

UNIVERSIDAD DEL NORTE

Mechanical Engineering Department



Vigilada Mineducación

DEVELOPMENT OF A CONTROL STRATEGY TO COMPENSATE
TRANSIENT BEHAVIOUR DUE TO ATMOSPHERIC
DISTURBANCES IN SOLAR THERMAL ENERGY GENERATION
SYSTEMS USING SHORT-TIME PREDICTION DATA

THESIS

submitted for the degree of:

Doctor of Philosophy in Mechanical Engineering

DAVID ROBERTO ACOSTA VILLAMIL

Barranquilla, Colombia

Noviembre 2021

DEDICATION

Esta obra, si se puede llamar así, no hubiese existido sin el apoyo emocional de toda mi familia. Pero especialmente de mi compañera Angélica, con quien todos los días descubro porque estoy listo para ser feliz.

No hubiera tampoco empezado este reto sin mi familia pequeña, mi Madre, mi Padre y mis hermanos, cada uno a su modo me sorprende asumiendo retos y luchando con fuerza por ellos. Ni esa familia grande en Bogotá. La red que creamos para sostenernos es fuerte así este construida con pensamientos.

También agradezco el apoyo de mis amigos, en Alemania y acá, y otros y otras que se volvieron amigos en este proceso. A muchos colegas de la maestría y el doctorado, les agradezco por las estimulantes conversaciones; espero todos sigamos construyendo algo en lo que creamos.

ACKNOWLEDGEMENTS

I want to acknowledge the UREMA group's work, particularly that of Jesus García and Richard Vasquez. They have set solid grounds for the understanding of high-temperature solar energy processes in our group. I would also like to acknowledge the simulation team's support in the Solar Institute of the DLR; they helped me leap forward in my research during my stay at Köln. After discussing the progress of my research with a new colleague Laurin Oberkirsch at the DLR, knowing that the ideas we discussed and simulated were tested in the Solar Tower in Jülich has been rewarding and inspiring. The joint work with Richard Rangel, Jesus Garcia, Professors Marco Sanjuan, and Habib Zambrano improved my approach to the thermomechanical stress problem. It shed light on my research, and it is included in this dissertation. I had the opportunity to present that work in Solar Paces 2020.

Foremost I would like to thank my advisor, Professor Sanjuan. Our conversations always managed to orientate my efforts towards clarity, despite some chaos in my thinking.

FUNDING

COLCIENCIAS financed the doctoral study framed within this research through a forgivable loan from *Convocatoria No. 727* (2015).

Additionally, Universidad del Norte partially funded this research through the forgivable loan associated with fellowship contract No. UN-OJ-2017-38173, and its amendments No. 1, 2, and 3. Finally, the international internship was partially funded by the Institute of Solar Research of the German Aerospace Center.

The content of this document is the sole responsibility of the author and his thesis director. It does not represent the opinion of any sponsoring institution or agency. The study's sponsors had no participation in the study design, data collection, data analysis, data interpretation, or in writing the document.

CONTENTS

ABSTRACT	1
1. INTRODUCTION	3
1.1. Towards a greener grid in Colombia	6
1.1.1. UREMA's research background	9
1.2. Historical evolution of CSP systems and state of the art	10
1.2.1. Research gap	18
1.3. Problem Statement	20
1.4. Objectives	21
1.4.1. General objective	21
1.4.2. Specific objectives	22
2. FUNDAMENTALS OF CSP	23
2.1. Solar Radiation	23
2.2. Central Tower Solar Power Plants	27
2.2.1. Heliostats	29
2.2.2. Solar field	33
2.2.3. Receiver	34
2.2.4. Thermal storage and Power block	41
2.3. Central tower plant operation	47
2.3.1. Clouds	55
2.3.2. Thermal stress on the receiver's tubes	63
2.4. Feedback and feedforward control strategies	65

2.4.1.	Feedback	65
2.4.2.	Feedforward Control	67
3.	CONTROL STRATEGY USING PREDICTION DATA	69
3.1.	Novel flux-feedback control strategy	70
3.1.1.	Controlled variables	71
3.1.2.	Manipulated variables	73
3.1.3.	Controller and architecture.....	77
3.2.	Solar radiation forecasting.....	83
3.2.1.	WobaS nowcasting system.....	85
3.2.2.	Disturbance resampling.....	88
3.3.	Design of an adaptive control strategy using nowcasting information	90
3.3.1.	Concept	91
3.3.2.	Implementation	91
3.4.	Design of a measuring system in Barranquilla as a starting point towards the prediction of short-term solar radiation	92
4.	RESULTS	97
4.1.	Reference Power Plant	98
4.1.1.	Steady-State Model	100
4.1.2.	Dynamic Model.....	102
4.2.	Evaluation of the feedback strategy	102
4.2.1.	Tuning the parameters of the feedback controller	115
4.2.2.	Feedback disturbance rejection.....	122
4.3.	Evaluation of the novel adaptive controller with feedback compensation.	127

4.3.1. Influence of the adaptive feedforward gain on the controller	131
4.4. Comparing the proposed strategy in terms of energy gain, thermal stress, and lifetime to an industry-standard practice	133
5. CONCLUSIONS	145
BIBLIOGRAPHY	149
APPENDIX A: Publications derived from this research	167
A.1. Solar Energy	167
A.2. Renewable Energy	167
A.3. Solar Paces 2020.....	168
A.4. Revista de Ingeniería de la Universidad de Antioquía	168
APPENDIX B: Other publications during the doctoral program.....	169
B.1. Revista Ingeniare : Aceptado para publicación	169

LIST OF TABLES

Table 1. Distribution of generation in the National Interconnected System (SIN) of Colombia according to Balance Energético Colombiano -BECO from UPME, in GWh. 7

Table 2. Summary of heliostat and receiver design parameters (Flesch et al., 2017). 98

Table 3. Average tracking speeds for scenarios starting at 11:30 a.m. and 12:40 a.m. for different values of the adaptive feedforward gain 132

Table 4. results of the fatigue analysis for both operation strategies 143

LIST OF FIGURES

Figure 1. Distribution of generation in the National Interconnected System (SIN) of Colombia according to data from <i>Balance Energético Colombiano -BECO</i> from UPME.....	8
Figure 2. Flux limit of a molten salt test receiver, taken from (D. C. Smith & Chavez, 1988)	13
Figure 3. The control algorithm for test receiver, taken from (D. C. Smith & Chavez, 1988)	14
Figure 4. Elevation angle A of the sun position, where \mathbf{nh} is the normal vector for the horizontal plane and \mathbf{ns} is the direction vector to the sun.	26
Figure 5. Spectral distributions for observed solar spectrum: extraterrestrial, terrestrial global AM=1.5, terrestrial direct AM=1.5, and Planck's spectrum for 5760 K, adjusted by one solar constant.....	26
Figure 6. Simplified diagram of a tower solar power plant	28
Figure 7. Heliostat's degrees of freedom, azimuth, and elevation.	29
Figure 8. Rows of heliostats at the DLR Solar Research Site at Jülich	30
Figure 9. Gaussian distributed flux map of a single heliostat, taken from (Grobler, 2015)	31
Figure 10. Heliostats in a solar field in the southern hemisphere	34
Figure 11. Power incident and losses on a solar tube.	35
Figure 12. Cross section area of the tubes in a panel and the quantities involved in the thermal model.....	36
Figure 13. Diagram of a reversible chemical energy storage system, taken from (Ballestrín et al., 2012).....	44
Figure 14. Hybrid wet and dry parallel cooling system, taken from (DOE, 2010)....	46
Figure 15. Large steam turbine power plant, taken from (K. Lovegrove & Pye, 2012)	47

Figure 16. States and transitions for the energy collection system, taken from (Zavoico, 2001)	48
Figure 17. Schematic diagram of the receiver flow circuit, taken from (Pacheco et al., 2002)	50
Figure 18. Transitions between states Energy collection system, made by the authors with information from (Zavoico, 2001)	51
Figure 19. Nitrate salt to be melted at Solar Two (1380 tonnes), taken from (Pacheco et al., 2002).....	53
Figure 20. Gemasolar plant behavior during a summer week, taken from (Schallenberg, 2013)	54
Figure 21. DNI and receiver outlet temperature for a cloudy day in Solar Two. At ~13:25, the receiver state changes to cloud standby, taken from (Pacheco et al., 2002)	55
Figure 22. Mean global energy budget of the earth-atmosphere system, taken from (Coley & Jonas, 1999)	58
Figure 23. Cloud models in voxel space, before height detection (left) and final model (right), taken from (B. Nouri et al., 2019).....	61
Figure 24. DNI Variability classification for a cloudy day on a CSP, taken from (B. Nouri et al., 2020)	63
Figure 25. Block diagram for a closed-loop feedback control strategy	67
Figure 26. Block diagram for a closed-loop feedback control strategy with feedforward compensation	68
Figure 27. Difference between the AFD and the incident flux on the discretized receiver's surface plane.....	73
Figure 28. Combination of aiming points and number of heliostats for Gemasolar and the reference power plant	74
Figure 29. Conceptual diagram of the proposed manipulated variables	75
Figure 30. Density function used to assign the radius that determines a movement constraint for the aiming points.	77

Figure 31. Block diagram of the proposed control strategy, the setpoint is the gap between the allowable flux density and the incident flux on the receiver.	78
Figure 32. Single Control Loop showing the signals involved in the control strategy for one group of heliostats.....	80
Figure 33. Control Loop for one group of heliostats for a zero valued Gap	82
Figure 34. Cloud objects in the voxel space (left) and corresponding nowcasted direct normal irradiance (DNI) map (right) (Pascal Kuhn et al., 2017).	86
Figure 35. Measured DNI for the dataset.....	87
Figure 36. Sample radiation map from WobaS for 11:05:00 on May 14 th , 2016, leadtime=0.....	88
Figure 37. WobaS datapoint in the center of the map, and interpolated values for 300 seconds	89
Figure 38. WobaS Radiation maps for 12:25:30 p.m. ($t = 270\text{ s}$) and 12:26:00 p.m. ($t = 300\text{ s}$)	89
Figure 39. Interpolated Radiation maps between 12:25:30 p.m. ($t=270\text{ s}$) and 12:26:00 p.m. ($t=300\text{ s}$) , every 5 seconds.	90
Figure 40. Block diagram for a closed-loop feedback control strategy with adaptive feedforward compensation	91
Figure 41. Diagram of the basic configuration for the solar radiation measurement system.....	94
Figure 42. Functional diagram of the measurement system.	95
Figure 43. Control panel for the solar radiation measuring system.	96
Figure 44. Schematic drawing for a panel of the receiver and one flow path for the molten salt.	98
Figure 45. Optical efficiency of the solar field with all heliostat aiming at the receiver's equator at noon on March 21 st	100
Figure 46. The crown temperature at the inner wall for the steady-state reference model and the model	101

Figure 47. Heliostat distribution and Sets assigned to a panel of the receiver. Green are the four sets of groups of heliostats closer than 700 m to the tower, and blue are the four sets of groups of heliostats farther than 700 m.....	104
Figure 48. Sets, and Groups assigned to one panel of the receiver.....	105
Figure 49. A panel of the receiver and groups assigned to its surface. Groups of heliostats with a slant range higher than 700 m are colored green, blue are those with a slant range under 700 m	106
Figure 50. Incident flux on the receiver a) before and b) after convergence of the proposed controller.....	108
Figure 51. The convergence of the error signals driving the 192 PI-Controllers to a steady-state value.	108
Figure 52. Average computation time for 60 iterations.	109
Figure 53. Evolution of the standard deviation as a measure of the homogeneity of the incident flux on the receiver's surface	110
Figure 54. Aiming point distribution on the receiver surface. The receiver circumference begins at the South facing panel and increases anticlockwise. a) Initial conditions for the configuration of the aiming points, b) Aiming points after the controller reached a steady state.	111
Figure 55. Optical efficiency after convergence, $k = 60$	111
Figure 56. Allowable flux density limit and irradiated flux on the central pipe for each panel. a) initial conditions for the aiming point configuration, b) after the controller reached steady-state	112
Figure 57. Allowable flux limit and irradiated flux on the central pipe in each panel with uniform noise in the flux measurement.....	113
Figure 58. DNI spatial distribution	114
Figure 59. Allowable flux limit and irradiated flux on the central pipe in each panel for iteration $n=0$ and $n=15$ after a change in DNI.....	114

Figure 60. Controlled variables response to a step-change in controller output for group 1	116
Figure 61. Identified static gains per group (Some outliers have been removed from this plot)	117
Figure 62. Labels for the geometric location in the solar field of the groups	118
Figure 63. Static gains for the models according to their location on the solar field	118
Figure 64. Time constants for the models according to their location on the solar field	119
Figure 65. Moderate vs. aggressive tuning result for one point of the receiver between 12:19 and 12:23 p.m. under disturbances	120
Figure 66. Distribution of the proportional gains for dispersion controllers in the solar field per groups	121
Figure 67. Proportional gains for the controllers according to their location on the solar field.....	121
Figure 68. Disturbance Scenario 1	123
Figure 69. Flux on the receiver at 11:30 a.m. under clear sky conditions for a near-optimal aiming point configuration obtained with the control strategy.....	124
Figure 70. Flux on the receiver at 11:30 a.m. under clear sky conditions, in a near-optimal aim point configuration, using the control strategy, with a linear index to represent the receiver surface.....	124
Figure 71. The response of the system with fixed aiming points to the disturbance at 11:30 a.m.....	125
Figure 72. The response of the system with the tuned feedback controller to the disturbance at 11:30 a.m.	125
Figure 73. Positive Index for the system's response for fixed aiming points and solar field feedback control under disturbances at 11:30 a.m.....	126
Figure 74. Negative Index for the system's response for fixed aiming points and solar field feedback control under disturbances at 11:30 a.m.....	126

Figure 75. Architecture for the testing of the adaptive control strategy with feedback compensation.....	127
Figure 76. Positive Index results from the adaptive feedforward with feedback compensation strategy and the feedback strategy for a disturbance at 11:30 a.m. ...	129
Figure 77. Negative Index results from the adaptive feedforward with feedback compensation strategy and the feedback strategy for a disturbance at 11:30 a.m. ...	129
Figure 78. Positive Index results from the adaptive feedforward with feedback compensation strategy and the feedback strategy for a disturbance at 12:19 a.m. ...	130
Figure 79. Negative Index results from the adaptive feedforward with feedback compensation strategy and the feedback strategy for a disturbance at 12:19 p.m. ...	130
Figure 80. Intercepted power using the adaptive strategy with different feedforward gains at 11:30 a.m.	131
Figure 81. Intercepted power using the adaptive strategy with different feedforward gains at 12:40 m.	132
Figure 82. Outlet temperature for both operation strategies. The shaded area represents molten salt, which could be directed to the hot tank.....	136
Figure 83. Equivalent stress	139
Figure 84. Equivalent stress evolution over the transient period for Inconel 625 in the (a) flow path 1 and (b) flow path 2 of the solar receiver.....	140
Figure 85. An estimate of S-N fatigue curve for Inconel 625.....	143
Figure 86. Axial-stress distribution on lateral surface of cylinder, taken from (Takeut & Nod, 1980)	144

NOMENCLATURE

DNI	Direct Normal Irradiance
GHI	Global Horizontal Irradiance
DHI	Diffuse Horizontal Irradiance
CSP	Concentrated Solar Power
PV	Photovoltaic
DC	Direct Current
PTC	Parabolic Through Collectors
IRENA	International Renewable Energy Agency
LCOE	Levelized Cost of Energy
AM	Air mass
NWP	Numerical Weather Prediction
IEA	International Energy Agency
FIT	Feed-in Tariff
PPA	Power Purchase Agreement
HTF	Heat Transfer Fluid
ASME	American Society of Mechanical Engineers
SAPS	Static Air Processing System
DAPS	Dynamic Air Processing System
AFD	Allowable Flux Density
SISO	Single Input Single Output
PID	Proportional Integral Derivative
MPC	Model Predictive Control

DMC	Dynamic Matrix Control
RMSE	Root-Mean-Square Error
ASI	All-Sky Imagers
ASTM	American Society for Testing and Materials
DOF	Degress Of Freedom
HFLCAL	Heliostat Field Layout Calculation
MCS	Master Control System
SPA	Sun Pixel Angle
PZA	Pixel Zenith Angle
ARIMA	Autoregressive Integrated Moving Average
FEA	Finite Element Analysis
PI	Proportional Integral
LCF	Low Cycle Fatigue
HCF	High Cycle Fatigue

ABSTRACT

There are two technologies used to convert sunlight into electrical power, photovoltaic (PV) and concentrated solar power (CSP). CSP is a promising renewable energy technology that can use the sun's power and replace the use of fossil fuels. It has, however, challenges to address to increase the pace at which it has been deployed globally.

Within CSP, two ways to collect the energy from the sun have the higher installed capacity. Parabolic through collectors (PTC) and solar towers. They differ on whether the sun is concentrated onto a line or a point. The solar towers are attractive due to the higher temperatures they can achieve, which allows for more efficient power conversion blocks. Solar towers are mainly composed of a solar field and a tower in which a receiver (heat exchanger) is connected to a power block. The solar field is made of thousands of heliostats, which are mirrors able to follow the sun and project the concentrated sunlight onto the receiver.

The receiver operates by using the projected power to heat a molten salt, producing steam and driving a conventional power block. These extensive solar power plants can provide power even at night due to their seamless integration with thermal storage.

Solar towers, with thermal storage, operate continuously, but they are subject to disturbances occurring from the interaction of the sunlight with the atmosphere. During these disturbances, vast areas of the solar field can be covered, interrupting the radiation reaching the heliostats, causing abrupt changes in the flux projected onto the receiver. This behavior can lead to thermally induced stresses and affect the integrity of the receiver. During these transient events, the molten salt velocity is usually increased to cool down the receiver tubes and prevent any malfunction; however, this results in non-collected energy.

To ensure proper operation of the receiver, each heliostat on the solar field must aim at the receiver, which depending on the sun position, yields a different angle at different hours. Complex optimization methods are used to determine the position of each heliostat. However, these methods are subject to parameter uncertainty and cannot compensate for real-time disturbances such as clouds because of their computational cost. This dissertation tackles this as a control problem by reducing the number of

variables found. Instead of searching for the elevation and azimuthal angle for thousands of heliostats, two proxy variables are used within groups of heliostats. Then, a feedback control strategy is implemented, taking advantage of this dimensional reduction.

The controllers use the flux projected onto the receiver to determine values for the proxy variables and ensure that the receiver operates within boundaries and with a homogeneous flux distribution.

Additionally, recent progress towards solar radiation forecasting using All-Sky Imagers (ASI) has been accomplished. This thesis takes advantage of a state-of-the-art nowcasting system and uses this forecasting information within a novel adaptive control strategy for the solar field. To the author's knowledge is the first solar field control strategy that uses nowcasting information to control heliostats in solar towers.

1. INTRODUCTION

According to the 2019 International Energy Outlook report, global energy consumption would increase by nearly 50% between 2018 and 2050 for the reference scenario. There is a 3% increase per year of the world's gross domestic product. However, this projection will undergo a severe revision considering how the COVID-19 pandemic will impact all economic forecasts. The report also indicates that, within the increase in electricity generation globally, production through renewable energy sources, including hydropower, would grow by an average of 3.6% per year. Among renewable energies, solar production would reach 8.3 trillion kilowatt-hours (*kWh*) of electric power generation globally by 2050 (US Energy Information Agency, 2019).

Renewable technologies that take advantage of solar radiation and have the largest installed capacity are photovoltaic (PV) and concentrated solar (CSP). In PV, radiation is directly converted into electricity, and in CSP, energy is transferred to a heat transfer fluid (HTF) through a photothermal process to fuel a downstream power block. PV is the most mature of both technologies; at the end of 2017, it had reached 415GW-DC installed globally, compared to 5.6GW in CSP installations (Margolis, Feldman, & Boff, 2018). However, if coupled with enough thermal storage, CSP generation is predictable, and it can adapt to the daily demand curve and cover programmed demand peaks (Bosatra, Fazi, Lionetto, & Travagnin, 2010).

Solar collectors are used to take advantage of direct solar radiation in CSP. They can be classified according to how the radiation is concentrated, whether in the focal line or at the focal point. Parabolic trough concentrators (PTC) are the most used within the focal line group, while central towers with heliostat fields are an attractive alternative to take advantage of focal point concentration. PTC are primarily used due to their high operating temperature and, consequently, the power cycle's greater efficiency and the ease of coupling to systems thermal storage (REEEI, 2012).

The learning rate is often used to measure the progress of renewable energy technologies. It is defined as the percentage reduction in project costs each time the accumulated installed capacity is doubled. According to the analysis of the International Renewable Energy Agency (IRENA) database, for electricity generation projects using CSP, the learning rate for the 2010-2020 period is almost 30% (IRENA, 2018a). Furthermore, through a comprehensive analysis of Levelized Costs of Energy (LCOE), the technical-economic analysis of 74 concentrated solar thermal energy projects shows a distinguishable decrease in the LCOE of CSP projects in recent decades, reaching an LCOE of 10.3 ¢/kWh in 2017 for a baseload CSP in 2017 (Musi et al., 2017)(DOE, 2017).

Progress has been so significant that by reviewing costs in projects commissioned in 2018 in Australia and Dubai using a reverse-engineering perspective, the technology proves sustainable and competitive (Lilliestam & Pitz-Paal, 2018). Two key enabling factors for these projects' low-cost environment are their low financing costs and very long power purchase agreements. Reduction of the LCOE for CSP systems remains among the objectives for research groups around the world.

Solar resource stochastic nature has a high impact on solar generation reliability; for example, the solar eclipse of August 21, 2017, caused an estimated decrease between 5.5 GWh and 11 GWh in large-scale photovoltaic generation in the western United States (Veda et al., 2018). CSP technology is attractive because it is naturally integrated into thermal energy storage systems, constituting a cost-effective manner of managing dispatchable energy.

For central tower systems, one way to reduce costs is to optimize the operation by developing strategies for real-time focusing of the heliostat field. Thus, guaranteeing homogeneous temperatures in the central receiver and contributing to increasing its life by reducing residual efforts due to temperature gradients (Jesús García, Chean Soo Too, et al., 2018). One of the components with the most significant impact on the cost

of tower systems is the central receiver, and the SunShot goals of the United States Department of Energy are a reduction of their cost to \$ 150 *per kW_{th}* (Mehos et al., 2017). The functionality of real-time focusing would improve the preheating process, allow for faster and safer starts, and even avoid full stops of solar energy production in the event of transients caused by clouds.

Radiation received from the sun on the earth is attenuated in its passage through the atmosphere by different phenomena. Radiation that is neither absorbed nor dispersed in the atmosphere and reaches the surface is called direct solar radiation. Diffuse radiation is the fraction of the incoming radiation that has been scattered in the atmosphere and reaches the surface. Interaction of solar radiation with molecules in the atmosphere can be modeled by Rayleigh and Mie scattering. The sum of direct and diffuse radiation constitutes the global radiation at the surface.

Physical study of atmospheric phenomena in equatorial zones has made it possible to understand the ocean's influence on the atmosphere and its complex interaction with fluctuations in global weather patterns. It is solar radiation that heats and evaporates water, which in turn, when condensed in the form of rain, releases such a quantity of heat that it becomes an essential factor in global atmospheric circulation (Stewart, 2009). Atmospheric properties that affect the solar resource include the concentration of aerosols, humidity, and clouds. The relative air mass (AM) concept is used to quantify the amount of space in the atmosphere that radiation must travel. When the AM is equal to one, the sun is vertically at sea level. In this location, solar radiation travels the shortest distance through the atmosphere to reach the ground. AM increases as the sun changes its position representing radiation's extinction as the sun moves towards the horizon. Clouds' stochastic behavior affects radiation at the Earth's surface, and the AM factor does not capture this modulation. Clouds cover an extensive area of Earth's surface, near 50%. Clouds' albedo, its effect on how short-wave radiation is reflected, and clouds' ability to absorb and radiate at long wavelengths negatively affect the balance of thermal energy global (Coley & Jonas, 1999). Considering that

the fuel of thermosolar plants is direct normal irradiance (DNI), and the factor with the most significant effect on its Spatio-temporal variability are clouds, techniques have been developed to predict solar radiation at the surface at different time scales.

Solar power's variability and reliability have become key factors for developers, financing institutions, and grid operators since cost and efficiency concerns have been addressed by continuous technological improvements (Kleissl, 2013). The long-term power commitments demand an increasingly accurate resource assessment. For grid operators, it is important to understand the effect of short-term power generation on managing their power grid and markets. Moreover, some of these forecasting techniques improve the operation of power plants during atmospheric transients caused by clouds or other phenomena.

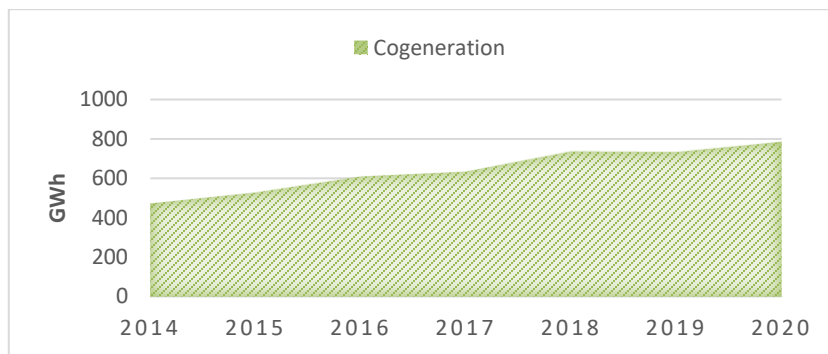
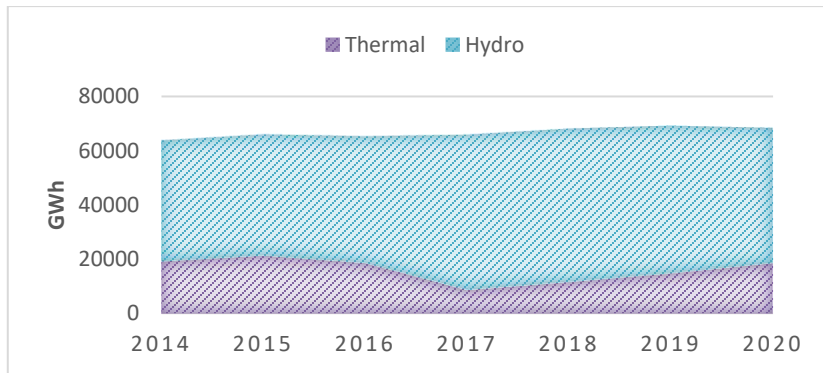
Most forecasting techniques are based on satellite information and numerical weather prediction models (NWP). Still, emerging new technologies are based on images from open-sky cameras (all-sky images) (P. Kuhn et al., 2018) (Bijan Nouri et al., 2019). The integration of this type of information to the control schemes of tower solar thermal power plants is a logical step in the evolution of CSP systems (Noureldin et al., 2018).

1.1. Towards a greener grid in Colombia

As seen in Table 1 and Figure 1, the diversification of Colombia's energy supply is insufficient. Large hydropower suppliers and fossil-fueled thermal power plants dominate it. Almost 70% of the centralized installed capacity in Colombia is hydraulic, with a only a three month water reservoir, which makes Colombia's energy supply highly vulnerable to weather phenomena like *El Niño* and macroeconomic variables such as fossil fuel prices (Benavides, Cadena, González, Hidalgo, & Piñeros, 2018). Following the tragedy of the Ituango Hydroelectric Power Project, which by 2019 was expected to add on average 13900 *GWh* to the National Interconnected System, the government set as one of its goals to multiply the NCRE generation capacity.

Table 1. Distribution of generation in the National Interconnected System (SIN) of Colombia according to Balance Energético Colombiano -BECO from UPME, in GWh.

	Solar PV	Wind	Cogeneration	Thermal	Hydro	Total
2020	191	10	783	18503	49837	69324
2019	132	63	732	14750	54437	70114
2018	11	43	734	11507	56648	68943
2017	5	3	633	8588	57328	66557
2016	0	51	608	18486	46788	65933
2015	0	68	526	21272	44682	66548
2014	0	70	472	19044	44742	64328



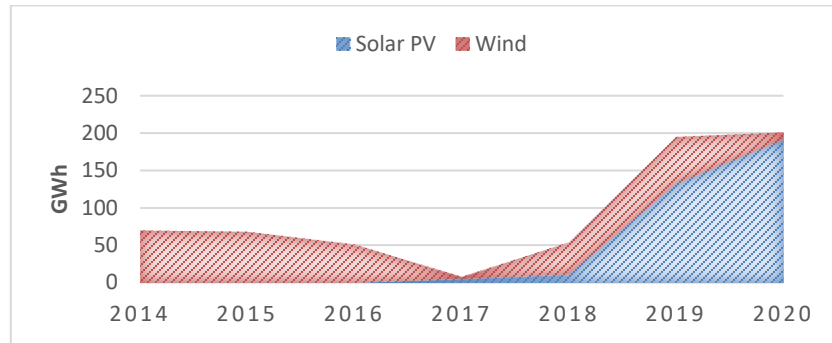


Figure 1. Distribution of generation in the National Interconnected System (SIN) of Colombia according to data from *Balance Energético Colombiano -BECO* from UPME

In 2019, the first successful auction in Colombia to incorporate NCRE took place (XM, 2019). Moreover, Colombia has taken enormous steps in public policy to address the challenges posed globally by climate change. Remarkably, the current government has committed to reducing CO_2 emissions by 51% in 2030. Along with these changes, the correlation of hydro and non-conventional renewable energy projects, shows that a deeper penetration of renewables reduces volatility of available energy in Colombia's energy portfolio, and also it increases the energy availability in the dry season (Benavides et al., 2018). Hence, it is expected that Colombia will make a big leap from over 10MW of installed solar renewable capacity in 2018 to more than 2800 MW by 2022 of combined solar and wind capacity. To that end, the government has signed contracts following a public auction in 2019 in which solar and wind energy projects have been assigned Power Purchase Agreements (PPAs) for 1298.9 MW. These projects should be commissioned in 2022. Together with NCRE projects under construction, Colombia will reach a capacity of 2,250 MW which exceeds the government's goals.

Although this ambitious plan was crafted before the health and economic crisis caused by the pandemic in 2020, a new auction took place in October 2021 with 15-year PPAs for 11 solar projects with a combined capacity of 796.3 MW (XM, 2021). These projects should start delivering electricity by the end of 2022. Before these auctions,

Colombia has taken significant steps towards introducing renewable energy sources into the grid. The first, and so far, the most important regulatory effort was the law 1715 of 2014 (Hernandez, Arredondo, & Rodriguez, 2019). This law, and the decrees and resolutions which enable it, sought to promote the development, and use of non-conventional renewable energy (NCRE) sources, by establishing tax benefits for investments in projects that integrate new green technologies into the Colombian grid. In June 2020, decree 829 streamlines the tax incentives of law 1715 for electric energy service providers, both foreign and traditional (The International Energy Agency (IEA), n.d.).

1.1.1. UREMA's research background

The UREMA research group at Universidad del Norte has four research lines. This work impacts two of them, i.e., Energy conversion and industrial process control, thus being in line with the group's goal to address the global need for energy efficiency and sustainable environments.

Our group has an ongoing interest in studying concentrated solar thermal technologies along the energy conversion research line, where radiation from the sun is concentrated and transformed into high-temperature thermal energy. Experience in estimating the potential of harnessing solar radiation has been gained in partnership with the University of South Florida (Besarati, Padilla, Goswami, & Stefanakos, 2013).

Parabolic trough power plants and central tower plants are the most commonly installed technologies for Concentrated Solar Power (CSP) generation. The group has gathered experience modeling the heat transfer phenomena for both technologies (Padilla, Demirkaya, Goswami, Stefanakos, & Rahman, 2011) (Chean et al., 2019).

One of the main technical challenges with CSP technologies is the stochastic nature of atmospheric disturbances, such as cloud passages. One of UREMA's contributions to the state-of-the-art was developing a biomimetic simulator of clouds (Jesús García, Portnoy, Vasquez Padilla, & Sanjuan, 2018). Researchers in the prestigious CSIRO

research center in Australia have already used the simulator to compare two control strategies using either manual valves or motorized valves in a parabolic trough solar plant under cloud shading (Abutayeh et al., 2019).

Finally, in the research line of control of industrial processes relating to CSP and Solar Power Towers, advances have been made towards solar field controllers using modern control techniques. A significant advance is a technique to control aiming points of groups of heliostats, enabling a reduction in the control problem's dimension. Using this technique, a Dynamic Matrix Controller effectively compensates atmospheric disturbances in a simulated power plant with 2650 heliostats (Soo Too, García, Padilla, Kim, & Sanjuan, 2019).

The research conducted for this dissertation has been possible thanks to those previous research efforts and more across the UREMA group.

1.2. Historical evolution of CSP systems and state of the art

The first “commercial” heliostat dates to 1968 in France, where Professor Trombe built a 1 MW_{th} solar furnace in which 63 heliostats of 45 m^2 were placed on a mountain forming a nearly two thousand square meter parabola whose focal point was 30 m away. This furnace was capable of concentrating around 13500 suns. (Vant-Hull, 2012). The first commercial solar tower power plant began operating in Spain in 2011; the Gemasolar project uses a 120 MW_{th} receiver and 15 hours thermal storage (Kolb, 2011).

By 2018, there were 84 CSP stations with a capacity exceeding 10 MW in 11 countries, with a global CSP capacity of 5.2 GW, which ramped up from 490 MW in 2008. And CSP was expected to generate 14.3 TWh annually (Lilliestam, 2018). The installed capacity of this technology grows slowly, which is not on track with the sustainable development scenario from the International Energy Agency (IEA, 2020). Studies in the literature describe the expansion of CSP in four phases (Lilliestam, 2018):

- 1) During 1984-1990, 9 Solar Energy Generating Systems (SEGS) stations were built in the Californian desert, taking advantage of a power purchase agreement (PPA). Due to the fall of the gas price at the end of the 80's the avoided costs and tariffs fell too, stopping further constructions. These stations remain operational.
- 2) In 2007, through a feed-in tariff (FIT) for CSP, the Spanish government helped achieve an installed capacity of 2.3 GW in 7 years. This public policy promoted both Spanish and German manufacturers and developers within the new industry. In 2012 with the end of the FIT scheme, expansion stopped. The developed industry has been weakening ever since.
- 3) From 2013-2016, a geographical turn from Spain to South Africa, Morocco, India, and the US took place. In this phase, competitive PPAs fueled rapid growth, almost 2 GW in 4 years. As US support stopped, the market became small, and the CSP industry and its supply chains were reduced.
- 4) Starting in 2016, the Chinese government began a policy supporting scheme for 20 projects for a total of 1.35 GW, using as public policy a FIT of USD 0.17 per kWh. The expansion derived from this policy came with new Chinese developers and manufacturers.

All this development started with research facilities in the 1980s and 1990s, when several demonstration electric power plants using solar central receivers were built, with a combined capacity of more than 25 MW_e . Only two of these plants used surrounding fields and a cylindrical receiver: Solar One, operated from 1982 to 1988, and Solar Two from 1996 to 1999, each with a capacity of 10 MW_e .

Solar one used Water/Steam as a working fluid, but its generation at over 500 °C and the high pressure demanded thick wall tubing, subject to large heat fluxes. Due to the thermal gradients and corresponding stresses, the allowable flux density was very low. Moreover, rapid changes from cloud passage made control complex, which led to the selection for Solar Two of a single-phase medium for the receiver, and better, one that

could be used for storage. Hence, Solar Two used Molten Salt as HTF. Consequently, the project also included a 107 MW_{th} thermal storage unit, which made both the collection and dispatch of energy independent, and thus, fully dispatchable (Vant-Hull, 2012).

In 1987, a study in the US was published by Kistler, which used weather data with insolation information at 3-minute intervals. The actual number of insolation cycles and their magnitudes was obtained from a location near Barstow, California, in 1984. They defined a cycle as any variation in insolation that reduces a receiver tube's remaining fatigue life. The study analyzed a cylindrical external receiver with inlet and outlet fluid temperatures of $290\text{ }^{\circ}\text{C}$ and $590\text{ }^{\circ}\text{C}$, respectively, liquid sodium as working fluid and 316 stainless steel as tube material. The total strain associated with each end of an insolation cycle was calculated with an analytical method. The effective strain range specified by ASME B&PV Code Case N47 was used along the fatigue tables to determine an effective fatigue life for each cycle type. To calculate the amount of fatigue over 30 years, researchers used a linear summation damage rule. Each cycle's fraction of life was obtained by dividing the actual number of cycles by the effective fatigue life. Summing these ratios for all cycle types, the fraction of fatigue life consumed for this design was obtained. The weather data and the receiver design examined justified a fatigue life of 10,000 design point cycles. Still, given the uncertainties, they recommended a safety factor of 2 in the design, suggesting that solar central receivers should be designed for a fatigue life of 20,000 design point cycles (Kistler, 1987).

Following the valuable lessons learned from Solar One came the successful design, construction, and testing of a solar central receiver of 4.5 MW_{th} using molten nitrate salt as a HTF. The Saguaro commercial receiver was used as the basis for the test receiver of that research. It was designed for 10,000 daily start-ups and 40,000 cycles due to cloud passage, which were used to represent 30-year design life. Thermal stress

occurs in panels due to absorbed heat flux leading to fatigue of the tubes because of the cycles involved in daily operation and cloud events. Furthermore, the high temperatures also include creep damage. Researchers used methods from the Nuclear code in the ASME Code Case N- 47 and a study of cloud cycles determined from meteorological data from the Solar One plant and found that the cumulative effect from cloud cycles was equivalent to 20,000 full cloud cycles. Their research concluded that thermally induced fatigue in this system is more damaging than isothermal mechanically induced fatigue. Flux limits for the receiver, shown in Figure 2, were derived considering fatigue limits of the tube material and the maximum allowable salt-metal interface temperature of 593°C to avoid corrosion (D. C. Smith & Chavez, 1988).

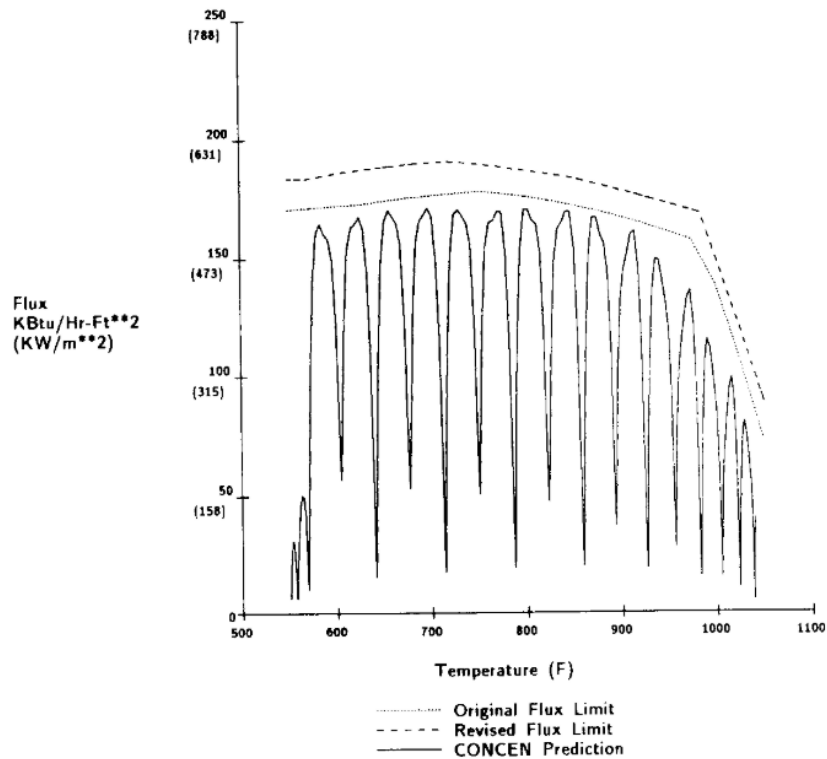


Figure 2. Flux limit of a molten salt test receiver, taken from (D. C. Smith & Chavez, 1988)

To control the receiver's outlet temperature, keeping a high outlet temperature while avoiding the corrosion limit, the control algorithm, shown in Figure 3, uses heat-flux

sensors on the panels and thermocouples attached to the back of the tubes. Flux signals and back-tube temperature signals feed into the algorithm as feedforward signals. The outlet temperature is also used as a feedback signal. Salt flow in each of the control zones and total flow are measured (D. C. Smith & Chavez, 1988).

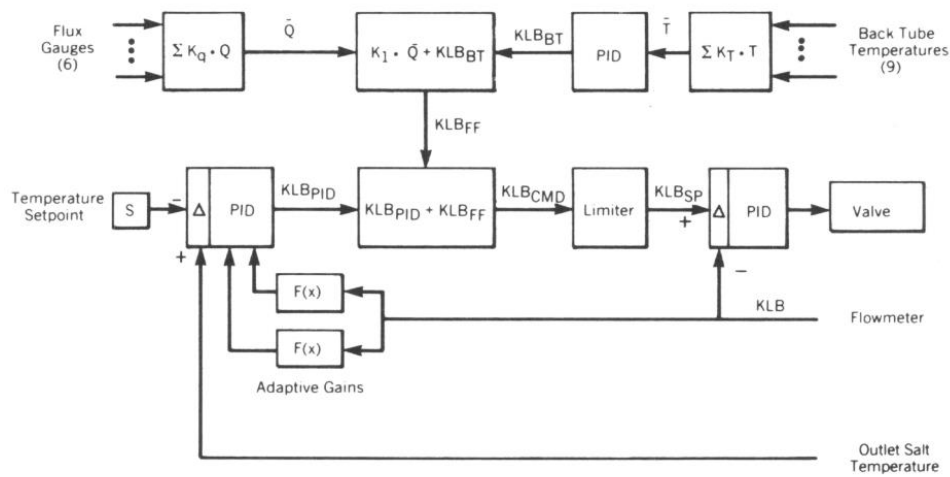


Figure 3. The control algorithm for test receiver, taken from (D. C. Smith & Chavez, 1988)

It is in Solar Two where a first multilevel vertical aim strategy is documented. Two software-based systems managed the heliostat solar field: the Static Aim Processing System (SAPS) and the Dynamic Aim Processing System (DAPS). The SAPS considers that each Heliostat aim point must change periodically, in 10- minute intervals for normal conditions, depending on the sun position, considering that the size and irradiation distribution of a heliostat beam change during the day and throughout the year. The effect of tracking errors was modeled as an increase in beam size. This approximation was deemed appropriate considering the averaging effect of having thousands of heliostats aiming at the receiver (Bradshaw et al., 2002).

The DAPS updated the aim points at least every 30 seconds, and its goal was to protect the receiver when overflux conditions arose during normal operation to fulfill the 30-year design life. The predicted flux incident on the receiver using the aiming points

from SAPS, ambient temperature, and estimated heliostat errors were used to calculate the receiver surface and film temperatures and then find areas with excess flux. Sequentially heliostats with higher flux contributions were removed, and the calculations repeated until no flux limits were exceeded. Finally, these heliostats were removed from tracking in the actual solar field. However, undesirable interactions with the mass flow controller lead to this system being deactivated, and on the final report, they said about such approach: “It appears at this time that the molten-salt power tower industry would not use a system like DAPS at future plants.” (Bradshaw et al., 2002)

The receiver control algorithm on the Solar Two project was used for the automatic operation of the receiver. It had two major objectives, first, maintaining the salt temperature at 565°C at the receiver's outlet and second, limiting thermal fatigue damage to receiver tubes, thus, ensuring the calculated 30-year life of this component. It used three signals to accomplish its task. The first one came from a feedforward path from eight photometers to sense incident power projected onto the receiver; the second, a feedback signal from the average back-tube temperature. And third, a feedback signal from the salt-outlet temperature from thermocouples. These signals informed a proportional-integral (PI) controller that regulated the flow control valve to achieve the flow setpoint. A cloud-standby feature was implemented, which simplified the algorithm, and the final version eliminated the feedback signal from the tube back-wall thermocouples. (Bradshaw et al., 2002)

Among the open technical challenges to accelerate the growth of solar tower plants' installed capacity is increasing their efficiency. An aiming strategy that reduces the spillage while simultaneously considering the flux density constraints and can compensate disturbances is the topic of this dissertation and a pathway to attack that technical challenge. The problem of finding an optimal heliostat configuration has been tackled predominantly, according to a comprehensive literature survey, using open-loop strategies.

In the first algorithm we reference, intended for cylindrical receivers, a radius of the beam at the receiver from each heliostat is estimated. Then, to reduce the flux, the aim of half the heliostats is moved towards the outer edge of the receiver until their beam reaches the top. The other half is moved towards the bottom of the receiver. Thus, rapidly increasing the flux level in areas closer to the edges and causing a decreased and homogeneous flux towards the equator (Vant-hull, 2002). A similar approach divides the field into three zones, and the algorithm fits the parameters for each zone (Collado & Guallar, 2019). A further modification of the Vant-Hull algorithm has been proposed, in which a factor modifies the estimated cone angle. The slant range, i.e., the distance between the heliostat and the tower, is multiplied by a tunable scaling parameter to obtain the factor. (Flesch, Frantz, Maldonado Quinto, & Schwarzbözl, 2017).

In another approach, an Allowable Flux Distribution (AFD) for each panel was obtained using as constraints the thermal stresses and the corrosion limits. The methodology accommodates flux images from each heliostat in a solar field to fit the AFD. The algorithm uses a symmetric aiming strategy from the equator and an aiming factor that moves the heliostats' aiming points vertically for each panel. (Sánchez-González, Rodríguez-Sánchez, & Santana, 2017). Several optimization methods were implemented for a cylindrical receiver in other work, branching the optimization problems in several sub-problems. They find that the most efficient approach considers flux overlap from neighboring heliostats (Astolfi, Binotti, Mazzola, Zanellato, & Manzolini, 2017).

The optimization problem can be formulated in a discrete form. Heuristic methods have been used to solve it, for instance, a genetic algorithm (Besarati, Yogi Goswami, & Stefanakos, 2014) and the ant-colony optimization algorithm (Boris Belhomme, Pitz-Paál, & Schwarzbözl, 2014). A mixed-integer linear programming approach has also been used in which an optimal aim point distribution is found. This algorithm is tested under disturbances' influence, even though the disturbance used resembles a square

cloud, not a real one (Ashley, Carrizosa, & Fernández-Cara, 2017). Extending this approach to allow the aiming point variables to take any value and using a bi-objective optimization model is further developed by the authors (Ashley, Carrizosa, & Fernández-Cara, 2019).

Most of the mentioned approaches have a high computational time and do not consider cloud events, making them unsuitable for real-world applications. Although predicting cloud influence on incoming radiation is currently not state-of-the-art, closed-loop approximations would be able to compensate for inaccurate heliostat tracking models and disturbances such as clouds.

The first closed-loop approach for a solar field control comes from the Solar Two project in which Vant-Hull designed a simple controller to avoid excess flux above the allowed AFD. When an area of the receiver was identified with a higher flux than desired, the heliostat with the highest estimated contribution to the flux was identified and redirected towards an aiming point outside the receiver surface (Vant-Hull, 2012). The algorithm, referenced next, used operator knowledge to create a heuristic heliostat control strategy that optimizes the temperature distribution. It was not designed for an external receiver but a volumetric receiver (García-Martín, Berenguel, Valverde, & Camacho, 1999).

The work referenced ahead stems from research carried out at the UREMA research group. In the first work, sets of single-input single-output (SISO) subsystems with Proportional Integral Derivative (PID) controllers are implemented. Groups of heliostats form the subsystems with two manipulated variables: the vertical movement of the aiming points' centroid and the dispersion of the group's aiming points. The vertical movement is constrained to start from the equator, and if it advances, it moves towards the edge of the panel where the salt enters. The field was divided into 12 sections, each with three groups. For each group, a PID controller was used for the manipulated variable. A simulated Gemasolar-like plant with 2650 heliostats was used

for demonstration (J García et al., 2017). In subsequent work, a multivariable model predictive control (MPC), precisely Dynamic Matrix Control (DMC) approach for cylindrical receivers, was implemented using the same configuration of manipulated variables (Jesús García, Chean Soo Too, et al., 2018). This configuration is adjusted to account for dynamic cloud disturbances by adding a PI controller, which avoided flux peaks after the cloud cleared the solar field (Jesús García, Chean, et al., 2018).

1.2.1. Research gap

The SunShot Initiative in 2011 aimed to make the cost of solar electricity competitive compared with conventional power generation technologies by 2020. The roadmap proposed addressed R&D gaps, including as a goal real-time flux feedback. The reason was that having real-time flux distribution, uniformity, and levels could improve plant performance and address concerns of overheating damage to the receiver tubes. It is also mentioned that it would allow for better control of the heliostat field, and the report added that no robust solution exists currently (Mehos et al., 2017). The goals for 2030 are even more aggressive. The need to accelerate the economic competitiveness of CSP is evident, and optimizing plant operation is one of the pathways to achieve this goal.

The spatial variability of the solar resource, coupled with its stochastic nature, makes using single-point sensors to inform controller decisions at solar power plants unreliable. In 2016, a model was developed to study the transient effect of varying and dynamic solar conditions for the parabolic trough collectors (PTC) plant control. It was then envisioned that short-term spatially resolved DNI forecasts could predict field behavior in advance and be used in control strategies (K. Nouredin, González-Escalada, Hirsch, Nouri, & Pitz-Paal, 2016).

In 2017, the WobaS-4cam was validated after being operational at two solar energy research centers and a commercial 50-MW solar PV-power plant. The system was able to derive nowcasted direct normal irradiance and global horizontal irradiance (GHI) maps. The system hardware consisted of 4 all-sky cameras, and it was validated on 30

days representing various weather conditions. It was found that spatial aggregations reduced the GHI-RMSE to 13.0% for the current time, and field sizes between 25 m^2 and 4 km^2 . Temporal average reduced the GHI-RMSE deviation from 25.3% (medium lead time 7.5 min, 1 min temporal average) to 19.0% (medium lead time 7.5 min, 15 min temporal average). It was envisioned that nowcasting systems such as the WobaS system would contribute to managing ramp rate limitations, resulting in reducing the required battery size and compensating the variability induced by clouds avoiding unstable effects on electrical grids (Pascal Kuhn et al., 2017).

By 2019, a solar irradiance nowcasts system derived from all-sky imagers (ASI) demonstrated its ability to track individual cloud height and motion vectors (B. Nouri et al., 2019). The system has also been used to evaluate if a given DNI variability classification of point-like measurement is correlated to other classification using field average results obtained with the system (Bijan Nouri et al., 2018).

Also, in 2019, a method able to determine a weather-dependent uncertainty specification of DNI nowcasts was presented using the ASI-based nowcasting system. The method can provide, in real-time, not only the spatial and temporal resolved irradiation maps but also the uncertainty associated according to the method. The uncertainties were obtained after studying two years of DNI variability and errors from the ASI nowcasts. For each combination of DNI variability class, Sun angle, and lead-time, an upper and lower uncertainty value describing a coverage probability of 68.3% is obtained from historical data. The corresponding uncertainty due to the specific variability class is stored in a database. It was found that the most significant deviations correspond to highly variable weather conditions, and they increase with the nowcast horizon (B. Nouri, Wilbert, et al., 2019).

The first application of solar field control using spatially resolved DNI information from all-sky imagers (ASI) appears in 2020. Two novel control strategies are developed in this study, optimizing control parameters depending on spatial and temporal DNI

variability classes. These controllers were tested for 22 days in a simulation environment, and a relative increase in revenue of 1.9% was observed compared to a state-of-the-art reference controller (B. Nouri et al., 2020).

The breach found in the state-of-the-art is the use of nowcasting or short-term forecasting information to control the solar field of central tower systems, which increases power intercepted by the receiver while fulfilling system constraints.

1.3. Problem Statement

One of the contributions to the control of CSP tower power plants of the UREMA research group consists of using an agent-based strategy to decrease the closed-loop control variables to find the heliostat's aiming points that distribute the incident flow over the central receiver. This contribution opens the doors to test modern control strategies to control the thousands of mirrors that make up the generation plant using low computational power.

On the other hand, the need for optimal operation of CSP systems has motivated the development of solar radiation prediction systems to manage energy dispatch to the electrical grid and have better control of the thermodynamic power cycle. The analogy with a natural gas turbine where fuel is suddenly unavailable helps to understand the need to anticipate and compensate for solar radiation variability. Specialists from various fields of work in CSP technology participated in the DNICast Project in a joint research effort from the European Union. Research groups such as the National Center for Renewable Energies -CENER and the Center for Energy Research, Environmental and Technological -CIEMAT of Spain, the Institute for Solar Research from the DLR of Germany participated. They developed components and techniques to improve the state-of-the-art and reduce uncertainty in direct solar radiation (DNI) prediction systems (Gastón et al., 2017). One of the objectives of the working group on solar energy meteorology of the DLR Institute of Solar Research is to know the solar radiation in a horizon of 15 minutes. In cooperation with the companies CSP Services

GmbH and TSK Flagsol Engineering GmbH, they developed a short-term forecasting system called WobaS-4cam, which is being tested in commercial solar plants in Spain. In a 30-day validation period, they found relative errors (RMSE) of 20.4% in predicting global horizontal irradiation for a 15-minute horizon at the pixel level (25 m²). This product uses the latest technology in the field (P. Kuhn et al., 2018).

The currently commissioned central tower systems use thermal salts as the working fluid, and the receivers used for said molten salts operate in the range of 1000 – 1200 kW/m² (Relloso & García, 2015). Therefore, managing transitory periods of operation during the Passage of clouds is vital to preserving the central receiver's physical integrity. The strategies to locate heliostat's aiming points in a tower solar thermal generation system to control the central receiver's energy flow are critical to guarantee operational limits. Control strategies that can compensate the energy in the receiver subject to operation and safety restrictions by manipulating the field heliostats is a current research problem that can reduce operational costs and impact the LCOE of future power plants.

This thesis presents an effort to develop control strategies that, using information from short-term solar radiation prediction systems, compensate for transients caused by clouds and improve the use of available solar radiation without exceeding operational limits in solar tower plants.

1.4. Objectives

This section presents the objectives of this research.

1.4.1. General objective

Develop a multivariate closed-loop control strategy that compensates for atmospheric transients using information from short-term solar radiation forecasting systems to aid in maximizing the utilization of solar radiation without exceeding operational constraints in solar tower power plants.

1.4.2. Specific objectives

- Establish a methodology for identifying a mathematical model of the dynamic system of tower solar power plants, using input-output measurement data.
- Design a closed-loop multivariate control strategy to control the temperature in the central receiver using the identified model and subject to operational restrictions.
- Establish a model representing the dynamic behavior of a short-term solar radiation prediction system following the current state of the art and based on actual solar radiation measurements.
- Design a control strategy that incorporates the information from the model of the solar radiation prediction system and analyze its behavior in the face of transients of solar radiation caused by clouds.

2. FUNDAMENTALS OF CSP

This chapter offers a broad overview of the most important concepts necessary to approach this dissertation's subject. In the first section of the chapter, a brief introduction to solar energy basic concepts is presented. A description of quantities related to solar energy and the influence our atmosphere has on its path towards the ground is explored.

The following section describes the main components of a central tower solar power plant that are relevant to the system performance. First, the heliostats are introduced, including their state-of-the-art structure, sources of uncertainties, and qualifying efforts. Second, we present the solar field and considerations about the location of each heliostat in it. And third, the receiver is presented, describing the basics behind the energy transport mechanism and thermal losses that determine the effectiveness of the transformation from radiative to thermal energy.

In section 3, two essential concepts from control theory are introduced, feedback and feedforward closed-loop control strategies. These two classical techniques are some of the most widely used control techniques in the industry due to their capacity to control process variables, usually around some operating point; hence, their use is not restricted to linear systems. This section is introduced because the strategies proposed in this thesis take advantage of this basic architecture.

Finally, at the end of the chapter, the technological gap stated in the description of the problem is reviewed in detail, including a brief discussion about the thermo-mechanical stresses induced on the receiver tubes, which may cause low-cycle fatigue and a reduction of lifetime for the tubes.

2.1. Solar Radiation

The sun can be thought of as a sphere with a radius of $6.96 \times 10^8 \text{ m}$ which is $1.496 \times 10^{11} \text{ m}$ away from earth. It emits radiation as a result of thermonuclear

reactions, such as the conversion from hydrogen to helium, for a total rate of energy emission of $3.8 \times 10^{23} \text{ kW}$. Only a small fraction of that energy reaches the earth and constitutes the planet's dominant source of energy (Goswami, 2015).

The spectrum of energy radiated by the sun can be approximated by considering it a black body emitter of temperature $T = 5760 \text{ K}$, which follows the thermodynamic relation between spectral radiance L_λ and wavelength λ , as expressed by Planck's equation:

$$L_\lambda(\lambda, T) = \frac{2hc^2}{\lambda^5} \frac{1}{e^{hc/\lambda kT} - 1} [\text{Wm}^{-2}\mu\text{m}^{-1}] \quad (1)$$

Where $h = 6.62 \times 10^{-34} \text{ Js}$ is Planck's constant, $c = 2.99 \times 10^8 \text{ m/s}$ is the light velocity in a vacuum and $k = 1.38 \times 10^{-23} \text{ Js/K}$ is Boltzmann's constant.

Radiant Flux is defined as the energy (Q) passing through an area A in a unit time:

$$\phi = \frac{dQ}{dt} [\text{W}] \quad (2)$$

Radiance L is used to express how a radiant flux emerges from a plane dA and a solid angle $d\Omega$ in direction Ω with angle θ to the normal of dA :

$$L = \frac{d^2\phi}{dA \cos\theta d\Omega} [\text{Wm}^{-2}\text{sr}^{-1}] \quad (3)$$

On the other hand, the radiant flux density or Irradiance E is the radiant flux incident onto an element plane dA of orientation Ω_A but only considering the radiation coming from the direction Ω , where the cosine of the angle between Ω and Ω_A is positive (Winter, Sizmann, & Vant-Hull, 1991):

$$E = \frac{d\phi}{dA} [\text{W/m}^2] \quad (4)$$

Radiation just above the earth's atmosphere is called extraterrestrial radiation and can be considered constant. Its mean value is called the solar constant $S_0 = 1367 \text{ W/m}^2$. The extraterrestrial radiation path through the atmosphere is filled with absorption and scattering phenomena, which extinct part of the solar radiation until it reaches the ground. The main processes which affect the terrestrial radiation, without considering thick clouds, are according to Sizmann (Winter et al., 1991): Rayleigh scattering by molecules of the air, absorption by ozone, CO_2 , O_2 , and water vapor, and extinction by aerosol particles and high or cirrus clouds. The way to relate the fraction of transmitted flux (ϕ) through a medium to the incident flux (ϕ_0) is called the transmittance and is equal to:

$$\tau = \frac{\phi}{\phi_0} \quad (5)$$

Part of the radiation that has been scattered through the atmosphere reaches the surface. It is called diffuse irradiance, and together with the direct or beam irradiance, constitute the global irradiance, which is measured on a horizontal surface. Moreover, the optical path's length through the atmosphere changes the spectral distribution of solar radiation. The air mass (AM) describes the ratio of the solar radiation optical path's length to the length of the shortest optical path through the atmosphere or $AM=1$. That is:

$$AM = \frac{1}{\sin A} \quad (6)$$

When the sun is at the zenith, the path is shortest, as shown in Figure 4.

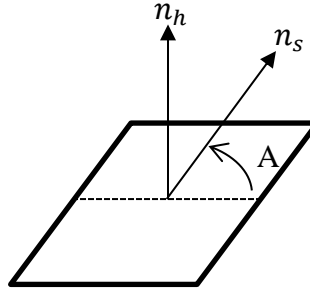


Figure 4. Elevation angle A of the sun position, where n_h is the normal vector for the horizontal plane and n_s is the direction vector to the sun.

In Figure 5, the spectral distribution for the extraterrestrial solar spectrum, or AM=0, is plotted for a range of wavelengths. Also, Planck's spectral distribution for $T = 5760\text{ K}$ is shown. Furthermore, the direct and global standard spectral irradiance distributions according to ASTM G173 – 03 are also shown for an AM=1.5.

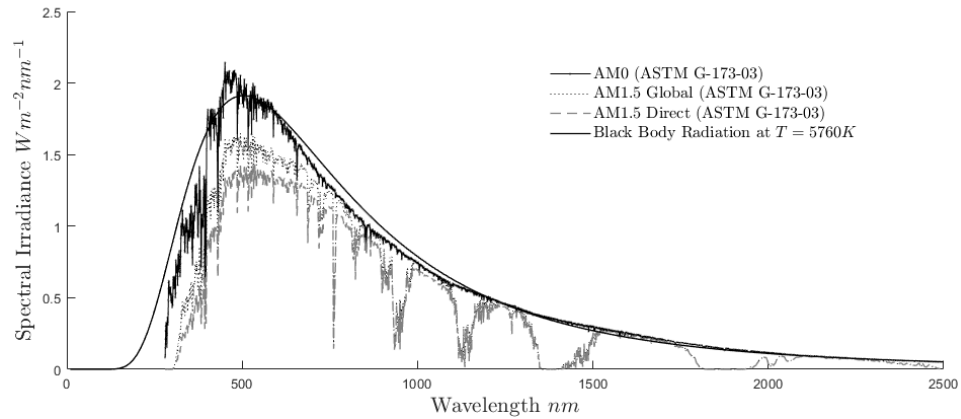


Figure 5. Spectral distributions for observed solar spectrum: extraterrestrial, terrestrial global AM=1.5, terrestrial direct AM=1.5, and Planck's spectrum for 5760 K, adjusted by one solar constant.

For the radiant flux's thermodynamic quality to be measured, a standard spectrum is often defined, from which the integral quality of solar radiance can be calculated. The ratio between the maximum obtainable power and the solar part of the spectrum, omitting the ambient radiance, yields the solar radiation quality. For a temperature of the sun of $T_s = 5777\text{ K}$ and $T_a = 300\text{ K}$, Sizmann writes: “only 7% of energy in the solar incident flux is inevitably lost due to the requirement to drain, via waste heat, the entropy income which accompanies the radiant flux”. Furthermore, he states that optical concentration contributes to keeping the radiation's entropy content as low as possible. This author adds: “the degree of quality of conversion to heat by absorption processes increases with concentration ratio” (Winter et al., 1991. p.40, p.47). For these reasons, the optic concentration of beam radiation is used with the primary goal of increasing the flux density E of a radiant flux ϕ .

2.2. Central Tower Solar Power Plants

Concentrating solar power (CSP) central tower plants can be divided into four main components. The first one is the solar field (see solar heliostat field in Figure 6), comprising hundreds or thousands of heliostats, which are mirrors with the capacity to track the sun with 2 degrees of freedom (DOF). Second (see the receiver in Figure 6), a receiver is located on a tower and absorbs the energy reflected from the solar field. The energy is transferred to a heat transfer fluid. Within this dissertation framework, we will study external receivers using molten salt as HTF, explained in detail in section 2.2.3. Third, a power block where process heat in the fluid is used in thermodynamic cycles to produce electricity. High concentration factors due to a large number of heliostats are translated into high process temperatures, which results in the potential for higher efficiency in the transformation to electrical energy. The final component of a solar tower is the control system, which decides each heliostat position and controls other essential process variables.

As shown in Figure 6, there are two tanks where the molten salt is stored. It is common to use a non-eutectic mixture of inorganic salts as the HTF. One of these commonly known solar salts is the mixture of potassium and sodium nitrate, which have a melting point above 220 °C (Bauer et al., 2013), and a thermal decomposition limit of 600 °C (Chang, Li, Xu, Chang, & Wang, 2015). These temperatures constitute two of the most critical security constraints for the receiver.

In the hot tank, molten salt is stored at a high temperature (e.g., 565 °C), and a *cold* container holds the salt well above its melting point (e.g., 290 °C). The molten salt is pumped up from the cold tank to the tower, where the solar field radiates onto the receiver the concentrated flux. The receiver then converts this radiant flux into heat. The receiver can be thought of as a *recuperative heat-exchanger* (Winter et al., 1991), which is then used to generate vapor and drive a steam turbine coupled with a generator generating electricity.

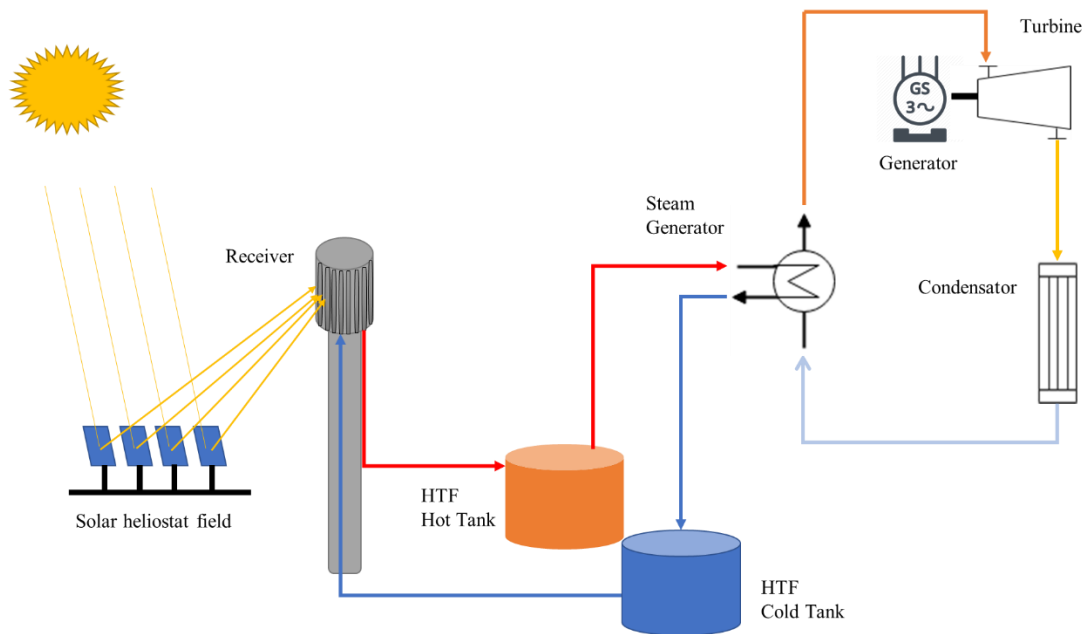


Figure 6. Simplified diagram of a tower solar power plant

In the following sections, each plant's component relevant to this dissertation will be explained.

2.2.1. Heliostats

The mirrors with the task to reflect the direct sun beam rays onto the receiver located at the top of the tower are called heliostats. They must have the functionality to track the sun's movement using two axes, the azimuth and elevation angle, see Figure 7. The number of heliostats in a solar field forces their structure to be cost-effective for this technology to compete with fossil fuel alternatives.

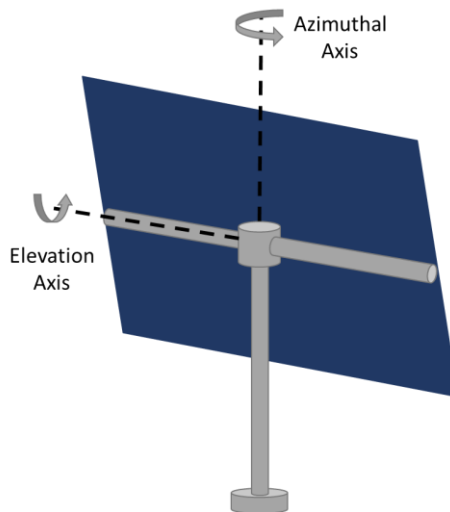


Figure 7. Heliostat's degrees of freedom, azimuth, and elevation.

Most installed heliostats use a T-like structure for their frame, as seen in Figure 8, composed of a vertical column and a torsion axis. The horizontal torsion axis is driven to follow the sun's elevation, while the vertical movement ensures the azimuthal movement. During operation, gravitational and wind loads act upon the heliostat, hence the need for a rigid structure.



Figure 8. Rows of heliostats at the DLR Solar Research Site at Jülich

The rigidity of the heliostat, hence its weight, is an indicator of its cost. New developments are still underway to diminish the total cost of a heliostat while improving its orientation capabilities. The mirror itself consists of facets joined to the metal structure, and the most common material for the facets is a low-iron mirrored glass of 1 to 4 millimeters (Pfahl et al., 2017). The actuator for the drives that move the heliostat is usually a rotary electromagnetic motor. The wind loads, among other factors, affect the precision of the heliostat's aiming point, causing errors.

Before describing the most critical factors contributing to the mentioned errors, it is necessary to introduce the concept of the degraded sun. In the field of concentrator optics, the sun is considered a distant object with an angular radius of 4.65 mrad , and a focused heliostat will form an image of the sun on the receiver, with a radius equal to the focal distance times 4.65×10^{-3} , which means that for a distance of 1 km , the projected image of the sun onto the receiver will have a 4.7 m radius. The sun has been

modeled using a bivariate gaussian function for a system with hundreds or thousands of heliostats. It constitutes a convenient way to handle the errors from each heliostat and avoid having to consider the convolution of the multitude of errors from various heliostats.

Now, for any point in the image plane, the actual image formed by a heliostat can be obtained by summing solar images distorted and displaced by errors in the heliostat. A degraded sun produces in conjunction with a perfect heliostat the same image as the actual sun and the imperfect heliostat. If there is an error function for the heliostat (G), then the equation for the degraded sun is (Winter et al., 1991):

$$D(x, y) = G * S = \int_{-\infty}^{\infty} \int_{-\infty}^{\infty} G(x - x_1, y - y_1) S(x_1, y_1) dx_1 dy_1 \quad (7)$$

Where S is the actual sun distribution, it is convenient to express both functions as bivariate Gaussians, see Figure 9, which can be approximated numerically using Hermite polynomials, a fact that has been exploited in early codes to model solar flux. In state-of-the-art simulations, although depending on the simulation objective, it is preferred to use ray-tracing techniques to model the solar flux.

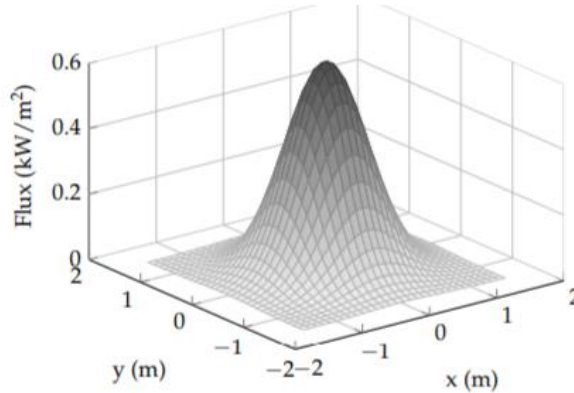


Figure 9. Gaussian distributed flux map of a single heliostat, taken from (Grobler, 2015)

When this function for the degraded sun is convolved with the flux density distribution on the image plane of a point sun formed by a heliostat with no errors, it is possible to obtain the heliostat's intensity distribution with errors. Hence, after using regressions to adapt the parameters to the limb-darkened sun data, the sun is usually represented by a bivariate gaussian with the second moment of $\sigma = 2.77 \text{ mrad}$. Heliostat errors are usually considered random errors and are added in quadrature to the second moment of the sun.

The errors in a heliostat, which have been so far discussed only abstractly, can be traced even from a microscopic level; we will start there to describe them.

Specularity: due to surface imperfections, photons are scattered when reflected from a surface, causing the reflected ray angles to have a distribution profile that has been, and can be, approximated with a Gaussian. The standard deviation of that distribution will be the error added to the second moment of the sun.

Contour: At the mirror's surface, but not on a microscopic level, there are also deviations from the desired surface and its normal. To capture these errors, the standard deviation of angular deviations for the surface normal are obtained, typically in the range from 0.4 to 5 *mrad* (Ballestrín, Burgess, & Cumpston, 2012).

Alignment: These errors occur on a system level, and they involve the canting of the facets of the heliostat. Canting means tilting the mirror facets to aim at the same point. Misalignment due to mechanical loads, has an impact on intercepted power (Sánchez-González, Caliot, Ferrière, & Santana, 2017).

Tracking errors: Changes in the receiver's radiation flux density profile can be caused by each heliostat tracking system. These errors come from an orientation's deviation for the heliostat from the desired aiming point.

All the errors introduced can be combined using the central limit theorem. Instead of using the convolution for every individual contribution and then with the solar

distribution, we can add the squares of all the errors to obtain the degraded sun' second moment (Winter et al., 1991):

$$\sigma_D^2 = \sigma_s^2 + \sigma_{spec}^2 + \sigma_{cont}^2 + \sigma_{align}^2 + \sigma_{track}^2 \quad (8)$$

Both from the industry and the research community, an effort has been made to establish a protocol to qualify heliostats according to commonly agreed performance tests. Within that framework, some parameters described above are considered beam shape parameters and not essential to describe a heliostat performance. During the last Solar Paces conferences, special workshops have consolidated the *Protocol for Optical and Geometrical Evaluation of Heliostats*. A detailed explanation for heliostats' testing guidelines can be found in that protocol (Röger, 2017).

2.2.2. Solar field

The set of all heliostats in the solar power plant constitute the solar field. For an external receiver using molten salts as HTF, the heliostats surround the central tower. Usually, all heliostats are of the same type, and each of them represents a segment of a parabola, reaching concentration factors of 1000. Considering that in solar fields located in the northern hemisphere, the projected area towards the sun is larger in northern heliostats, northern solar fields have fewer mirrors on the southern side. Conversely, in solar fields located in the southern hemisphere, more heliostats are located south of the tower. Figure 10 shows an example of the heliostats' location in a solar field located in the southern hemisphere.

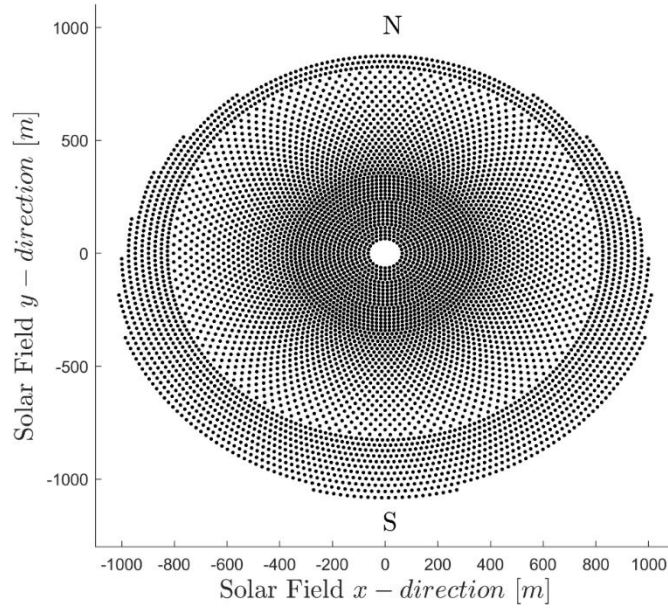


Figure 10. Heliostats in a solar field in the southern hemisphere

Obtaining each heliostat's location in the field at the design stage is a complex optimization problem that depends on several plant, geographical, and meteorological information. One of the problems that must be avoided in the solar field design is the loss of optical efficiency caused by blocking or shading other heliostats. Hence it is necessary to locate them in a way this loss is minimal. Several codes have been developed to solve that problem; one of them is called HFLCAL, developed originally for a research project between Germany in Spain, subsequently purchased and continuously developed by the DLR (Schwarzbözl, Pitz-Paal, & Schmitz, 2009).

2.2.3. Receiver

The receiver's goal is to intercept the high flux density concentrated by the solar field. It must absorb this energy and transfer it to a HTF at a very high temperature. The power block's efficiency depends on the temperature of the HTF and the thermal losses due to radiation and convection. Due to the high temperatures, location high up on a tower, and price, this is perhaps the most critical element in a tower solar power plant.

According to Goswami (Goswami, 2015), there are three kinds of central receivers depending on how their design allows them to absorb radiation. External and cavity receivers, which indirectly use the radiation to transfer energy to the HTF, and volumetric receivers in which radiation is used to transfer energy to the structure's interior rather than its surface, thus decreasing the radiative losses at their inlet.

If concentrated peak flux densities below $1 \text{ MW}/\text{m}^2$ are sought, then external receivers using tubes can be used since the heated area can be small, thus reducing thermal losses (Winter et al., 1991). The central receiver consists of several panels formed by a multitude of long vertical tubes connected at the end in a tubular distributor, which connects the fluid flow between panels. The tubes' material is often a stainless steel alloy, like the austenitic nickel-chromium-based superalloy Inconel 625. With all the panels assembled, the receiver resembles a vertical cylinder.

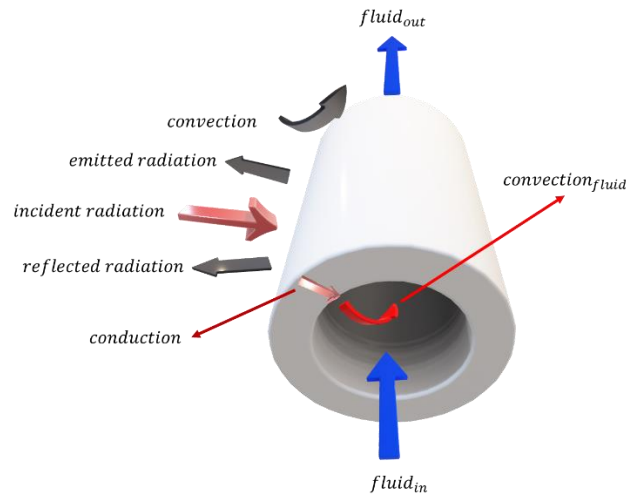


Figure 11. Power incident and losses on a solar tube.

These receivers are the topic of this dissertation, and the basic thermal processes involved with their function will be explained hereafter, and a cross section diagram of the tubes in the panel is shown in Figure 12, the control volume are the tubes of the panel.

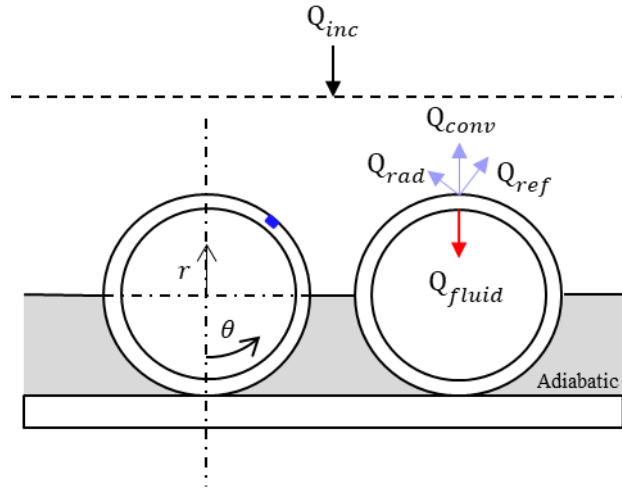


Figure 12. Cross section area of the tubes in a panel and the quantities involved in the thermal model

Reflection: The following equation gives the external tube's wall reflectivity:

$$\rho = 1 - \alpha \quad (9)$$

Where α is the absorptivity of the surface. Improving the metal's absorption properties is achieved by a thin layer of absorbing paint applied to the tubes, e.g., the heat-resistant silicone copolymer coating named Pyromark©, which in turn improves the absorptivity of the tube's surface. The power loss due to reflection is obtained by multiplying the reflectivity by the incident power:

$$Q_{\text{ref}} = \rho Q_{\text{inc}} \quad (10)$$

Radiation: With external receivers, a view factor of one is normally used for calculating radiation losses. The radiated flux, depending on the surface temperature, is given by:

$$Q_{\text{rad}} = \epsilon \sigma A (T_s^4 - T_a^4) \quad (11)$$

Where T_s the surface temperature of the tube, ϵ is the emissivity of the absorbing surface, σ is the Stefan-Boltzmann constant, A is the surface area, and

$$T_a^4 = \frac{\epsilon_{sky} T_{sky}^4 + \epsilon_{gr} T_{amb}^4}{\epsilon_{sky} + \epsilon_{gr}} \quad (12)$$

With ϵ_{sky} and ϵ_{gr} being the emissivities of the sky and the ground respectively. And T_{sky} and T_{gr} are the temperatures of the sky and the ambient.

Conduction: The power transported across the radius of the tube towards the fluid and along the flow's direction can be approximated using Fourier's law of conduction:

$$Q_{cond} = -kA\nabla T \quad (13)$$

Where k is the thermal conductivity of the tube. The conduction within the tubes also serves as “a means of equalizing a non-uniform temperature distribution” (Winter et al., 1991, p.172).

Convection to ambient: The surface temperature of the receiver can reach 800 °C, and can receive winds of to 20 m/s. In this work, we consider the natural convection losses caused by the temperature difference between the tube's surface and the ambient and the forced convection caused by the wind, for which a combined convective heat-transfer coefficient as proposed by Siebers and Kraabel (1984) is used:

$$h_{mix} = (h_{nc}^{3.2} + h_{fc}^{3.2})^{\frac{1}{3.2}} \quad (14)$$

For the natural convection, the receiver is considered a large, high temperature, vertical surface with curvature in the horizontal direction and vertical ribs resulting from the vertical tubes that form the surface (Siebers & Kraabel, 1984). The mentioned ribs contribute to the roughness of the surface, and the proposed equation to determine the Nusselt number, the non-dimensional heat transfer coefficient, is:

$$Nu_{nc} = \left(\frac{\pi}{2}\right) 0.098 Gr^{1/3} \left(\frac{T_s}{T_\infty}\right)^{-0.14} \quad (15)$$

Where Gr is the Grashoff number, or the ratio of buoyant to viscous forces, and can be obtained from the following equation:

$$Gr = \frac{g \beta_{air} (T_s - T_\infty) H_{rec}}{v_{air}^2} \quad (16)$$

Where g is the gravitational acceleration, H_{rec} is the height of the receiver, β_{air} is the bulk expansion coefficient, and v_{air} is the kinematic viscosity of air. Now, it is possible to calculate the heat-transfer coefficient for the natural convection, with k_{air} being the thermal conductivity of the air:

$$h_{nc} = \frac{Nu_{nc} k_{air}}{H_{rec}} \quad (17)$$

In this dissertation, the forced convection heat-transfer coefficient is found using the equations developed by Churchill-Bernstein to calculate the heat transfer from a cylinder in crossflow (Churchill & Bernstein, 1977):

$$Nu_{fc} = 0.3 + \frac{0.62 Re^{1/2} Pr^{1/3}}{\left[1 + \left(\frac{0.4}{Pr}\right)^{2/3}\right]^{1/4}} \left[1 + \left(\frac{Re}{282000}\right)^{1/2}\right] \quad (18)$$

Where Re is Reynold's number or the ratio of inertia to viscous forces; Pr is the Prandtl number, expressing the ratio of kinematic viscosity to thermal diffusivity as a measure of the relative thickness of the velocity and thermal boundary layer. Using the following equations, it is possible to solve for the Nusselt:

$$Re = \frac{\rho_{air} v_{wind} (2 r_{rec})}{\mu_{air}} \quad (19)$$

Where ρ_{air} is the air density, v_{wind} is the wind velocity, r_{rec} is the receiver's radius, and μ_{air} is the air's dynamic viscosity.

$$Pr = \frac{Cp_{air} \mu_{air}}{k_{air}} \quad (20)$$

Where Cp_{air} is the air's specific heat capacity. Afterwards, it is possible to calculate the forced convection heat-transfer coefficient as:

$$h_{fc} = \frac{Nu_{fc} k_{air}}{2 r_{rec}} \quad (21)$$

With both natural and forced convection coefficients, it is possible to find the mixed coefficient and calculate the power losses due to convection:

$$Q_{conv} = Ah_{mix}(T_s - T_{\infty}). \quad (22)$$

Convection to fluid: To account for the transfer of energy from the tubes to the HTF, a fully hydrodynamically and thermally developed turbulent flow of the HTF in a smooth circular tube is assumed, for which the Nusselt number is obtained from the Dittus-Boelter equation (Bergman & Lavine, 2017):

$$Nu_{fluid} = 0.023 Re_{fluid}^{\frac{4}{5}} Pr_{fluid}^{0.4} \quad (23)$$

Where Re_{fluid} is the Reynolds number of the fluid, given by:

$$Re = \frac{\rho_{fluid} v_{fluid} (2 r_{inner})}{\mu_{fluid}} \quad (24)$$

Where r_{inner} is the inner radius of the tube, ρ_{fluid} is the fluid's density, v_{fluid} is its velocity, which is related to the mass flow (\dot{m}):

$$v_{fluid} = \frac{\dot{m}}{\rho_{fluid} \pi r_{inner}^2}$$

Finally, μ_{fluid} is the kinematic viscosity of the fluid, and Pr_{fluid} is the Prandtl number of the fluid:

$$Pr_{fluid} = \frac{Cp_{fluid} \mu_{fluid}}{k_{fluid}} \quad (25)$$

The properties of the HTF are obtained depending on the composition of the molten salt and the fluid's temperature. In this work, a mixture based on 60 %wt. sodium nitrate ($NaNO_3$) and 40 %wt. potassium nitrate (KNO_3) is considered. The properties are found, considering the fluid's bulk temperature in degrees Celsius, according to the following relations (Chang et al., 2015) :

Density $\left[\frac{Kg}{m^3}\right]$:

$$\rho_{fluid} = 2090 - 0.636 T_{fluid} \quad (26)$$

Specific heat capacity $\left[\frac{J}{Kg K}\right]$:

$$Cp_{fluid} = 1443 + 0.172 T_{fluid} \quad (27)$$

Thermal conductivity $\left[\frac{W}{m K}\right]$:

$$k_{fluid} = 0.443 + 1.9 \times 10^{-4} T_{fluid} \quad (28)$$

And Viscosity $[Pa \times s]$:

$$\mu_{fluid} = \frac{22.714 - 0.12 T_{fluid} + 2.281 \times 10^{-4} T_{fluid}^2 - 1.474 \times 10^{-7} T_{fluid}^3}{1000} \quad (29)$$

After having found the Nusselt number for the fluid, it is possible to determine a heat-transfer coefficient inside the pipe:

$$h_{fluid} = \frac{Nu_{fluid} k_{fluid}}{2 r_{inner}} \quad (30)$$

Finally, it is possible to determine the heat transferred to the fluid:

$$Q_{fluid} = A h_{fluid} (T_w - T_{fluid}) \quad (31)$$

2.2.4. Thermal storage and Power block

In this subsection, the relevant technologies associated with two critical subsystems for a CSP plant are explored. First, by presenting the possibilities for thermal storage according to the current technological developments. Within this scope, some key concepts such as the solar multiple and the storage capacity are discussed. And then, the processes by which captured energy can be converted to electricity are discussed.

Thermal Storage

In a fossil fuel power plant, the energy storage is the fuel itself. On the contrary, CSP plants without energy storage can only operate during the day since the fuel is solar radiation, besides being exposed to the weather's influence on the solar resource. In CSP power plants, storing the captured energy enables the plant to be operated even after the sun has set. For instance, Gemasolar in Spain was designed with a 15-hour capacity storage system. A CSP tower can be used as a baseload plant, using an adequately sized storage system and a fossil backup. State-of-the-art storage includes sensible heat storage systems, latent heat, steam accumulators, and thermo-chemical energy storage systems (Sattler et al., 2011).

In sensible heat thermal energy storage systems, a material absorbs or releases heat because of a temperature difference without changing its state. This process can be direct or indirect, depending on whether there is an additional storage medium to the

HTF. Usually, a pressure drop is considered associated with the HTF charge or discharge storage process.

An example of an indirect process is a packed-bed thermal energy storage system, also known as a regenerator. A container is filled with rocks with a high heat capacity; the HTF can be air. The solar tower Jülich, in Cologne-Germany, uses this kind of storage with a more sophisticated ceramic storage material. Among the operation specifications, the storage system could be cycled between 120 and 680 °C supplying a near to 9 MWh capacity. The steel container is shielded from storage heat using ceramic fiber insulation. There are two operating modes: charge and discharge. When charging, hot air from the tower's receiver enters the system flowing downward, forming a moving temperature profile, while in discharge flow's direction is reversed supplying heat to the air loop (Stefan Zunft , Matthias Hänel , Michael Krüger , Volker Dreißigacker , Felix Göhring, et al., 2011). Another example of a direct process involves sand, which makes it environmentally friendly due to the ubiquity of the material near desertic regions where CSP thrives, and a low-cost alternative. The sand would descend through a heat exchanger where a crossflow of air through a porous wall will transfer the heat to the falling sand exiting at a much lower temperature through another porous wall (Sattler et al., 2011).

Direct storage systems are usual in solar power towers, particularly the configuration that uses one cold tank and a hot one. In this configuration, the HTF and the storage medium are molten salts. Usually, the medium is a mixture of sodium nitrate and potassium nitrate, 60 % and 40%, respectively. In the cold tank, the salt must be kept above its freezing point (221 °C). Therefore, when the plant is not in operation, the tank uses an electrical heater to keep it, for instance, at 290°C. In regular plant operation, the salt is heated to nearly over 550°C and then redirected to the hot tank. The power block uses the salt, sometimes via a steam generator, and the salt leaving the heat exchanger would return to the hot tank. An ideal two-tank storage system would have no storage losses and no exergy storage losses, and the discharge capacity

would be equal to the charge capacity (Sattler et al., 2011). Gemasolar, the first commercial solar tower plant using molten salts, includes a 15-hour capacity two-tank storage system. SENER, who operates Gemasolar, expects in 2021 to achieve 24/7 operation at least 30% of the year and already holds the record of 36-day continuous operation for around-the-clock generation (Kraemer, 2020).

Another kind of storage system takes advantage of the heat absorbed and released when a material experiences a phase change. Solid to liquid phase change storage systems can be used in power generation up to 350 °C (Sattler et al., 2011). There is also a storage system consisting of a pressure vessel in which steam is fed into hot water, thus raising the water's temperature by the steam's heat of condensation. For the discharge of the storage, a sliding pressure system can be used in which saturated steam is withdrawn from the vessel. This system is also known as Ruth's storage, and it is used by the solar tower plant PS10 in Spain. Current lines of research consider using capsules of phase-change-materials with melting temperatures between the lower and upper operating saturated steam temperatures of the accumulator, thus reducing the volume required to achieve the needed capacity and reducing in this way investment costs (Michael , Krüger; Selman, Muslubas ; Thomas , Loeper , Freerk Klasing , Philipp Knödler et al., 2020). Finally, there are also thermochemical energy storage systems that use reversible reactions. These systems use endothermic reactions for the charge while exothermic reactions for the discharge, as shown in Figure 13. In other words, excess heat is absorbed by an endothermic reaction, and the products of this process are stored in separate units. These products can then be used for an exothermic reaction, and the heat from this reaction can be used, for instance, to produce electricity.

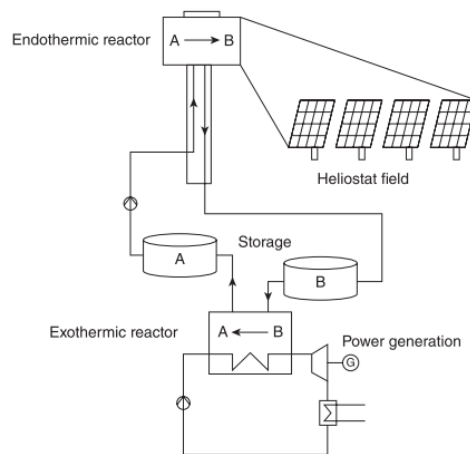


Figure 13. Diagram of a reversible chemical energy storage system, taken from (Ballestrín et al., 2012)

A typical catalytic reaction where the technical feasibility has been demonstrated consists of the endothermic reforming of methane and water at very high temperatures provided by a solar tower, producing a carrier gas with high energy content (Von Storch, Becker-Hardt, & Sattler, 2018). This gas can be transported or used later to produce methane by an exothermic methanation process. The reaction heat is used to generate steam and further drive a power generation block. The use of natural gas as a reactant to supply solar hydrogen seems to be the alternative while large-scale implementation of water splitting reaches technical and commercial maturity (Agrafiotis et al., 2014)(Roeb et al., 2011).

To conclude this section two crucial concepts are introduced. The first concept is related to the design parameters of a solar plant. The solar multiple is defined as the amount of power the solar field can radiate onto the receiver at the design day divided by the power cycle's nominal input power. A solar multiple of 1.5 means that the plant was designed to deliver 50% more thermal power than needed in the generation stage. This apparent overcapacity compensates for months distant from the design point where the available solar radiation would not suffice to reach the necessary nominal thermal power input to the power block. Furthermore, by including a thermal storage

system, the plant would store any excess energy to be used as buffering, pre-heating, or decrease the use of the fossil fuel backup.

Another essential concept is the capacity factor, defined as the ratio of the number of operating hours at the rated output power to the total number of hours in a year, i.e., 8760 h. Revising the performance of installed solar power CSP projects, it is interesting that Spanish projects have increased their capacity factors due to improvements in plant operation. There is also a general global tendency as noted by the IRENA report: “The capacity factors have increased over time as a shift towards newer technologies, with larger thermal storage capacities has coincided with a trend towards the growth of markets in higher irradiation locations” (IRENA, 2018b). Capacity factors over 20% are usual for power plants without thermal storage, while it is expected that the capacity could be increased significantly by including thermal storage (Boretta, 2018).

Power Block

Even though the use of Brayton cycles for the next generation of solar tower plants has been an active line of research, most commercial projects use a Rankine cycle with superheated steam as the working fluid to perform the conversion of the thermal energy concentrated onto the receiver into electricity (Merchán, Santos, García-Ferrero, Medina, & Hernández, 2021). The main components of a conventional Rankine cycle are the boiler, in which the working fluid changes its phase, it is evaporated; the turbine, in which power is generated via the expansion of the fluid using a generator; the condenser, where at low pressure the working fluid is condensed; and finally a pump to increase the pressure of the fluid and make sure there is a constant flow (Karellas & Roumpedakis, 2019).

The power cycle is not able to use all the energy provided by the thermal storage or the receiver, depending on the configuration of the solar plant, and most of this energy has

to be rejected as waste heat to the air-cooled condenser, which works typically at 40 °C (Boretti, 2018). The use of air is preferred since solar towers are installed in desertic regions. Although water cooling requires considerably less capital effort, guaranteeing water supply can be challenging in desertic areas. The disadvantage is that the coolant temperature lies at ambient temperature level. Therefore, the air-cooled condenser might be combined with a hybrid cooling tower and a conventional surface condenser which transports the condensation heat to cooling water; a schematic diagram can be seen in Figure 14 (Hoffschmidt et al., 2012).

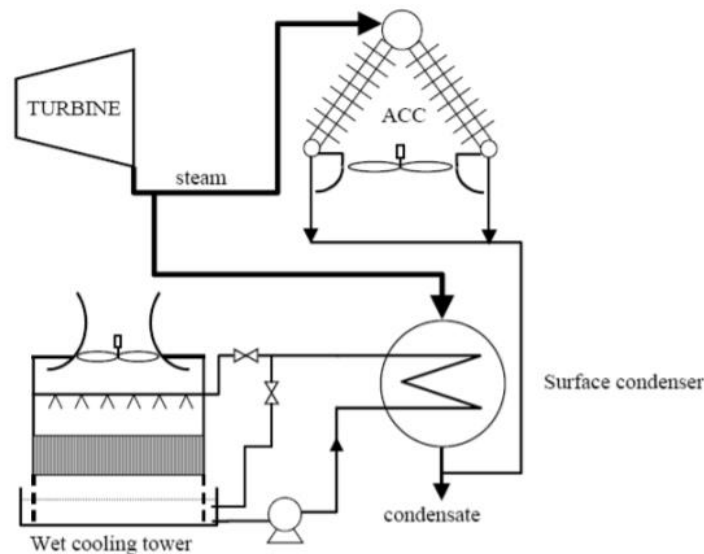


Figure 14. Hybrid wet and dry parallel cooling system, taken from (DOE, 2010)

Furthermore, when designing a solar power cycle, it is essential to consider adjusting the heat recovery steam generator to cope with transient weather conditions. However, it is possible for large plants to achieve high efficiency because the components of the power cycles are state-of-the-art (Hoffschmidt et al., 2012). To increase the cycle's efficiency, steam from the turbines can be obtained in stages to heat feed water to the boilers. The vapor is superheated before the expansion to avoid a liquid fraction that can affect the blades' integrity. Still, material limits might interfere with the low liquid fraction objective. Hence, the vapor is re-heated after the partial expansion (Keith

Lovegrove & Stein, 2012). All these technological advances can be used in a solar power cycle. A schematic diagram for this process is shown in Figure 15.

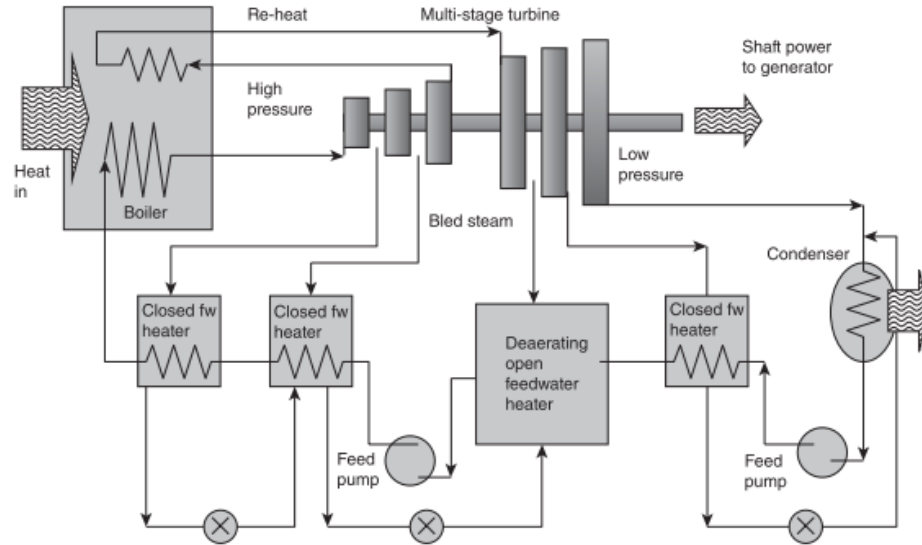


Figure 15. Large steam turbine power plant, taken from (K. Lovegrove & Pye, 2012)

2.3. Central tower plant operation

The daily operation of a solar plant involves specific vital processes, which are explained in this section. Special attention is given to the start-up and shutdown of the solar plant and the power block, cloud passage transient periods, and the transition between the system states' modes of operation. These processes include normal operation, preheating, and standby states. At the end of the section, the focus is turned to the influence of atmospheric disturbances on a solar central tower plant's daily operation because this is a crucial factor embedded within this dissertation's goals.

There is a design basis document for solar power towers prepared after the solar-two project's experience. In this document, the states and transitions between the plant's operational states are divided into two major areas: the energy collection area that groups both the solar field and the receiver, and the energy conversion area that

contains the steam generator and the electric power generator. A detailed description of each area subsystem status can be found in that report (Zavoico, 2001). A general overview of the states and transition between states for the energy collection system is explained in this section; for a detailed description of the energy generation operating modes, the reader is referred to the original document. In the diagram obtained from the design basis document, shown in Figure 16, the states and transitions are depicted.

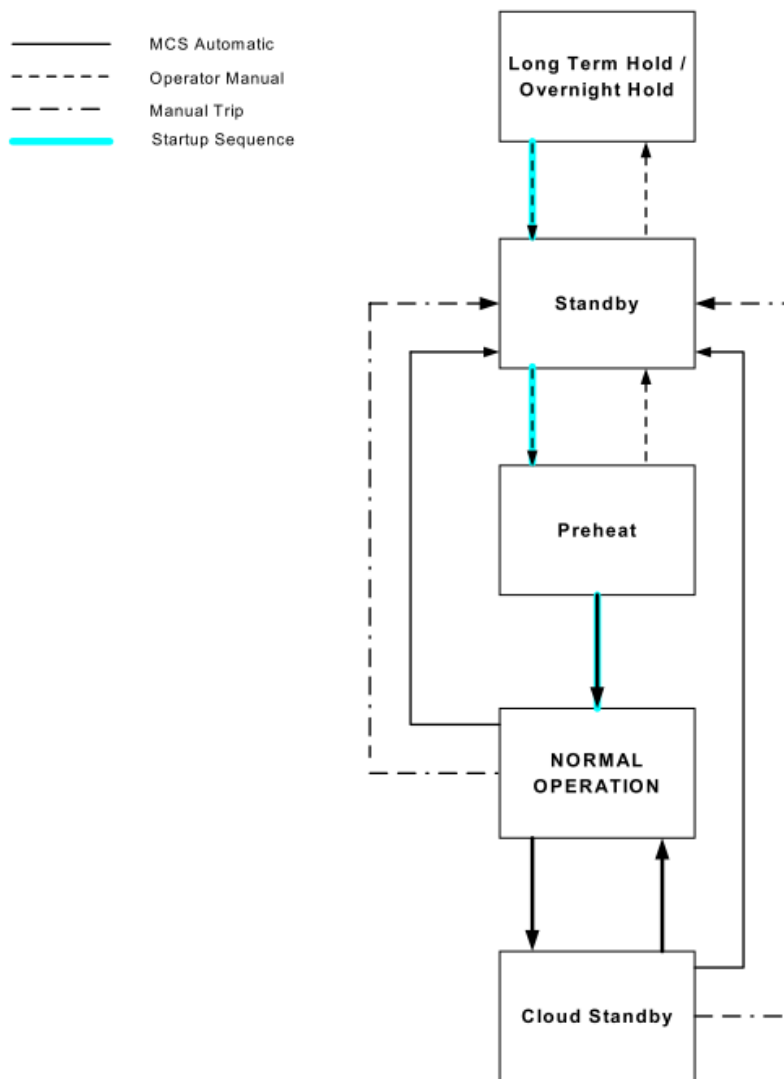


Figure 16. States and transitions for the energy collection system, taken from (Zavoico, 2001)

There are five states for the energy collection area; the Master Control System (MCS) automatically changes between the *Normal Operation*, *Cloud Standby*, or *Standby* state and can also change between the *Preheat* state and the normal operation. In contrast, a Plant Operator changes between the standby state and both the preheat and the *Long Term Hold* states. The operator also can drive the plant to standby mode.

In the first state called ***Long Term Hold***, which is also used as an *Overnight Hold*, the heliostats in the solar field are stowed, the receiver is drained from molten salt, and the electric heat trace circuits are used to avoid freezing of the molten salts are deactivated. In the second state, called ***Standby***, heliostats focus on predefined aiming points away from the receiver; the receiver pump is in operation, guaranteeing recirculation of the HTF. The molten salt flows through the pump, which rises the fluid to the receiver inlet vessel, then bypassed through a line into the downcoming flow. These elements can be seen in Figure 17. This diagram contains the most important elements in the flow circuit of the receiver, starting at the west 1 panel and then crossing over the east side until it leaves the receiver to the east 12 panel. At the bottom of each interconnection between the panels, there is also drain valve.

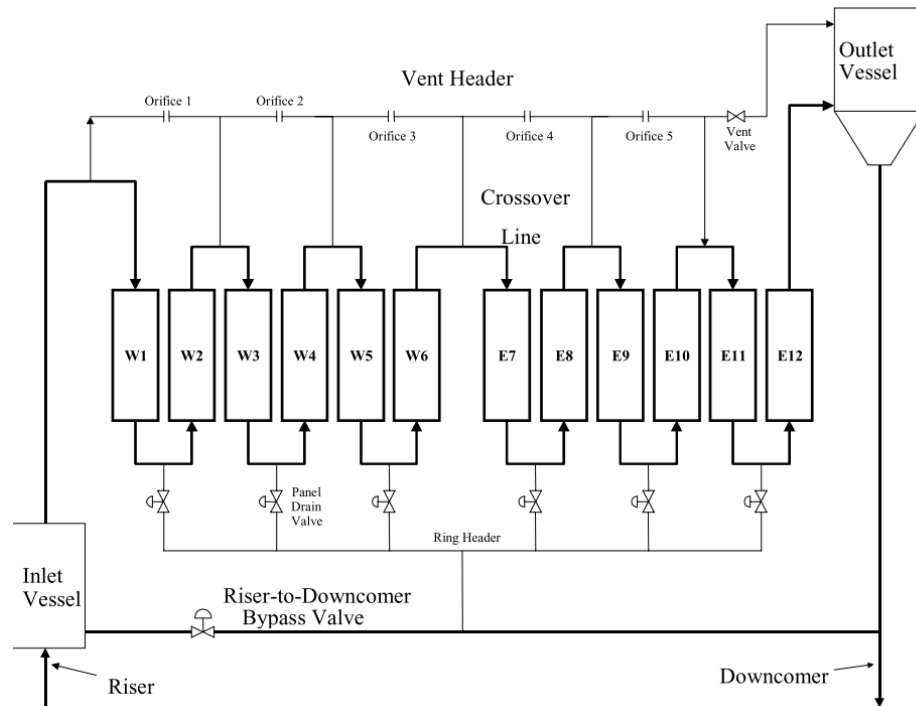


Figure 17. Schematic diagram of the receiver flow circuit, taken from (Pacheco et al., 2002)

In a third state called *Preheat*, the circuits to activate the receiver's heat traces are on. A group of previously chosen heliostats is focused on the receiver; the receiver pump is activated in this state so that salt flows in the riser, the bypass, and the downcomer line. The next stage is the *Normal Operation*. The solar field is focused on the receiver, and a temperature controller seeks to reach and maintain an outlet temperature of 565°C manipulating the mass flow rate in the receiver. Also, the heat trace circuits are deactivated once the normal operation set points are reached. A fifth state is the *Cloud Standby*. All of the available heliostats are focused on the receiver. The receiver flow rate is manipulated to decrease or maintain an outlet temperature of 510°C, under a theoretical clear sky condition. Also, the electric heat trace is not active in this state. There are nine transitions, a more detailed description of the actions taken by the subsystems during the transitions is shown in Figure 18.

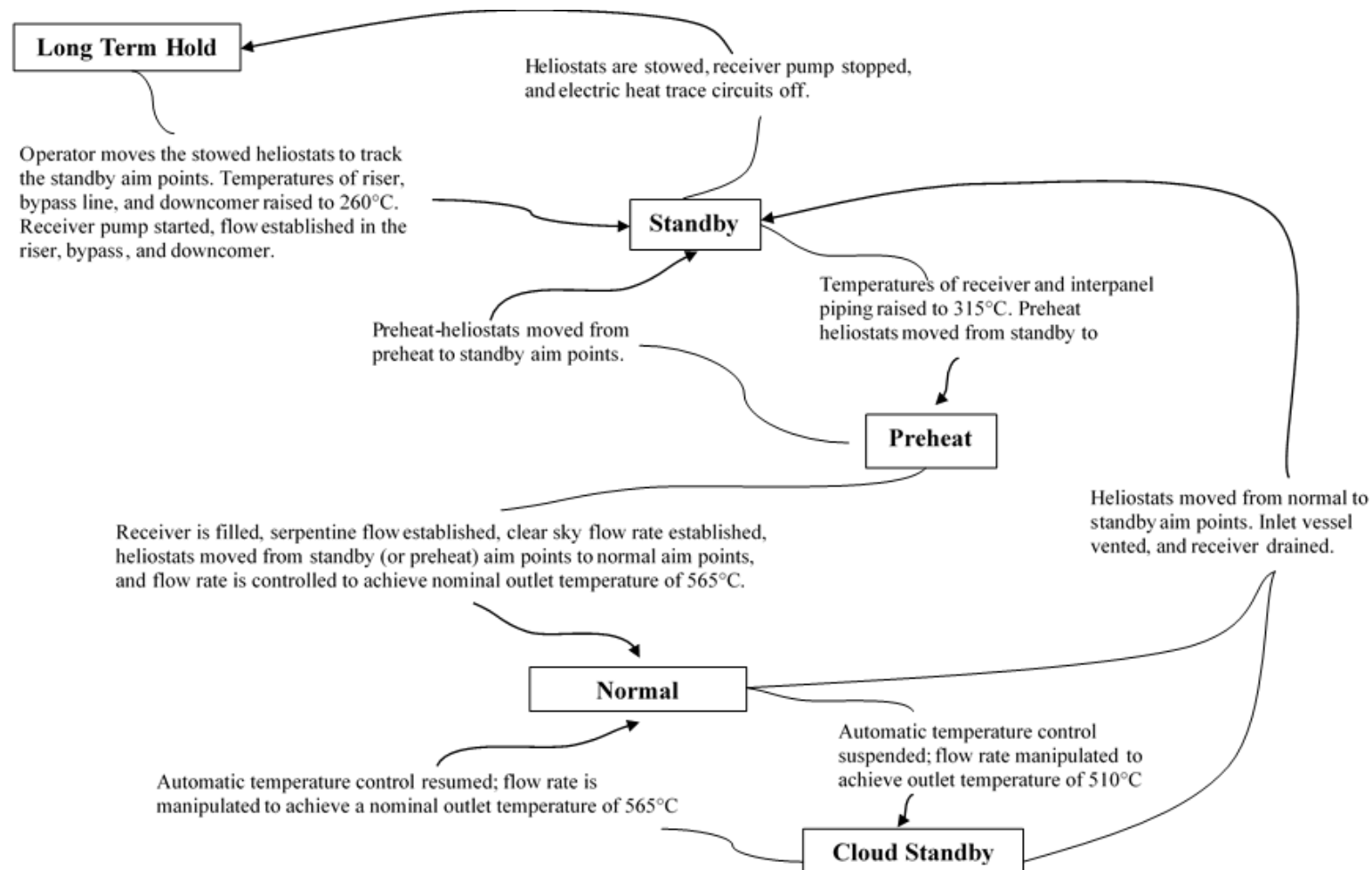


Figure 18. Transitions between states Energy collection system, made by the authors with information from (Zavoico, 2001)

Among the most interesting feature of the Solar Two project is the Heliostat Field Flux Management System and the Preheat processor. The first one includes a Static Aim Processing System (SAPS), which worked on 10-minute intervals. Its goal was to adjust heliostat aim points to minimize spillage and provide a flux approximate to the desired pattern. The Dynamic mode of the Aim Processing System (DAPS) compared predicted flux patterns in short time intervals (few seconds) to remove heliostats contributing to overflux conditions. In addition, the Preheat processor's objective was to reach a temperature between 260 and 380°C on the receiver's surface as fast as possible without overheating the dry receiver tubes. The heliostat field could provide a vertically uniform flux density that could vary azimuthally between 12 and 36 kW/m^2 . The uncertainty appears from local convective losses due to the wind. To accomplish that, a predicted flux density map for each heliostat was obtained with a simulation using current conditions of insolation, sun position, and ambient temperature. The total flux radiated onto the receiver from all tracking heliostats was computed and compared to the desired flux. If the predicted flux was higher than desired at some area, the set of heliostat flux maps was scanned to find the heliostat producing the most flux at that area. Its flux contribution was subtracted in the simulation from the total receiver flux map, repeating this process until no overflux existed. The heliostats causing the higher flux were then directed to stop tracking the receiver.

Another aspect to highlight on the receiver operation is that salt might freeze in the receiver tubes during startup. This phenomenon, which happened in Solar Two, and recent projects like Gemasolar, is due to boundary conditions, specifically high winds or too cold tube clips. It can be addressed by heating gradually the tubes with heat tracers or the solar field.

Before operating the plant, during the commissioning of the solar field and the receiver, it is necessary first to deliver a large amount of salt, which may take months to complete. In Figure 19 the total amount of salt used for Solar Two is shown. Then, it is necessary to melt it, which is a 24/7 operation until completed.



Figure 19. Nitrate salt to be melted at Solar Two (1380 tonnes), taken from (Pacheco et al., 2002)

The melting process can lead to NOX production if the salt contains traces of $\text{Mg}(\text{NO}_3)$. Additionally, depending on the air's moisture, the melting process may promote nitric acid formation (HNO_3). These hazardous gasses and their disposal alternatives are determined depending on environmental regulation, personnel hazards, and corrosion and fire risks to the equipment (Zavoico, 2001).

The first commercial solar power tower was Gemasolar in Sevilla, Spain. In Figure 20, the performance of the plant for a week in summer is shown. The plant can continuously operate 24 hours/day, and the performance is better on clear sky days than on cloudy days. The operation of the plant requires 20 on-site employees, including supervisors, health, safety, and environmental (HSE) personnel, process engineers, and operators. For maintenance, nearly 30 employees, including supervisors, technicians, mechanical and electrical engineers, chemical engineers, and cleaning crews, are needed (Schallenberg, 2013).

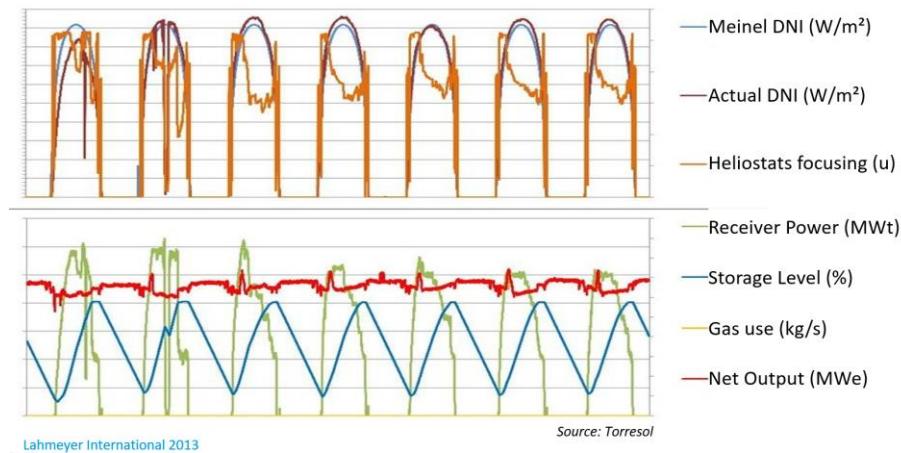


Figure 20. Gemasolar plant behavior during a summer week, taken from (Schallenberg, 2013)

Although not evident from Figure 20, daily variations on the DNI can substantially impact the plant's behaviour. This graph was published by the owner of the solar tower to demonstrate how the plant could operate continuously, for one week, thanks to the Thermal energy storage. The orange line represents the amount of heliostats focused on the receiver, and when the storage level is high, they are defocused. Furthermore, sharp DNI variations as seen on day 2, impact the stored energy.

For instance, for the Solar Two plant, Figure 21 shows how due to atmospheric disturbances, specifically a cloud passing through the solar field, the receiver outlet temperature leaves normal operation bounds. The controller enters the cloud standby state in which mass flow is increased to protect the receiver's mechanical integrity. A key factor affecting the availability of solar radiation on the ground is the extinction of solar radiation due to clouds.

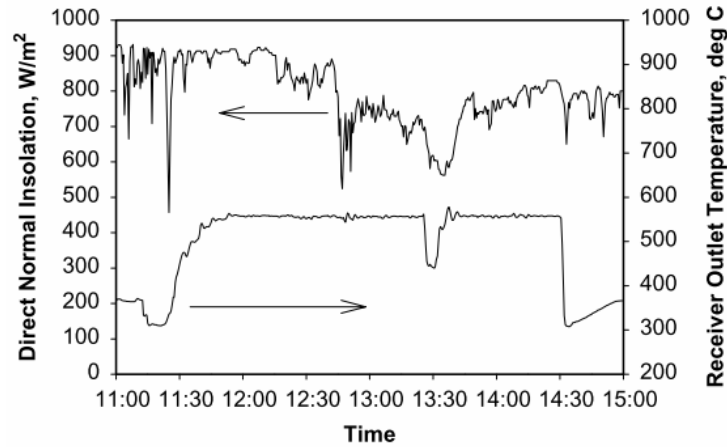


Figure 21. DNI and receiver outlet temperature for a cloudy day in Solar Two. At ~13:25, the receiver state changes to cloud standby, taken from (Pacheco et al., 2002)

2.3.1. Clouds

We have established that one of the primary disturbances in a Central tower plant's daily operation is clouds' effect on the solar radiation available to the solar field. To forecast solar energy in the short term, it is necessary to forecast clouds' evolution (Miller, Heidinger, & Sengupta, 2013). Hence, it is vital to understand what clouds are, how they are classified, and the mechanisms involved in influencing available solar radiation. Furthermore, particular attention in this section is given to modeling attempts carried out by our research group and other approaches to predict their effect on solar radiation and, hence, solar plants' performance.

Clouds are made up of liquid and solid particles much larger than the incoming short-wave radiation wavelengths. They have been classified according to their height in groups. The names for these groups use Latin words or a combination of them to identify them. Hence, *stratus* clouds resemble a flat and uniform layer, *cumulus* clouds develop vertically and tend to be more individual. The root *cirrus* is used to name clouds that form high in the troposphere (higher than 6000 m); ice crystals compose these clouds. The root *alto* is used to designate clouds in a middle level; these clouds can contain liquid water droplets or ice crystals, depending on the altitude and the troposphere's temperature distribution.

The size of a liquid water droplet is on average $10\ \mu m$, which is an order of magnitude higher than the wavelength of the incoming short-wave radiation. Hence the scattering of the light is nearly independent of wavelength. Furthermore, transmittance through a cloud, which is the fraction of direct-beam energy incident on a cloud top transmitted to the ground, decreases as the cloud thickness increases. This is because direct beams entering the cloud will collide with drops and generate diffuse and almost isotropic energy around the individual drops in the cloud. Also, the Sun's zenith distance influences transmittance energy. At noon, transmittance would be greater than at sunrise for thin clouds, while for very thick clouds, the transmittance in visible light approaches zero regardless of the sun hour. The absorption of infrared radiation in clouds is a complex phenomenon because water and water vapor absorb energy differently depending on the wavelength (Fritz, 1957).

The effect of clouds on the atmospheric absorption of solar radiation has been studied actively; however, modeling such phenomena is highly complex. A classical term used to define cloudiness is the fractional cloud cover, used regularly in airports and obtained by any observer looking at the sky. However, it does not appropriately describe the effect of clouds on the surface, such as in the surface's energy balance. The shape, height, and density of clouds affect the radiation on the surface. Elthair and Humphries studied the role of cloudiness feedback in the surface energy balance over the Amazon Forest. They considered the impact of deforestation on large-scale land-atmosphere interactions over rainforests (Elthair & Humphries, 1998). Li used four years of records for the solar flux from space and the earth's surface to evaluate the ratio of mean short-wavelength cloud radiative forcing at the surface to that at the top of the atmosphere averaged over the entire period (R). The cloud radiative forcing is defined as the difference between clear-sky and all-sky net radiation fluxes (Y. Liu, Wu, Jensen, & Toto, 2011). Li found that the effect of cloud absorption is variable in the globe. Also, the ratio R is not a measure to use directly to account for cloud

absorption since other factors influence it. One of these factors is aerosol content in the atmosphere resulting from biomass burning in the tropical region (Li, 1995).

Radiation reaching the earth from the sun is called short-wave since it is concentrated in wavelengths between (0.1 to 6.0 μm). A significant part of the short-wave radiation occupies the visible region of the electromagnetic spectrum. Radiation emitted by the earth's surface, on the other hand, has a much higher wavelength radiation band (3.0 to 100 μm). The shortwave radiation suffers from scattering, and absorption although in a lesser magnitude. Looking at the entire earth's surface, clouds can cover 50 % of it, and the radiation budget is affected by the albedo of clouds and their greenhouse effect. Albedo is the fraction of the incident energy reflected into space. The greenhouse effect explains how both clouds and some gases in the atmosphere absorb and re-radiate longwave radiation in all directions, trapping some energy within the earth's atmosphere. Figure 22 shows the mean values per unit area of the earth's surface for the atmosphere's main energy transfer mechanisms. Clouds reflect, absorb, and emit significant amounts of radiation (Coley & Jonas, 1999). More than a third of the energy reaching the planet is reflected into space. The other part is absorbed by the atmosphere, and only less than 50 percent of the extraterrestrial energy reaches the surface.

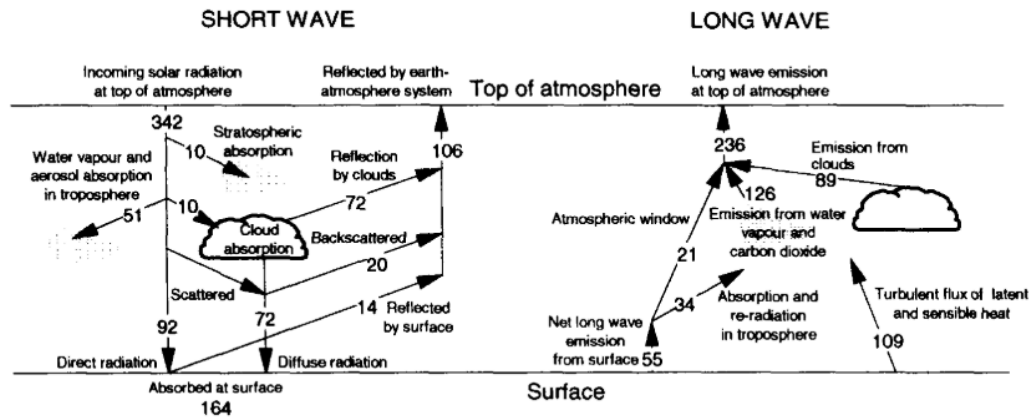


Figure 22. Mean global energy budget of the earth-atmosphere system, taken from (Coley & Jonas, 1999)

In a CSP project, the fuel is the DNI since it is converted into energy and indirectly into monetary returns. The accuracy of the DNI data reduces economic uncertainties. Furthermore, the microclimate of a specific site will influence the DNI. Using information with too large spatial resolutions is not advised, especially in the project's advanced stages. Schlecht and Meyer recommend having at least one year of local DNI measurements to include all seasons' changes.

Additionally, proper use of this data and longer time-series from satellite information that can go back decades would decrease the DNI uncertainty for project planning (Schlecht & Meyer, 2012). A review of techniques to ensure robust solar-radiation datasets, which are deemed essential for the financing of solar power projects, can be found in Vignola et al. Basic terms like Typical Meteorological Year datafiles are introduced as well as requisites to construct bankable datasets which can be used to calculate the probability of exceedance of a level of electrical generation that the power plant will produce over a number of years (Vignola, McMahan, & Grover, 2013). NREL compiled another valuable resource in which the quality and reliability of the DNI are discussed to facilitate developers and researchers so that reliable data about the solar resource available at specific locations can be obtained (Sengupta et al., 2015).

On the other hand, for operational purposes and regarding the necessary matching to be made between demand and production of renewable energy, it is becoming more important to consider the ability to predict in the short-term the yield of CSP plants; this forecast is better defined as follows:

Short-term solar-energy forecasting (e.g., 0–3 h) entails the prediction of fine-scale temporal and spatial details in the down-welling surface irradiance field, including the capture of high-frequency fluctuations in this field due to the passing of cloud shadows or aerosol attenuation; it also accounts for the influence of the regional cloud/aerosol field on diffuse-sky irradiance. To the first order, cloud cover is the primary driver of solar variability, particularly at short-term forecast timescales (Miller et al., 2013, p. 50).

There are numerous data-based approaches to forecast radiation that have been studied recently. For instance, Chu and Coimbra developed a k-nearest neighbor (kNN) algorithm, which provides intra-hour forecasts for the Probability Density Function (PDF) of Direct Normal Irradiance (DNI). They use diffuse irradiance measurements and cloud cover information to provide their forecast. Through quantitative metrics to assess the method's performance for different locations, their algorithm shows better performance than both a persistence- and a gaussian-based probabilistic model when the forecast horizon is greater than 5-min (Chu & Coimbra, 2017). Coimbra and Pedro discuss other methods based on stochastic learning such as artificial neural networks, fuzzy logic, and regression methods like autoregressive moving averages (ARMA) and autoregressive integrated moving averages (ARIMA). They conclude that the forthcoming generation of forecasts, used for the operation of renewable energy plants, will take advantage of deterministic and stochastic approaches in machine-learning environments (Coimbra & Pedro, 2013).

In the UREMA group, the challenge to model clouds has been approached by creating a model for imitating the behavior of cloud shading on the ground by applying a

biomimetic approach, in which a bacterial colony growth is used to model change in cloud shape and motion as seen in the real phenomenon. The approach was quantitatively assessed comparing Fast Fourier Transform markers with real cloud images (J. M. García, Padilla, & Sanjuan, 2016). Consequently, the model was tuned with an objective function extracting the characteristics of an actual set of available DNI measurement time-series. The results of that work showed that the model after the tuning procedure could provide responses similar to measured direct solar radiation transients (Jesús García, Portnoy, et al., 2018).

For short periods, timescales in minutes, the clouds' size and movement changes have been characterized in several works using linear assumptions applied to observations. This is also known as nowcasting. It can be regarded as a deterministic problem in which a measuring system determines clouds' position in space and track their movement, using All-Sky Imagers (ASI). Furthermore, this system must include a method that estimates the clouds' optical properties, which affect the solar radiation on the ground (Miller et al., 2013). Urquhart et al. discuss in detail the challenges, possible applications, and existing Sky-Imaging Systems for Short-Term Forecasting (Urquhart et al., 2013).

One of the state-of-the-art ASI-based nowcasting systems for solar radiation is based on 4-ASI and a voxel carving-based cloud modeling algorithm together with a cloud segmentation independent stereoscopic cloud height and tracking detection (B. Nouri et al., 2019). A voxel is a volume element, like a pixel with a defined edge length in each spatial direction. Each cloud detected has attributes, height, position, volume, surface area, transmittance, an associated motion vector.

The cloud height detection method is based on a novel approach that does not depend on cloud detection to find cloud speeds (P. Kuhn et al., 2018). Moreover, the cloud's height calculation uses the cloud speed as proposed by Wang et al. (Wang, Kurtz, & Kleissl, 2016). In Figure 23, the creators of this system show the cloud models in each

direction stemming from the nowcasting system before the height detection method is used, and after each cloud has been assigned a value for the attribute of height.

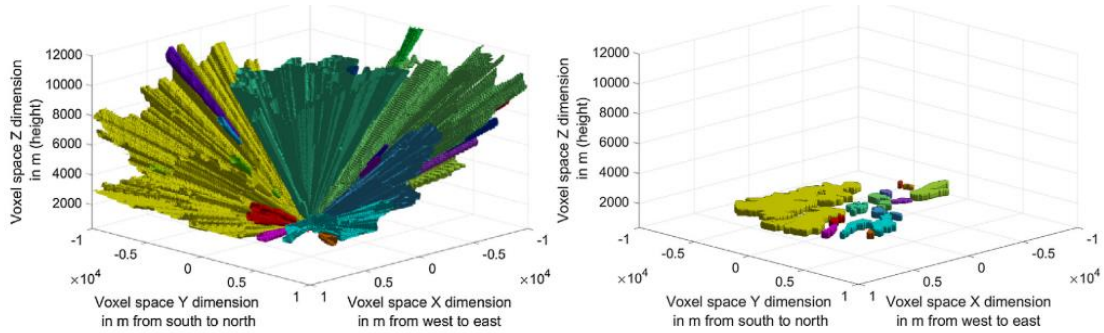


Figure 23. Cloud models in voxel space, before height detection (left) and final model (right), taken from (B. Nouri et al., 2019)

This system's accuracy is affected by its capacity to detect the cloud's height and to track its movement. The system's predictions have been evaluated after comparing in a 30-day interval the height with a ceilometer and the movement with the results from a shadow camera system. More information on this exciting system can be found in (P Kuhn et al., 2017). This shadow camera system uses photos of the ground from an elevated position and solar radiation measurements to derive spatially resolved irradiance maps. After evaluating the results, the authors concluded that the accuracy of ASI systems depends on weather conditions. High accuracy is expected from single low-layer cloud conditions with optical thick cumulus clouds. A significant challenge is higher clouds and multilayer conditions, and they suggest higher image resolution cameras for ASI-based nowcasting systems (B. Nouri et al., 2019).

A recent study from the DLR shows that using an ASI-based system's spatial nowcasting capacities, optimizing parabolic-trough power plant operation in variable irradiance conditions is possible. Using two years of data from ASI-based systems, they created temporal and spatial DNI-variability classes, where the classification was made considering self-developed indices. For the temporal case, they classify the DNI from clear sky to overcast. The spatial class used two indexes: the area covered in the

solar field and the ratio between the average DNI in shaded areas and a clear sky. Using these indices, spatial DNI-Variability was classified into *Sunny conditions*, *Low spatial DNI variability* (clouds with high transmittance), *High spatial DNI variability*, *Intermediate spatial variability* (most of the solar field is shaded with thin clouds), and *Low spatial variability* (overcast or clouds with low transmittance).

Both temporal and spatial classes were combined into five classes. In Figure 24 it is shown a sample day with a point DNI measurement from a pyrheliometer and the classification of the DNI-variability. They test two different controllers and a reference controller in a simulated parabolic-through power plant. The reference controller uses two pyrheliometer signals in a feedforward loop to determine the adequate mass flow depending on actual irradiance. The other controllers use DNI information from the ASI nowcasting system, and the controller's parameters have been optimized for each combined DNI-variability class. The class-dependent controllers outperform the reference controller. (B. Nouri et al., 2020)

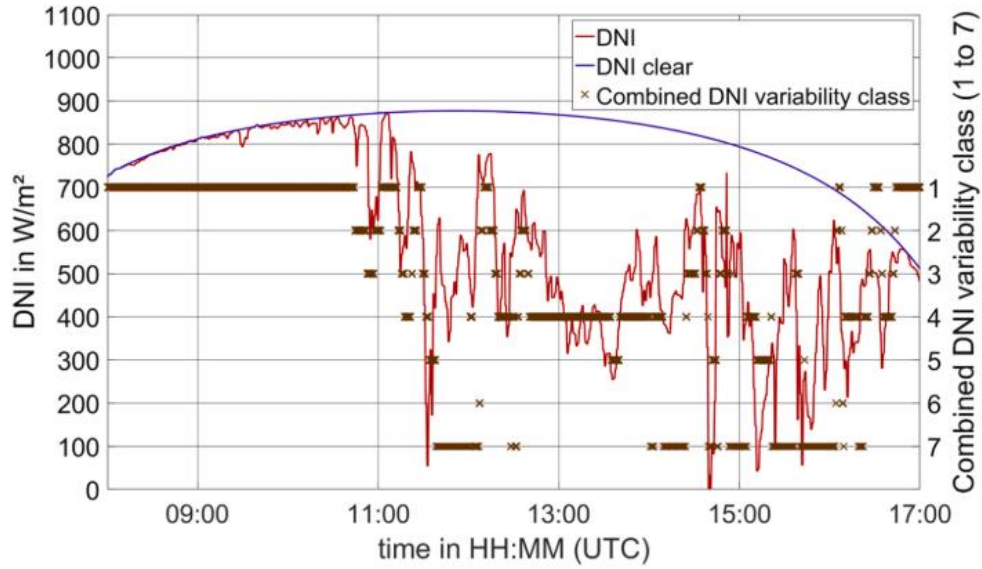


Figure 24. DNI Variability classification for a cloudy day on a CSP, taken from (B. Nouri et al., 2020)

2.3.2. Thermal stress on the receiver's tubes

The problem of finding the thermal stresses in a tube subject to a steady non-axisymmetric temperature distribution $T(r, \phi)$ is solved for a thick cylinder, of inside radius a and outside radius b , by superposing the results of a non-axisymmetric and the axisymmetric solution (Hetnarski & Eslami, 2009a). After demonstrating that terms in a Fourier series for the temperature distribution with an order superior to one do not contribute to the thermal stress, the temperature in the tube is represented by the following series:

$$T(r, \theta) = F_0(r) + F_1(r)\cos\phi + G_1(r)\sin\phi \quad (32)$$

Where

$$F_0(r) = (T_a - T_b)\ln\left(\frac{r}{a}\right) + T_a \quad (33)$$

$$F_1(r) = \frac{F_{10}}{r} + F_{11}r \quad (34)$$

and

$$G_1(r) = \frac{G_{10}}{r} + G_{11}r \quad (35)$$

Furthermore, if a linear variation of the temperature is assumed for the temperature in x and y directions, the terms associated with F_{11} and G_{11} do not produce thermal stress. Superimposing the solutions for the stresses caused by the axisymmetric and the non-axisymmetric temperature distribution yields the following approximation of two-dimensional thermoelasticity:

Radial stress:

$$\begin{aligned} \sigma_{rr} = \frac{E\alpha(T_a - T_b)}{2(1-\nu)} & \left[-\ln \frac{r}{a} + \frac{b^2}{b^2 - a^2} \left(1 - \frac{a^2}{r^2} \right) \ln \frac{b}{a} \right] \\ & + \frac{E\alpha r}{2(1-\nu)(a^2 + b^2)} \left(1 - \frac{a^2}{r^2} \right) \left(1 - \frac{b^2}{r^2} \right) (F_{10} \cos \phi + G_{10} \sin \phi) \end{aligned} \quad (36)$$

Tangential stress:

$$\begin{aligned} \sigma_{\phi\phi} = \frac{E\alpha(T_a - T_b)}{2(1-\nu)} & \left[-1 - \ln \frac{r}{a} + \frac{b^2}{b^2 - a^2} \left(1 - \frac{a^2}{r^2} \right) \ln \frac{b}{a} \right] \\ & + \frac{E\alpha r}{2(1-\nu)(a^2 + b^2)} \left(3 - \frac{a^2 + b^2}{r^2} - \frac{a^2 b^2}{r^4} \right) (F_{10} \cos \phi + G_{10} \sin \phi) \end{aligned} \quad (37)$$

Axial stress:

$$\sigma_{zz} = \nu(\sigma_{rr} + \sigma_{\phi\phi}) - E\alpha(T - T_0) \quad (38)$$

Where T is the temperature of the axial element, T_0 is a reference or stress-free temperature, E is Young's modulus, ν is the Poisson's ratio, and F_{10} and G_{10} are arbitrary constants that must be determined from the temperature distribution.

2.4. Feedback and feedforward control strategies

The idea behind automatic process control is to maintain process variables at the desired setpoint or within an acceptable margin to follow a trajectory. Industrial processes are dynamic systems from which essential variables can be measured. Based on that information, a controller makes decisions and acts upon the system through actuators. In a closed-loop controlled process, the setpoint and the controlled variable are compared, and this error signal enables the controller to decide a corrective action. To act, the controller adjusts a manipulated variable, thus maintaining the controlled variable at its setpoint (C. A. Smith & Corripio, 2006). Consequently, if a disturbance affects the dynamic process, the measured deviation of the controlled variable will motivate the controller to drive the system back to the desired setpoint, hence compensating for disturbances. The described flow of information between sensors, controllers, and actuators is a feedback control strategy. Furthermore, if the controller has the advantage of having information regarding the disturbance, a feedforward control strategy can be implemented. The characteristics of both control strategies are presented in the following section.

2.4.1. Feedback Control

In a feedback control-loop, there is a controlled process variable $c(t)$, a setpoint or desired value for that variable $c^{set}(t)$, an error signal $e(t)$ stems from the difference between the setpoint and the process variable, and a controller output signal $m(t)$ which conveys the actuator how to use the manipulated variable to stir the process in the direction that decreases the error signal. Usually, industrial processes have a defined operation point; therefore, it is convenient to work with deviation variables from a steady-state operating point. Hence, these new variables appear:

$$C^{set}(t) = c^{set}(t) - \overline{c^{set}} \quad (39)$$

$$C(t) = c(t) - \bar{c} \quad (40)$$

And

$$M(t) = m(t) - \bar{m} \quad (41)$$

The region of operation of industrial processes tends to be around a point of operation, \bar{c} and \bar{m} are the steady-state values for the controlled variable and the controller output, and $\overline{c^{set}}$ is the reference signal for the control loop at these steady-state. Thus, it has proven powerful to obtain in case the system can be represented by the linearization of a nonlinear system of equations, or if the system behaves linearly, a representation of the system using the Laplace transform (Åström, 2006). This mathematical tool offers the advantage of converting a set of ordinary differential equations into algebraic equations in the form of transfer functions. For instance, for the setpoint:

$$C^{set}(s) = \mathcal{L}\{C(t)\} = \int_0^\infty C(t)e^{-st}dt. \quad (42)$$

Furthermore, after transforming the set of differential equations, it is possible to establish a transfer function as the ratio between the output and the system's input. In Figure 25, a simplified example of a closed-loop control is shown, with a transfer function for the controller $G_C(s)$ relating the error $E(s)$ and the controller output $M(s)$. Moreover, the process transfer function, $G_P(s)$, relates the output signal of the controller with the process variable $C(s)$. The units shown in the block diagram correspond to percentages of the controller output range for %CO, and in the case of the measured process variable, the units refer to the percentage of the range of the sensor/transmitter pair %TO.

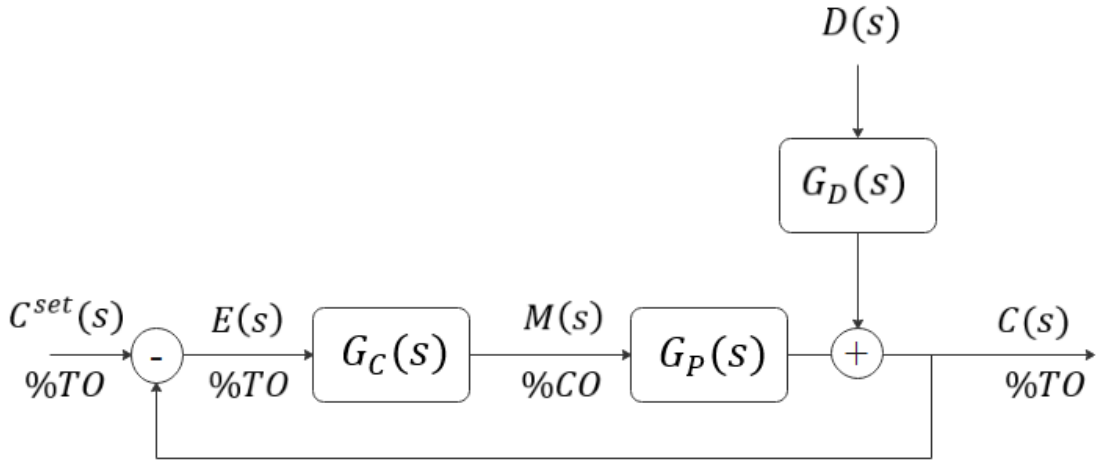


Figure 25. Block diagram for a closed-loop feedback control strategy

If a disturbance, $D(s)$, enters the system it propagates through and its effect on the process variable can be modeled by the transfer function $G_D(s)$; only when the process variable has changed can the controller try to correct the effect of the disturbance by performing a control action.

2.4.2. Feedforward Control

In the case of being able to identify a disturbance that affects the process variable to be controlled, it is possible to create a feedforward control strategy and avoid having to wait until the disturbance propagates through the system and is manifested in the process variable to take a control action. In Figure 26, both feedback and feedforward are illustrated. Here the disturbance $D(s)$ affects the controlled variable via the transfer function $G_D(s)$.

The disturbance is measured, which is represented with the transfer function $H_D(s)$ and this information is used by the controller $G_{FF}(s)$ to determine a controller action $M_{FF}(s)$ which is added to the controller action of the feedback loop.

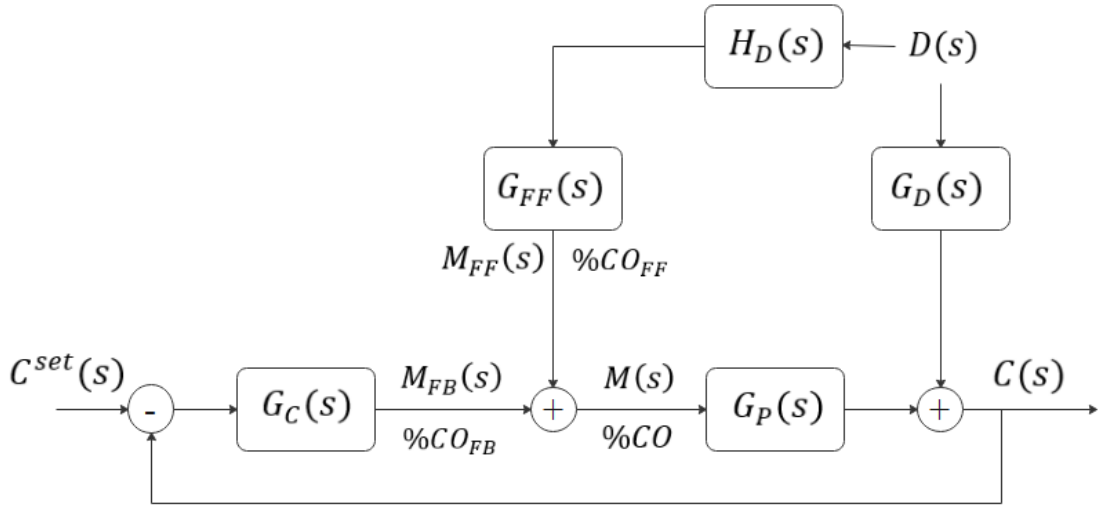


Figure 26. Block diagram for a closed-loop feedback control strategy with feedforward compensation

The advantage of the feedforward strategy is that considering the disturbance's information can make the controller react faster to the dynamic changes propagated to the system, thus providing faster compensation to the disturbance.

3. CONTROL STRATEGY USING PREDICTION DATA

Within this chapter, the major contributions of this dissertation are presented.

The first contribution is a novel flux-feedback control strategy that maintains the flux density distribution projected onto the receiver by the solar field under operational constraints while at the same time reducing the spillage, i.e., the energy not absorbed by the receiver. Most of the strategies proposed to manage the solar field found in the literature are based on optimization techniques. Few works have explored the advantages of feedback control to manage solar fields. This line of research has proposed controllers in which the management of the solar field uses temperature feedback having as constraints the flux limits. However, the results did not promote a homogeneous distribution of the flux projected onto the receiver. The strategy developed in this dissertation accomplishes both fulfilling flux limits and promoting a homogeneous flux on the receiver. This strategy is explored in section 3.1. One of the proposed control strategy applications stems from its ability to rapidly find a near-optimal aiming point configuration, as explained in Chapter 4. The dynamic behavior of the proposed strategy is analyzed using data from a solar radiation nowcasting system (WobaS System). Therefore, a detailed description of the nowcasting system, its characteristics, and drawbacks are provided in section 3.2.1. Using the spatially resolved information from the short-term prediction system as if it were the actual radiation over the solar field, a method is proposed to derive intra-minute data from the nowcasting system. From the 30 *sec* sampled data available from the WobaS system, a 5 – *sec* sampled dataset is generated and used to test the proposed feedback strategy in a static (pseudo-dynamic) simulator. The goal of this testing framework is to analyze the behavior of control strategies to atmospheric disturbances. The static (pseudo-dynamic) simulator is presented in this work.

This work's second contribution is the novel treatment of the forecast information available with the WobaS dataset. There are no approaches in the state of the art to use

forecast information to improve the control of the solar field in solar towers. An adaptive control strategy concept using a feedforward architecture is explained, and the implementation of the proposed controller based on the data from the nowcasting system is discussed in section 3.3.

The third contribution of this dissertation is the development of a measuring system using a solar tracking system to obtain direct and diffuse solar radiation and deliver intra-minute solar radiation measurements in Barranquilla. The system's design is explained in section 3.4, together with an outline towards a new research line once the measuring system is installed and operative.

In the last section of the chapter, the proposed adaptive control strategy with feedback compensation is presented as a whole, describing its advantages, shortcomings, and future possible research paths.

3.1. Novel flux-feedback control strategy

Traditionally solar fields are managed by having a discrete set of aiming points and an optimization strategy. Additionally, a module, which considers measurements and simulations, determines the dynamic state of the solar field, and the heliostats that most likely contribute to overflux conditions are removed from tracking the aiming points. These heliostats are then stowed in a safe position. However, a feedback control strategy would add these management systems with the capacity to compensate for dynamic changes on measurable plant variables and fuse other sources of information. The essential elements of a control strategy include controlled plant variables, manipulated plant variables, the controller architecture, and the logic employed by the controller to determine its actions. The controller used the measured plant variables and makes decisions that determine the values for the manipulated variables, keeping the controlled variables at the desired setpoint or following a predefined trajectory.

In this dissertation, controlled variables are the highest exceeding flux values for a bidimensional grid, representing the receiver's surface. On the other hand, the manipulated variables are two proxy variables (*dispersion* and *vertical distance to the centroid of a group*), enabling the controller to decide both the elevation and the azimuthal angle for all heliostats belonging to a particular group. These controlled and manipulated variables will be explained in detail in the following section and how they are used within the controller and the proposed control architecture.

The control strategy, which will be explained in this section, assumes that a flux measurement irradiated onto the receiver by the solar field is available for the control strategy. In this work, the flux is obtained from an optical ray-tracing simulator developed by the Institute of Solar Research from the German Aerospace Centre (DLR). The simulator is called STRAL and is a fast ray-tracing tool for high precision calculation of heliostat fields' flux density distributions (B. Belhomme, Pitz-Paal, Schwarzbözl, & Ulmer, 2009). The tool was licensed for this research.

The solar flux distribution on the receiver's surface could be reconstructed using photometers measurements as it was done for the feedforward control algorithm from the Solar Two project (Bradshaw et al., 2002). Röger et al. discuss other techniques to measure flux distributions in large-scale receivers (Röger et al., 2014).

To discuss the control strategy, first, the controlled variables will be introduced. A description of the manipulated variables follows this. Finally, the controller logic and architecture will be addressed.

3.1.1. Controlled variables

Ultimately the goal of the control strategy is to find a homogeneous flux density distribution on the receiver while fulfilling operational constraints. Each area of the receiver is assigned to a group of heliostats, and each time step, the highest exceeding flux value for these areas is found. The controlled variable for each heliostat group is the difference between the AFD and this single highest exceeding flux value. For this

purpose, the concept of allowable flux density is used in this dissertation. The AFD typically considers permanent damage which can be caused to the receiver due to corrosion or thermally induced mechanical stress (Sánchez-González, Rodríguez-Sánchez, & Santana, 2020a), in Chapter 4 the way it was calculated in this dissertation is explained.

The solar flux distribution on the receiver's plane is a three-dimensional surface, where each point in the cartesian grid corresponds to an incident flux value. It is possible to calculate the difference between the AFD and the actual flux radiated onto the receiver for every point in the receiver's plane.

In Figure 27, two data points are shown from groups labeled 1 and 25.

$^1(\text{AFD} - \text{Flux})_{x_1, y_1}$ refers to the difference at the point (x_1, y_1) used by the controller for Group 1, and $^{25}(\text{AFD} - \text{Flux})_{x_3, y_{25}}$ refers to the difference at the point (x_3, y_{25}) as used by the controller for Group 25.

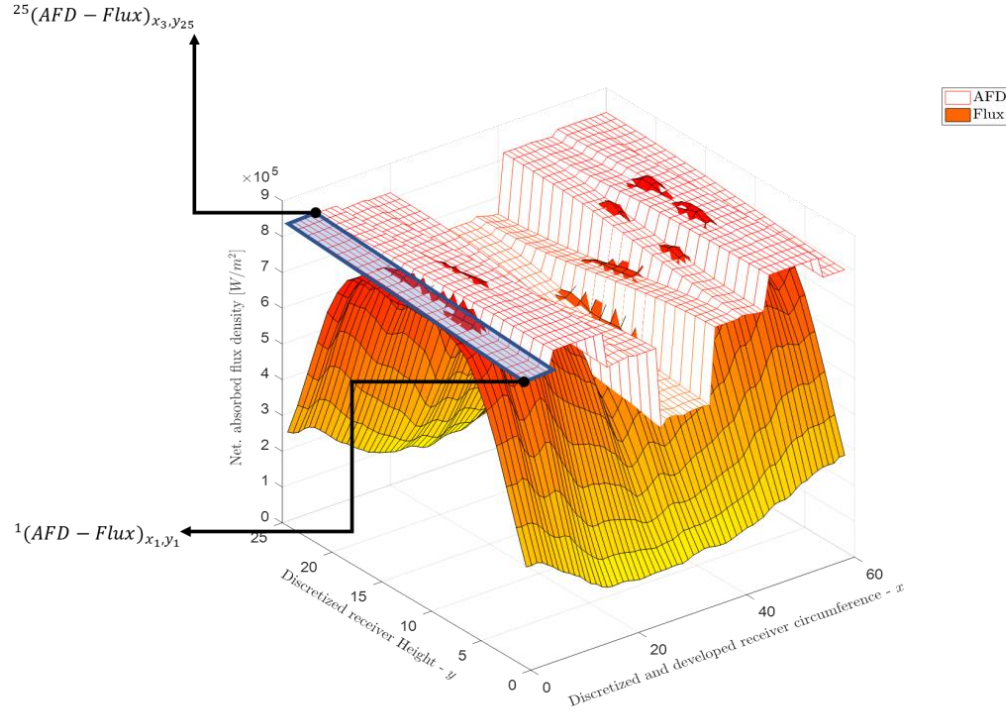


Figure 27. Difference between the AFD and the incident flux on the discretized receiver's surface plane

There is a singular controlled variable per each group of heliostats in the solar field. It is defined as one of the local differences between the allowable flux density and the incident flux in the panel's surface plane. The goal of this work is to reduce the problem's dimension. Therefore, every iteration, a *low selector* (LS) finds the most negative or the smallest value for the difference between the AFD and the incident flux obtained with the simulation based on STRAL. Each group of heliostats in the solar field is assigned a panel section, as explained in the following sections. The selected difference in that area of the panel is the controlled variable for the group of heliostats assigned to that area, i.e., the highest exceeding flux value.

3.1.2. Manipulated variables

The solar field is composed of thousands of heliostats. Deciding the reference for the azimuthal and elevation angles for each heliostat's local controller is a problem that is

currently solved by an optimization algorithm. The sun's position determines a baseline aiming point, and through simulations, heliostats that might induce undesired flux deviations on the receiver's surface are identified from previously established boundaries. Several approaches view this as a discrete optimization problem, in which for a fixed number of aiming points and safety constraints, the algorithm yields an optimal aim point configuration. This formulation results in a hard problem. The search space size is given by the number of possible aiming points elevated to the number of heliostats. Going from 2650 to 6483 heliostats, the search space grows considerably (see Figure 28).

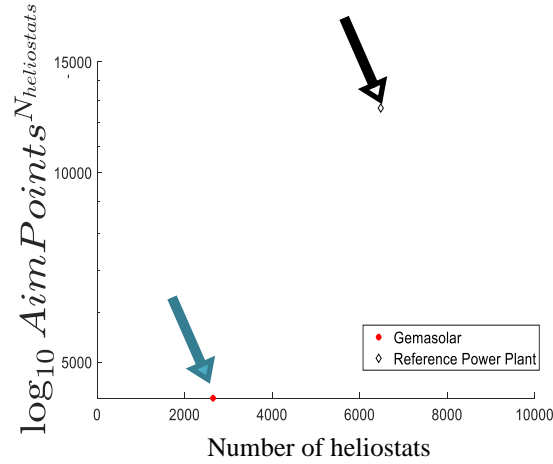


Figure 28. Combination of aiming points and number of heliostats for Gemasolar and the reference power plant

This optimization depends on mass flow and cloud events and is susceptible to modelling errors, such as tracking errors of heliostats. Alternatively, this dissertation approaches this subject as a control problem to reduce the impact of modeling errors and compensate for disturbances. And instead of finding the value of both angles for each heliostat, i.e., thousands of variables, we take advantage of the possibility of controlling the positions of aiming points for groups of heliostats with only two variables per group. These variables are the **Dispersion** of the group, or how close the aiming points are to each other, and a proxy variable, Y_{centroid} , for the distance to

the receiver's equator for all the aiming points in a group. Garcia et al. referred to the desired behavior as a *valve analogy* since the dispersion of the aiming points can be seen as a valve that regulates the flow in a fluid pipeline and gives a detailed description of heliostats' movements (J García et al., 2017). A conceptual diagram of the proposed controlled variables is shown in Figure 29. The *Dispersion* for a group of heliostats is related to the size of the image formed by their aiming points. A highly dispersed group covers a higher surface on the receiver. The variable $Y_{Centroid}$ refers to the position of the centroid of the image of the aiming points measured from the receiver's equator towards the edges of the receiver. By constructing a set of rules, a resulting swarm-behavior for groups of heliostats is achieved. It is explained briefly in the following subsection.

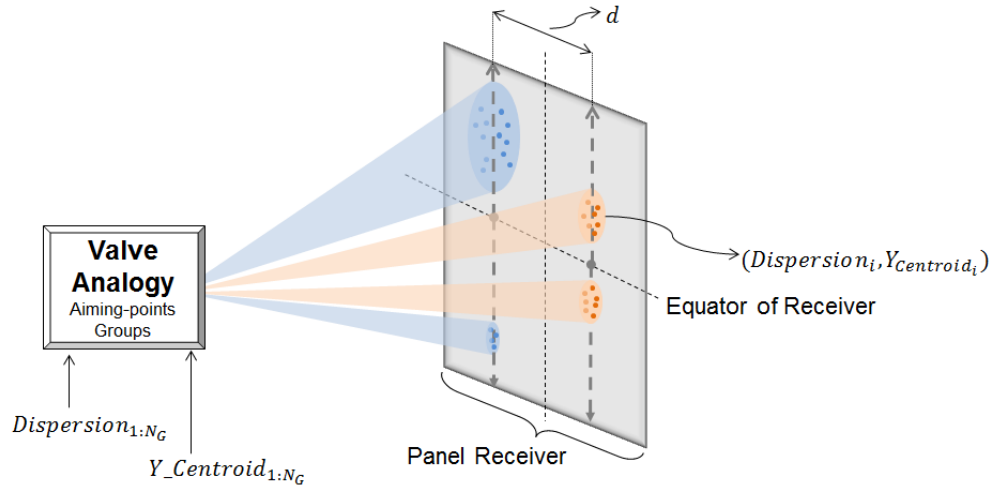


Figure 29. Conceptual diagram of the proposed manipulated variables

Molten salt external receivers are composed of multiple panels, which hold several tubes through which the HTF is transported. Parameter d , in Figure 29, determines a distance that separates the centroids of the groups assigned to one panel, promoting a more homogeneous distribution of the incident flux. This parameter then becomes a path from the equator to the receiver's edges, which the centroid of the group of aiming

points follow. Thus, for the example shown, for a panel with four independent areas, there are eight manipulated variables, $Dispersion_i$ and $Y_{Centroid_i}$, with i varying from 1 until the number of groups, in this case $N_G = 4$.

The position on the receiver of the aiming points is related to each heliostat's angular setpoints in the solar field. To be able to manipulate thousands of position signals, groups of heliostats are established. Together with the series of rules from the *Valve Analogy* (Jesús García, Chean Soo Too, et al., 2018), this technique permits manipulating all heliostat's angular positions in a group, with only the pair of variables discussed. The valve analogy relies on movements from aiming points which are calculated using rules from an agent-based logic. Each individual movement combined results in a swarm behavior because every aiming point considers the movement of all the other aiming points in the group.

Swarm behavior of aiming points in a group

For each group of heliostats, displacements for the aiming points are calculated. Each aiming point attempts to reach the group's centroid while maintaining a circular boundary (of an assigned radius) from each other aiming point. The radius becomes a constraint to the center of neighboring aiming points. Additionally, the centroid of the group also moves, attempting to coincide with the aiming point assigned to the group ($Y_{Centroid}$).

Every iteration, a probability distribution is used to determine the proposed radius surrounding every aiming point. The distribution itself depends on a pre-defined order for each heliostat within the group. Which is implemented by defining a proxy variable x , inside the range of the probability function. Hence, the value of k_{disp} , as shown in Figure 30 and Equation (43, determines whether a group is either dispersed or concentrated.

$$r = \frac{k_{disp}}{1 + \left| \frac{x}{k_{disp}} \right|^{2k_{disp}}} \quad (43)$$

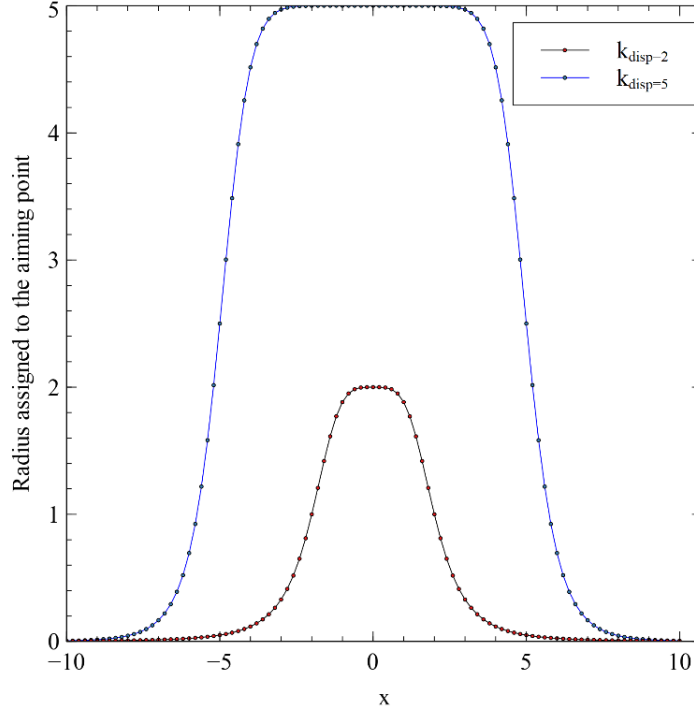


Figure 30. Density function used to assign the radius that determines a movement constraint for the aiming points.

A contribution from this dissertation to the valve analogy model is introducing a new parameter, d (see Figure 29), which for a large receiver offers the advantage of better distributing the solar field's energy to achieve a more homogeneous flux on the receiver.

3.1.3. Controller and architecture

The manipulated variables determine the angular position for each heliostat in the plant's solar field, consequently adapting the flux projected onto the receiver, which impacts the behavior of the heat exchanger modifying the outlet salt temperature. The

salt exiting the receiver is then directly coupled to the power block or fed to the storing tanks and then fed to the power block.

The architecture for the proposed control strategy is presented now that the manipulated and controlled variables have been defined. Figure 31 shows a block diagram for the feedback control strategy. The flux projected onto the receiver and other plant variables serve as inputs into an AFD constraint module in which the AFD is determined. The setpoint for the controlled loop is defined as a gap between the AFD and the incident highest flux, and there is one value for each group of heliostats, Gap_i . This setpoint allows the control engineer to determine a safe distance between the highest incident flux and the allowable flux density. A non-conservative approach would set them all to zero.

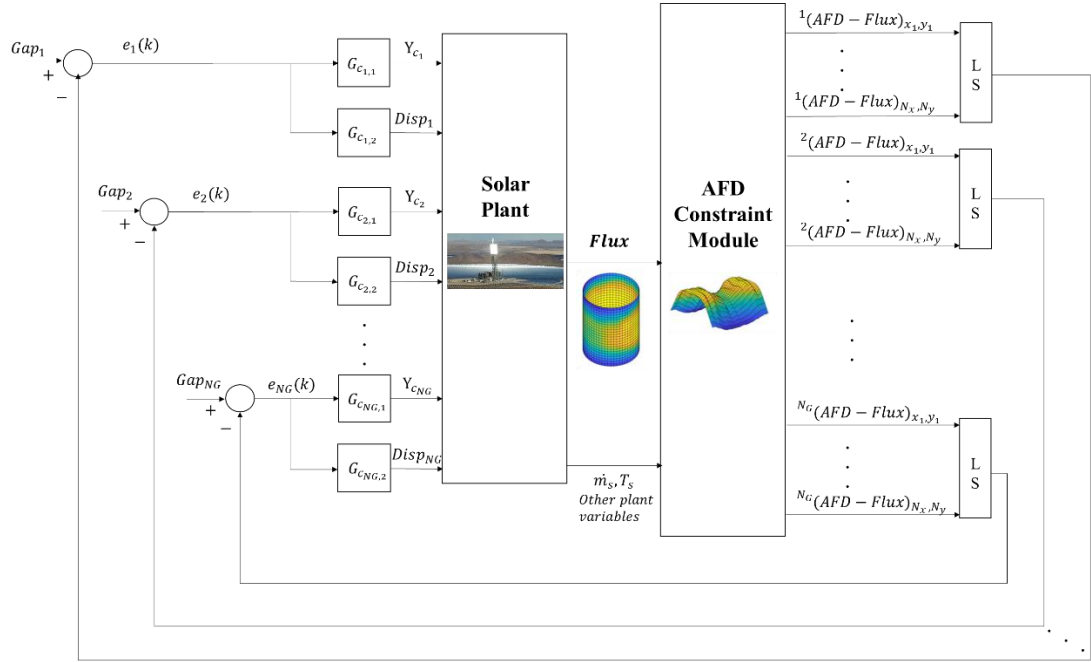


Figure 31. Block diagram of the proposed control strategy, the setpoint is the gap between the allowable flux density and the incident flux on the receiver.

First, for each group of heliostats, there are two controllers. A set of controllers, $G_{C_{*,1}}$, impacts the dispersion of the group of aiming points for heliostats belonging to that

group. An increment in the controller output signal will disperse the aiming points, while a decrement will concentrate them. In contrast, the controller $G_{C*,2}$ acts upon the vertical centroid of the aim points, an increase in the controller output signal will move the aim points' centroid farther from the equator, a decrease in the signal will bring the centroid closer to it.

The controllers used in this dissertation are PI-Controllers, and at each iteration, the input to the controller is the error, $e(k)$, which is equal to the subtraction of the desired setpoint and the minimum difference between the allowable flux distribution and the actual incident flux. This error is calculated for each area of the panel where the group of heliostats is assigned. It is then scaled by setting the error range to be: $[-100,100] \frac{kW}{m^2}$, which means that an error of $100 \frac{kW}{m^2}$ equals 100 % of the transmitter output (%TO): $e(k) = 100 \frac{kW}{m^2} = 100 \%TO$. Values out of this range are saturated at either the lower or the upper bound.

Each controller's output is the parameter that modifies the dispersion and the centroid for the group of heliostats, i.e., the manipulated variables $m(k)$ for the valve analogy. One of these loops can be represented by the simplified block diagram illustrated in Figure 32. In case the strategy could be tested in a real plant, the flux could be indirectly measured or estimated by fusing information from ray-tracing results and sensors located at the receiver

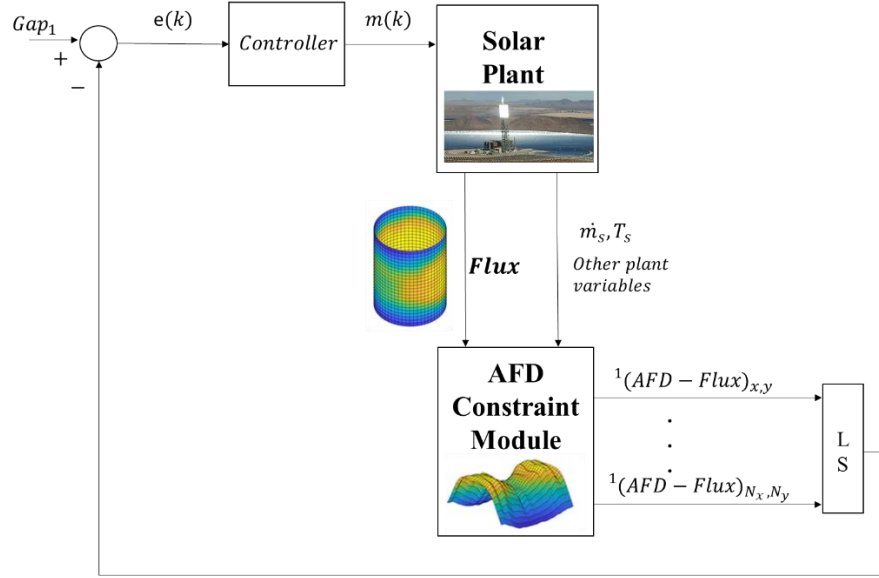


Figure 32. Single Control Loop showing the signals involved in the control strategy for one group of heliostats

A continuous PI-Controller uses the following equation to derive the controller output:

$$\Delta m(t) = K_C e(t) + \frac{K_C}{\tau_I} \int e(t) dt \quad (44)$$

Where K_C is the controller's proportional gain, and τ_I is the integral time. The tuning of this controller is presented in Chapter 4. Sending information to all heliostats on the solar field is a distributed network task that presents its own technical challenges and escapes this dissertation's scope. In this work, the control law was implemented by a discrete approximation of the error's integral between samples. The controller will calculate new positions, not in a continuous fashion but based on a sampling time in a discrete form.

The velocity form for a discrete PI-Controller was selected since it automatically includes anti-reset windup (Marlin, 1995). With the following equation, the values of the control law at each iteration are obtained:

$$m(k) = K_c \left[(e(k) - e(k-1)) + \frac{1}{\tau_I} e(k) \right], \quad (45)$$

where, $m(k)$ is the controller output at iteration k . The controller action based on the error drives both the centroid's dispersion and vertical position for each group of heliostats. As stated above, a positive value for the controller output $m(k)$ increases dispersion or moves the centroid of the group farther away from the panel's equator. A negative value concentrates the aiming points or moves the centroids close to the equator.

Another contribution of this work is to take into account for the contribution of adjacent regions to the incident flux on the panel area assigned to a group of heliostats. This dissertation's novel approach considers the complete set of data points from all the receiver's surface plane. It applies a weighted average of spatially neighboring groups as the error feeding the controller.

For each controller in group- i , the error signal entering the controllers considers the situation of the adjacent region by a weighted average to include into the controller's decision the interaction among control loops. In Figure 33, the flow of information in the control strategy for a zero-valued Gap is presented, including one central group of heliostats, one group to the right, and one to the left.

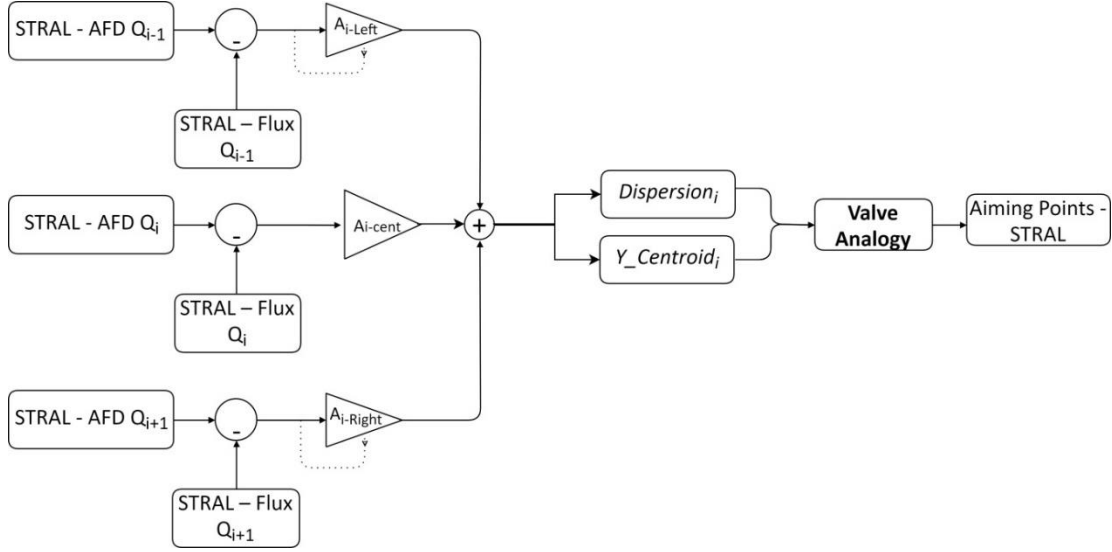


Figure 33. Control Loop for one group of heliostats for a zero valued Gap

The values of the diagram refer to the weighting parameters for the neighboring errors; their default value was set to $A_{right} = A_{left} = 0.3$, and $A_{cent} = \left(1 - \frac{A_{right} + A_{left}}{2}\right) = 0.7$. The arrows below the weighting parameters A_{right} and A_{left} , represent reset feedback signals to the gain. A positive error for the group means that the irradiated flux in the panel area assigned to the group of heliostats is below the allowable flux density. Therefore, the error from adjacent regions is not considered in the controller output calculation so that the group concentrates the flux faster.

Furthermore, as it was explained before, the error entering the central group is defined using the errors from the adjacent areas, as shown in the following equations:

$$e_{center}(k) = \min\{AFD_i - Flux_i\} \quad (46)$$

$$e_{right}(k) = \min\{AFD_{i+1} - Flux_{i+1}\} \quad (47)$$

$$e_{left}(k) = \min\{AFD_{i-1} - Flux_{i-1}\} \quad (48)$$

$$e(k) = \left(1 - \frac{A_{right} + A_{left}}{2}\right) e_{center}(k) + \frac{(A_{right}e_{right}(k) + A_{left}e_{left}(k))}{2} \quad (49)$$

3.2. Solar radiation forecasting

There are several phases involved in a solar energy power generation project. First, the feasibility is evaluated, identifying potential locations and technology based on historically available solar resources and local economic variables. Afterward, a design phase starts where models of system configurations are analyzed throughout the system's life. Consequently, a deployment phase occurs in which the construction, commissioning, and testing of the system are conducted. And finally, the normal operation phase, where the new power system is brought online considering system operators' needs, complying with transmission contracts and guidelines from state regulatory agencies (Stoffel, 2013).

During the feasibility phase, it is necessary to characterize the available solar irradiance during a historical time period, which can be used for energy conversion in the place of interest. This phase is known as Solar-resource assessment, while solar-energy forecasting becomes necessary for the operation of an electrical grid with solar-power generation or a solar power plant's operation.

As seen in chapter 2, solar irradiance is defined as a radiant flux density or power density (W/m^2) and the three fundamental components of solar radiation at the surface are the Direct normal irradiance (DNI), which is the solar beam coming directly from the solar disk on a planar surface normal to the sun and can be measured by a pyrheliometer. The Diffuse horizontal irradiance (DHI), or solar radiation coming from the entire sky on a horizontal surface, excluding the DNI. This radiation has been scattered by aerosols and clouds and can be measured with a shaded pyranometer. The third component is the Global horizontal irradiance (GHI), which is the total hemispheric solar radiation coming down on a horizontal surface and can be measured by an unshaded pyranometer.

As introduced previously, clouds have the strongest effect on the amount and type of solar irradiance available for energy conversion, even though there are also complex interactions between solar radiation and the atmosphere's composition under a cloudless sky. For the forecast of solar radiation, it is necessary to account for the sun and the earth's position, the atmospheric properties, and their effect on available solar energy for the conversion system. The methods designed for this forecast depend on the forecast period. A basic approach estimates an available clear-sky irradiance either from weather databases or sensors used to determine atmospheric content values and then incorporates the effect of the clouds. Some of these measurements can be determined using instruments on the ground or satellite information, or they can also be based on numerical weather prediction.

The timescales in which the forecast is needed are also an important consideration, with horizons starting in seconds or minutes, known as intrahour, intraday, or intraweek. Forecasts used for scheduling use intraweek information, while near-real-time operation benefits from intrahour forecasting or even nowcasting.

In Concentrating solar systems, DNI is the fuel, and its availability should be known. Hence, it should be forecast, also, because of the nonlinear dependence of the system efficiency on DNI and the controllability of power generation with or without thermal storage. However, this component of solar radiation is influenced by phenomena complicated to consider, including cirrus clouds, fires, dust, and air pollution. Moreover, the thermal inertia and thermodynamic nonlinearities associated with CSP present a technical challenge to couple production with DNI at timescales in the minutes' range (Stoffel, 2013).

For long-time horizons, physics-based models are employed. Then, the methods are combined for a shorter time scale, relying on cloud models and using numerical weather prediction software. For the short term, intrahour techniques based on total-sky-imagers have been investigated for both GHI and DNI. They calculate cloud

positions and turn them into deterministic models (Kazantzidis et al., 2017). Also, in short-term forecasting, there are statistical approaches, including classical methods such as autoregressive integrated moving averages (ARIMA) but also artificial neural networks (ANN) (Coimbra & Pedro, 2013).

3.2.1. WobaS nowcasting system

In short time scales and small spatial scales, solar resource forecasting is a task not currently solved by satellite products or numerical weather predictions. Instead, in recent years sky-images, obtained from ground cameras, have begun to be used to deal with the spatial and temporal variability of ground radiation induced by clouds. Thus, becoming tools for nowcasting systems or short-term prediction systems for solar irradiance (Kazantzidis et al., 2017). For four years, the European Union funded a project entitled: Direct Normal Irradiance Nowcasting methods for optimized operation of concentrating solar technologies, DNICast. Within this project's framework, the partners developed state-of-the-art methodologies in which parameters and estimations of solar resources were investigated and applied in real weather conditions. The Institute of Solar research and other industrial partners, including a spinoff of the DLR, CSP Technologies, used the knowledge derived from this broad investigative effort to develop a novel system to predict short-term, spatially resolved maps of ground solar radiation up to 15 minutes. The system is called WobaS, which stands for “*Wolkenkamera-basierte Nowcasting-Systeme*” which is german for the ASI-based Nowcasting system (Pascal Kuhn et al., 2017).

The WobaS system uses the images provided by one or more ASIs and a voxel carving-based cloud modeling method. It consists of deriving three-dimensional objects using multiple camera perspectives combined with a cloud segmentation independent stereoscopic cloud height and tracking detection system. An example of the system's cloud objects and the derived DNI map corresponding to the spatially resolved ground radiation provided by the system is shown in Figure 34. Tracking these 3D-Cloud objects over time allows for the calculation of future cloud positions.

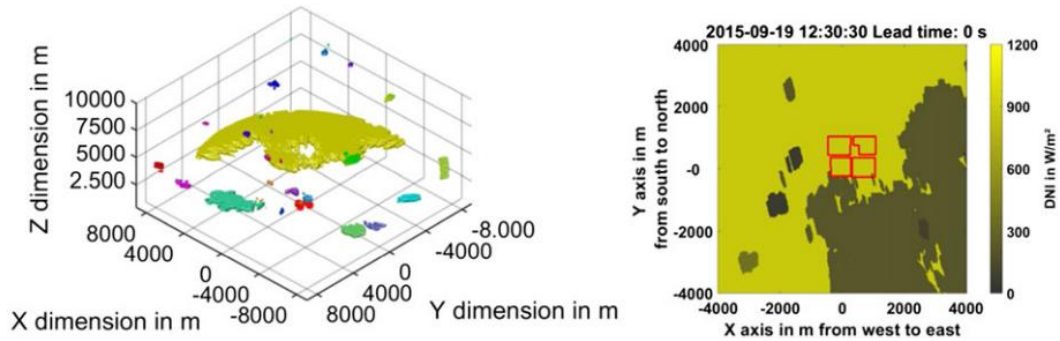


Figure 34. Cloud objects in the voxel space (left) and corresponding nowcasted direct normal irradiance (DNI) map (right) (Pascal Kuhn et al., 2017).

Before the 3-D cloud object has been created, clouds had to be detected and segmented. This is achieved by using a proprietary 4-dimensional clear sky library (CSL). This library stores for every pixel Red-to-Blue Ratio (RBR) value, which depend on:

- 1) Sun pixel angle (SPA)
- 2) Pixel zenith angle (PZA)
- 3) Air mass (related to solar elevation for the site's altitude)
- 4) DNI-derived Linke turbidity. This index is an approximation model for the atmospheric absorption and scattering of solar radiation under the clear sky and is calculated using historical solar radiation measurements.

If the pixel in the ASI images is not inside the library, it is assumed it belongs to a cloud and is considered in the voxel carving procedure described. The system's cloud height and tracking accuracy are discussed in (B. Nouri et al., 2019), while the uncertainty derived from the technique is discussed in detail in (Bijan Nouri et al., 2019). One conclusion is that the performance of the ASI-Nowcasting system is highly related to the prevailing weather conditions.

After a research stay in the Institute of Solar Research at the DLR, a license agreement between the Institute and the Universidad del Norte was completed. Data from the WobaS system for the Experimental site at the Plataforma Solar de Almería (PSA) on

the day 14.05.2016 was provided for this research. That day contains both clear sky, as well as varying periods of DNI. The DNI for that day, as measured by a pyrliometer, is shown in Figure 35.

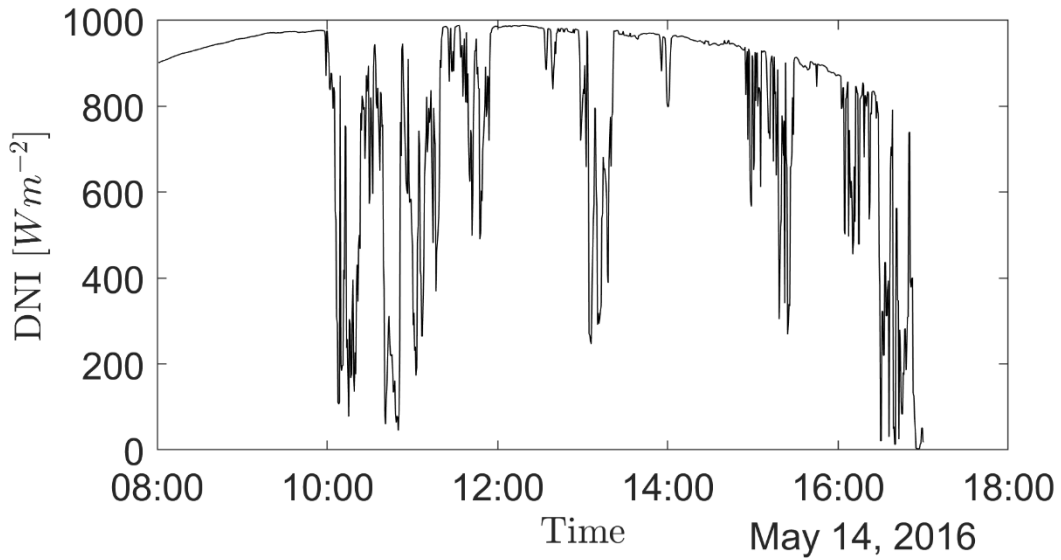


Figure 35. Measured DNI for the dataset

The dataset consists of several ground irradiances maps for an area of 8 *Km* by 8 *Km* and a resolution of 20 *m*. Every 30 seconds, the system produces the spatially resolved map for the current DNI and a forecast for the next minute, up to 15 minutes ahead. Additionally, it provides two maps every minute, considering the uncertainty and a spatial filter to account for rapid changes in boundary areas. A sample spatially resolved radiation map for a lead time of zero, i.e., the forecast is in space, not time, is shown in Figure 36.

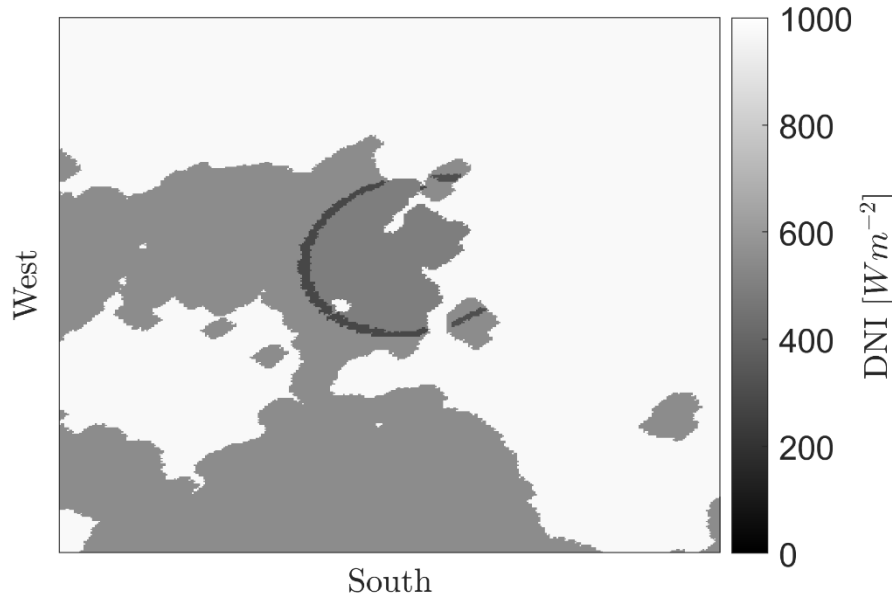


Figure 36. Sample radiation map from WobaS for 11:05:00 on May 14th, 2016, leadtime=0.

The dark ring in the middle of the map corresponds to a correction implemented to account that the transmittance of the clouds is measured with a pyrliometer with an opening angle of 5° . The cloud elements in the volume space covered by this 5° cone are always considered separately and receive the current transmittance measured value. For areas outside this 5° cone, clouds receive a transmittance value using a statistical method, in which the current and historical cloud heights and transmittance measurements are taken into consideration.

3.2.2. Disturbance resampling

Since the data is available every 30 seconds, and to study a closed-loop system's behavior, a higher sampling rate is needed. A method was implemented to decrease the sampling rate and obtain transition radiation maps every 5 seconds, based on the spatially resolved maps with no lead time.

To do so, we considered each data point in the map as a time-dependent function. For this function, values in between samples were linearly interpolated to create new radiation values. For example, the point in the center of the map starting at 12:21:00 p.m. for 300 seconds had the DNI values shown in Figure 37, along with the interpolated values.

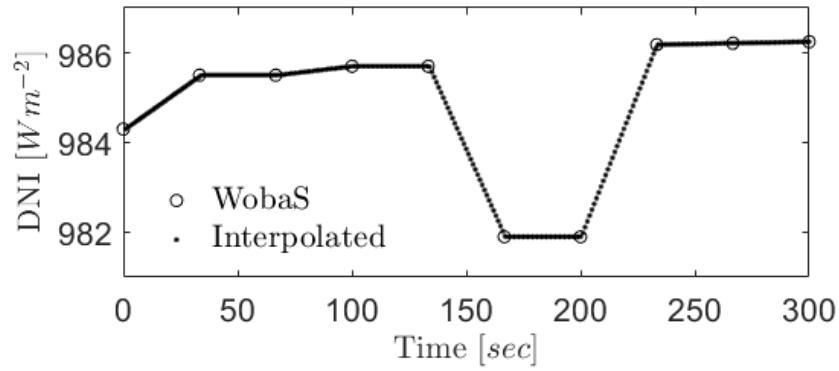


Figure 37. WobaS datapoint in the center of the map, and interpolated values for 300 seconds

The same procedure is applied for each data point of interest in the radiation map. Thus, obtaining radiation maps for every 5 seconds. Figure 38 shows the WobaS radiation maps for 12:25:30 p.m. and 12:26:00 p.m., and in Figure 39, the interpolated 5-sec maps obtained with the proposed resampling technique are shown.

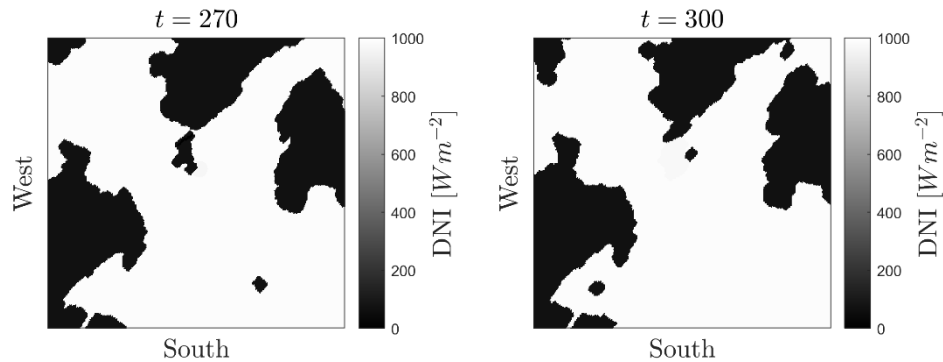


Figure 38. WobaS Radiation maps for 12:25:30 p.m. ($t = 270$ s) and 12:26:00 p.m. ($t = 300$ s) .

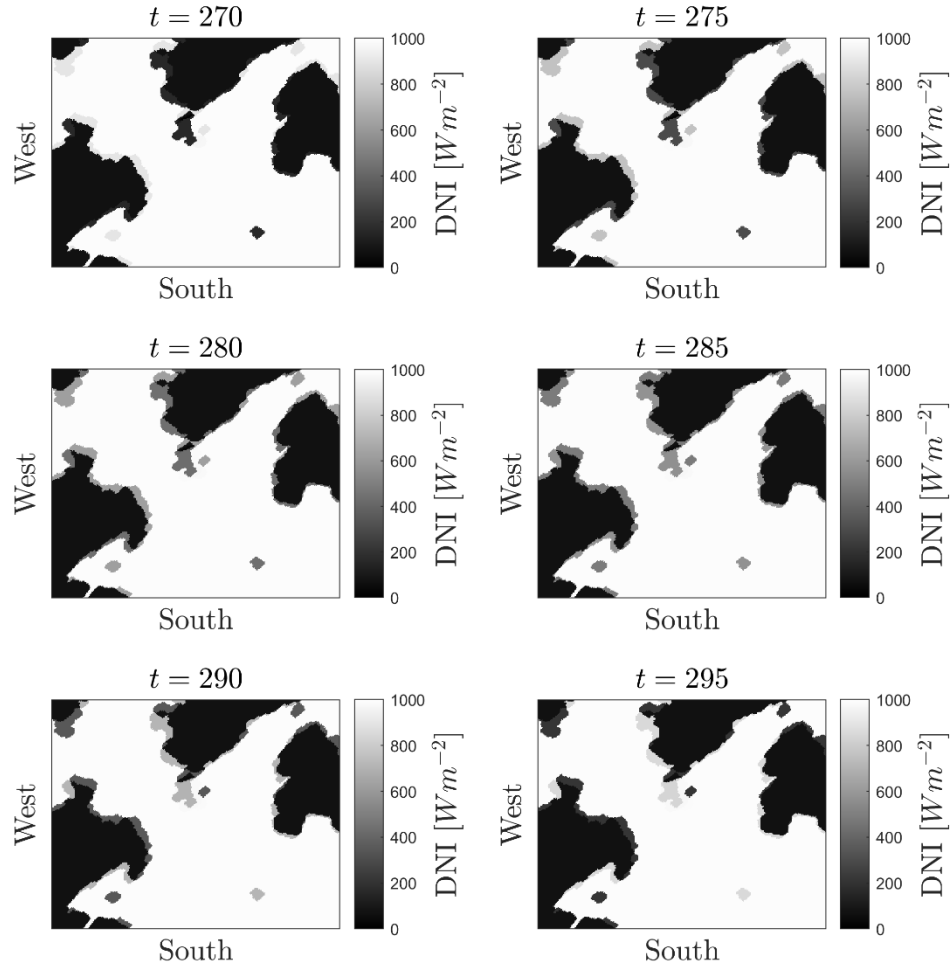


Figure 39. Interpolated Radiation maps between 12:25:30 p.m. (t=270 s) and 12:26:00 p.m. (t=300 s) , every 5 seconds.

This resampling method was developed to use the spatially distributed solar radiation information from the WobaS system without temporal forecast as an input to analyze the behavior of the control strategy when atmospheric disturbances enter a solar field.

3.3. Design of an adaptive control strategy using nowcasting information

3.3.1. Concept

In this work, we propose an adaptive control strategy using a feedforward architecture in which nowcasting information from the disturbance is used. In Figure 26, both feedback and the adaptive strategy with feedforward architecture are illustrated. Here the disturbance $D(s)$ affects the controlled variable via the transfer function $G_D(s)$.

The information from the nowcasting system, which is related to the disturbance, is used by the controller $G_{FF}(s)$ to determine a controller action $M_{FF}(s)$ which is added to the controller action of the feedback loop.

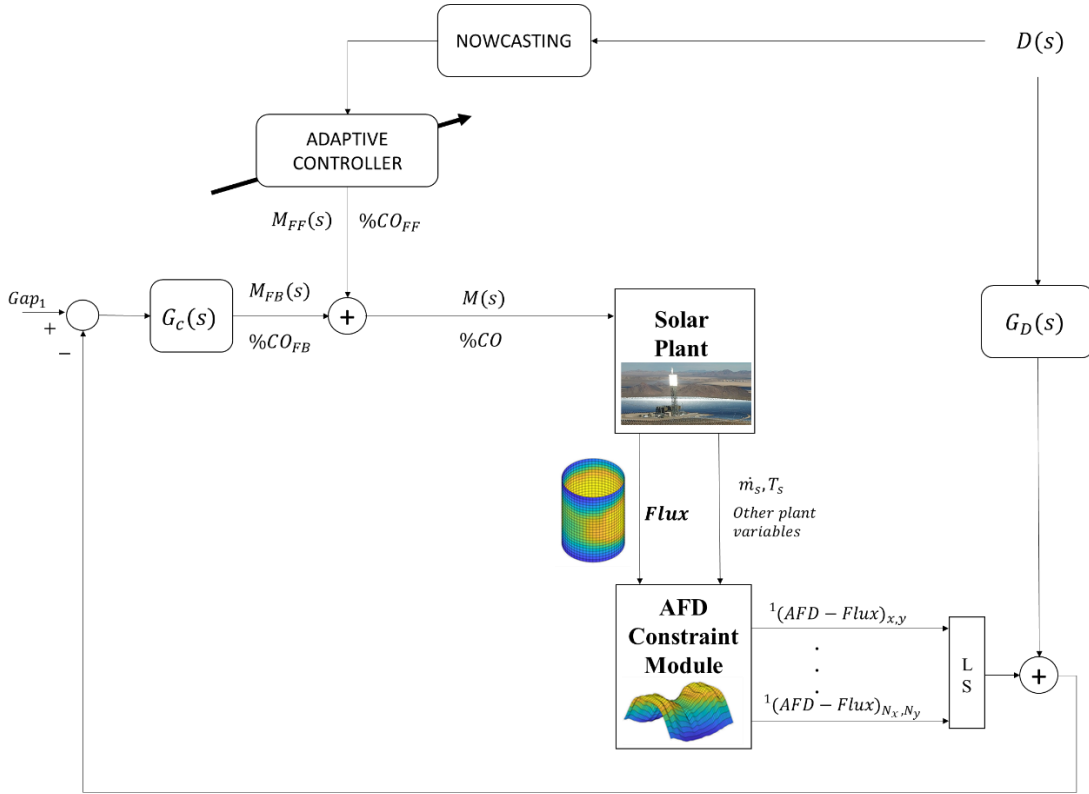


Figure 40. Block diagram for a closed-loop feedback control strategy with adaptive feedforward compensation

3.3.2. Implementation

The nowcasting information provides every 30 seconds a set of 16 irradiance maps on the surface. One map containing the spatially resolved irradiance information for the

current time, then 15 maps with the temporally and spatially resolved prediction for each minute up to 15 minutes ahead of the current time.

An index was developed to convey this information to the controller in charge of each group's dispersion. The coordinates from each heliostat in the group determine if that point in the nowcasting map is shaded or not. For which a threshold for the irradiance was set to $500 \frac{W}{m^2}$. Then, a heliostat fraction index (Hel_{f_i}) is proposed for each group. Inspired by the variability index presented by Nouri et al. (B. Nouri et al., 2020), the heliostat fraction for a group is defined in this work as the number of shaded heliostats in a group divided by the number of heliostats in that group.

$$Hel_{f_x} = 100 \frac{\sum hel_{shaded_i}}{\sum hel_{group_i}} \quad (50)$$

Now, the rule to adapt the dispersion controller output for each group of heliostats is defined using the following logic:

$$M_{FF}(k) = \begin{cases} k_{FF}, & Hel_{f_x}|_k > 50 \wedge Hel_{f_x}|_{k+1} < 30 \\ 0, & other\ cases \end{cases}$$

In this way, if more than half of the heliostats in a group are covered at instant k , according to the nowcasting spatially resolved information, but one minute later, less than 30 % of the heliostats in the group are shaded, the adaptive controller will increase the controller output by k_{FF} . A more detailed description of the implementation is presented in the following chapter.

3.4. Design of a measuring system in Barranquilla as a starting point towards the prediction of short-term solar radiation

There is no public information on ground measurements of DNI in Colombia. Accurate long-lasting records of the direct irradiance are necessary for the pre-feasibility studies of any high-temperature CSP technology. This lack of information drove us to make an enormous budgetary effort, considering the resources available for this

investigation, and invest all the funds of this research to acquire a solar tracker and two solar radiation sensors. The tracker has a solar elevation angle's accuracy of fewer than 0.01° between 0° and 87° with a resolution of 0.009° . The characteristics of the sensors are as follow:

Pyranometer: Class A according to the norm ISO 9060:2018 (ISO, 1990) of quality secondary standard, and a response time under 0.5 s, the irradiance range goes up to 4000 W/m² in wavelengths between 285 and 3000 nm.

Pyrheliometer: Class A with a response time under 0.2 s, the irradiance range goes up to 4000 W/m² in wavelengths between 200 and 4000 nm.

An essential connection between the sensors, the tracker, and a computer serving as an interface for the digital storage system was possible with the UREMA group's help, which provided a CompactRio unit for this measuring system. The CompactRio contains a controller with a processor and a user-programmable field-programmable gate array (FPGA), which can hold one or more conditioned Input/Output modules. For the solar radiation measurement system, two modules are used. The NI-9207 module is a Voltage and Current Input Module, which reads the signals from the sensors. And the NI-9263, a Voltage Output Module, is used to feed the temperature sensors located in the pyrliometer and pyranometer and activate a window heater that prevents abnormal measures due to condensation in the pyrliometer quartz window. The basic configuration can be seen in Figure 41.



Figure 41. Diagram of the basic configuration for the solar radiation measurement system.

This complete connection architecture is more complex, and a more detailed functional diagram of the necessary software tools is shown in Figure 42. Here the numbers 1 to 3 refer to different hardware instances where the functional software must be embedded. In the CompactRio, both the pyrhelimeter and the pyranometer are read every 30 seconds, and those values are averaged to provide one value per minute, respectively. Every hour an FTP client uploads to a secure FTP server, hence number 2. The server belongs to the University's information architecture. Finally, in a separate machine or in the server itself, a service is started every 2 hours to upload the cloud's gathered data.

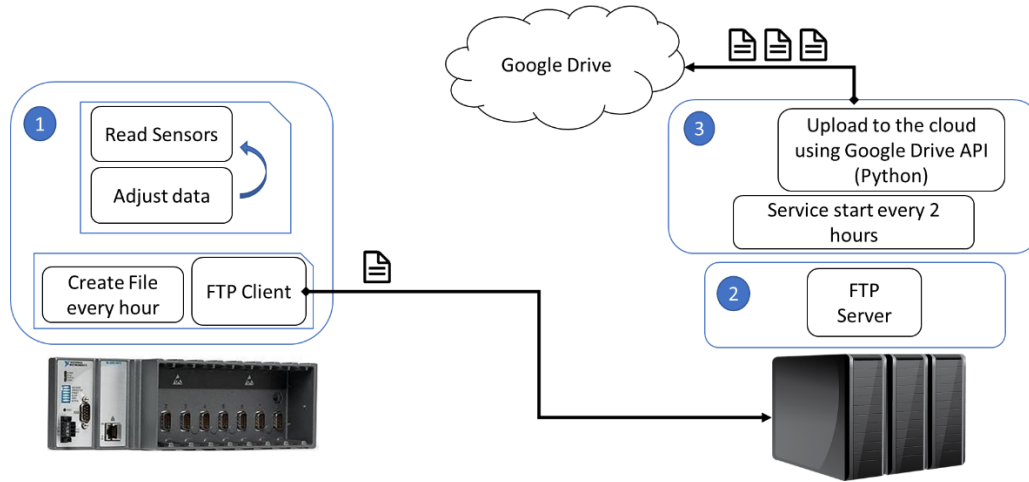


Figure 42. Functional diagram of the measurement system.

The control panel, which enables the connection between the tracker/sensors and the CompactRio, also enables the CompactRio to access the local area network (LAN) and voltage source shown in Figure 43. Besides this software and hardware design, the mechanical requirements for the structure necessary to install the tracker and the control panel have also been delivered to the University, awaiting for the necessary conditions to install the system resurface.

As the measurements become available, the data quality must be assessed, which opens research opportunities early on with the data acquisition. Furthermore, once the data is validated, the DNI time-series can be modeled using a model structure such as the Autoregressive Integrated Moving Average (ARIMA). The forecast can start to be developed locally. Additionally, this data might prove of interest for other research groups at the university, dealing with climate models that can be adjusted by having ground solar fluxes measurements. Another contribution from this dissertation is laying the groundwork for that research line at the UREMA group.

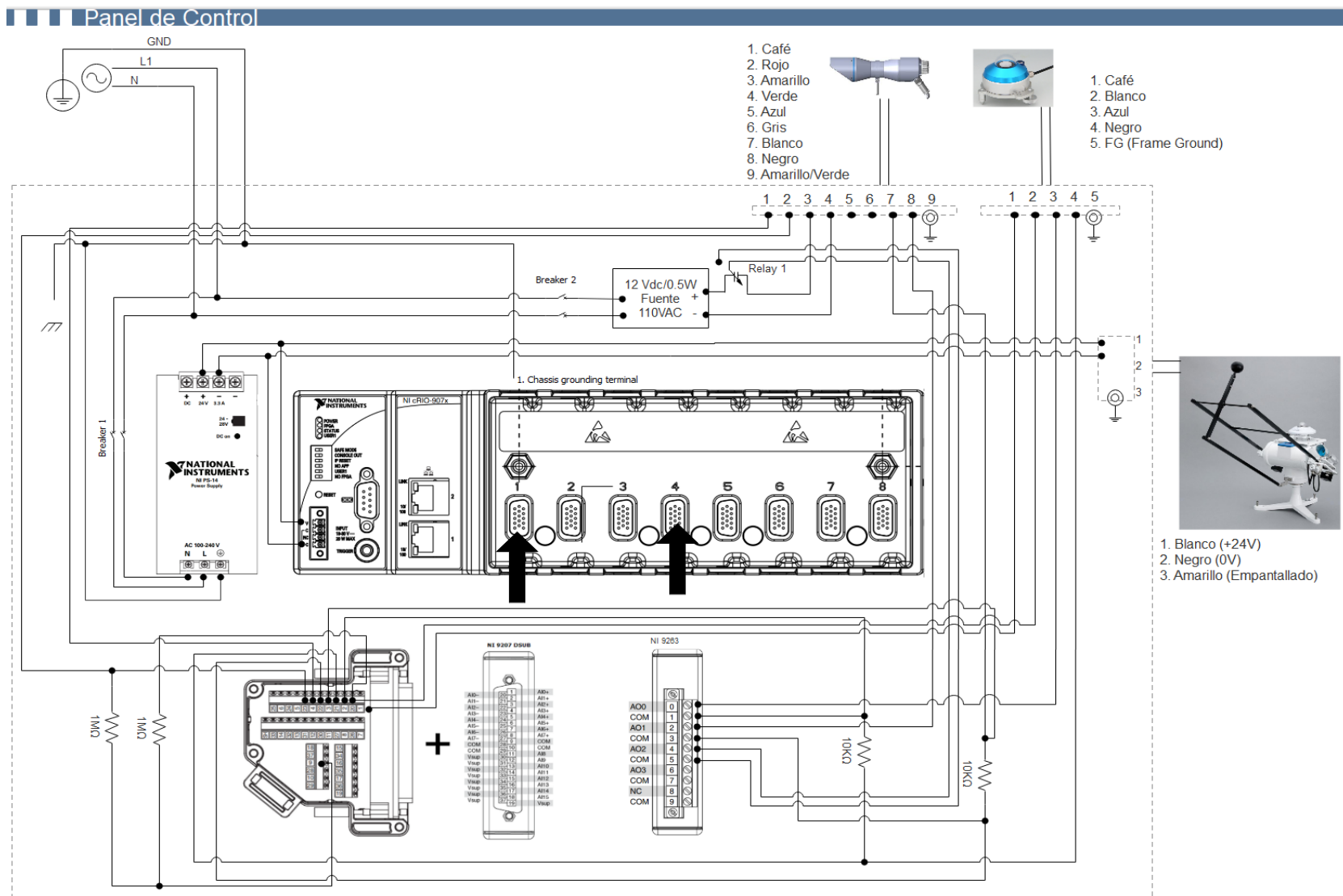


Figure 43. Control panel for the solar radiation measuring system.

4. RESULTS

This chapter presents the main findings encountered during this investigation. In the first section, a reference power plant is presented, which has served as the platform to explore the design control strategies. The 3D steady-state model and its numerical implementation are discussed. This model was used to obtain key process variables to test the proposed control strategies. Also, a brief introduction to a dynamic model is presented.

The following sections discuss the main results obtained during this investigation. First, an evaluation of the feedback strategy begins with one novel application of the strategy. The proposed feedback controller is used to obtain near-optimal aiming points at a given operating point using a simulated environment. The method proposed to tune the parameters of the proposed feedback strategy is discussed next, followed by the analysis of the disturbance rejection behavior of the feedback solar field control strategy under atmospheric disturbance. For which data collected from a real nowcasting system is used. Subsequently, it is explained the concept developed to incorporate into an adaptive controller the prediction information for the solar radiation available from a state-of-the-art nowcasting system. This section then discusses the influence of some key parameters from the proposed control strategies on the closed-loop system's behavior.

In the next section, the adaptive strategy is compared to an industry-standard practice. A method is also presented to calculate the thermoelastic stresses in the tubes using the steady-state model's temperature distribution. The stress cycles induced by atmospheric disturbances are discussed in terms of the mechanical integrity of the receiver. This methodology's limits are discussed, thus proposing new lines of research, particularly the need to find dynamic allowable flux density limits.

4.1. Reference Power Plant

The so-called virtual plant's solar field layout and receiver were designed for an approximate thermal power of 450 MW, using 6482 heliostats (Flesch et al., 2017). The receiver consists of 12 panels, each with 117 tubes. There are two independent flow paths for the molten salt, with a crossover after the third panel, as shown in Figure 44.

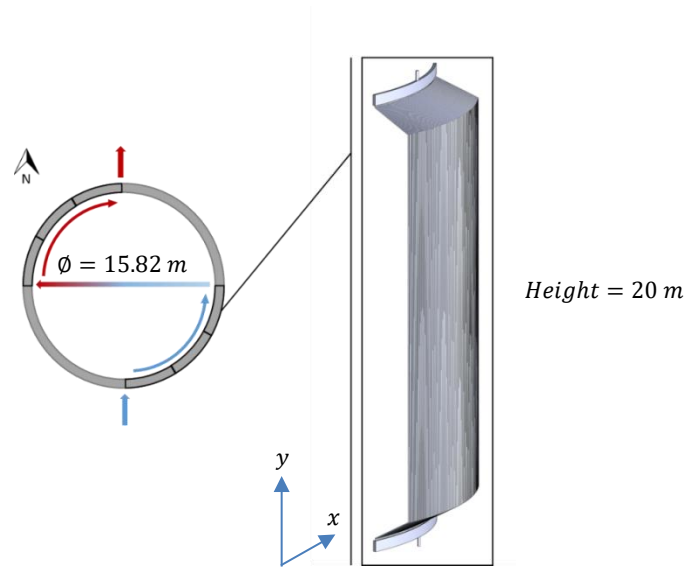


Figure 44. Schematic drawing for a panel of the receiver and one flow path for the molten salt.

The main characteristics of the reference power plant are summarized in Table 2. Furthermore, in Figure 45, the position of each heliostat in the solar field is presented. Additionally, each heliostat's optical efficiency is plotted for the autumnal equinox with all heliostats aiming at the receiver's equator. The optical efficiency is calculated as the dot product of the incident beam ray direction and the normal of the mirror surface.

Table 2. Summary of heliostat and receiver design parameters (Flesch et al., 2017).

Heliostats	
Total reflective area	121 m ²
Width	12.93 m

Height	9.57 m
Surface error	1.3 mrad
Tracking error	0.65 mrad
Total reflectivity	90.24 %

Receiver

Optical Tower height	190 m
Diameter	15.82 m
Radiated height	20 m
Flow paths	2, crossing after the third panel
Panels	12
Tubes per panel	117
Tube inner/outer diameter	30 / 35 mm
Inlet / Outlet Temperature	290 / 565 °C

For the solar field, this results in a total intercept factor of 0.983. This value means that the total power intercepted by the receiver is ~98% of the reflected radiation of all heliostats in the solar field, which was not blocked by neighboring heliostats, accounting for the attenuation caused by atmospheric transmission.

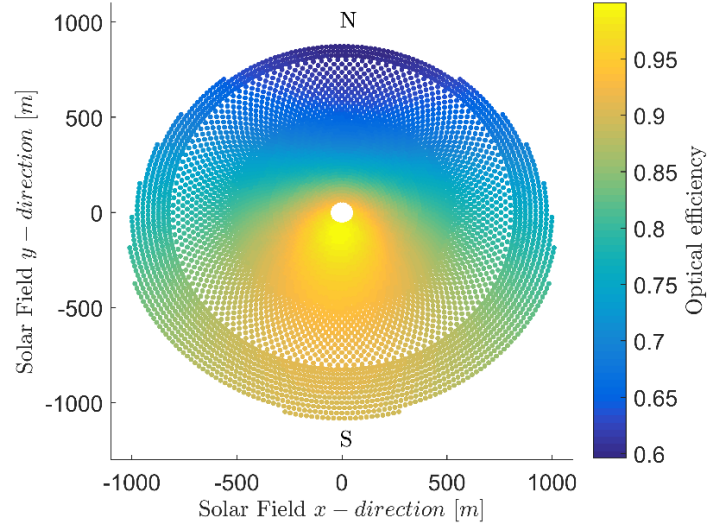


Figure 45. Optical efficiency of the solar field with all heliostat aiming at the receiver's equator at noon on March 21st

4.1.1. Steady-State Model

The temperature distribution over the tubes is obtained from the 3D steady-state model composed of equations (51) and (52):

$$k_w \left[\frac{1}{r} \frac{\partial}{\partial r} \left(r \frac{\partial T_w}{\partial r} \right) + \frac{1}{r^2} \frac{\partial^2 T_w}{\partial \theta^2} + \frac{\partial^2 T_w}{\partial z^2} \right] = 0 \quad (51)$$

Where k_w represents the thermal diffusivity of the pipe material, and r , θ , and z are the radial, tangential and axial directions. And for the fluid:

$$Q_{\text{fluid}} = \dot{m} C_{p_f} \frac{\partial T_f}{\partial z} \quad (52)$$

And \dot{m} is the mass flow of the molten salt, C_{p_f} is its specific heat capacity.

The model is solved using a compact finite difference scheme (Lele, 1992) (Han & Dai, 2013), which approximates each differential operator by a numerical matrix. The numerical method is implemented in MATLAB. The necessary boundary conditions

stem from chapter 2, considering that the convection at the inner side of the pipe is equal to the conduction at that surface:

$$-k \frac{\partial T_w}{\partial r} \Big|_{r=r_{inner}} = h_f (T_w - T_{fluid}) \quad (53)$$

And that at the outside of the pipe, the incident power results from the subtraction of the reflected, the radiated, and the power loss due to convection:

$$-k \frac{\partial T_w}{\partial r} \Big|_{r=r_{outer}} = (1 - \rho) Q_{inc} - Q_{rad} - Q_{conv} \quad (54)$$

The backside of the outer pipe wall is assumed to be adiabatic. The reference model in Flesch (Flesch et al., 2017) was used for validation. Figure 46 shows the crown salt temperature at the inner wall calculated by the reference and the 3D-model for one flow path. An inhomogeneous flux distribution on the receiver obtained by STRAL and a mass flow of 8.97 kg/s yields an outlet salt's temperature of $431 \text{ }^\circ\text{C}$ for the model. Using this temperature for the reference model results in a mass flow of 8.95 kg/s , a deviation of just $0.1 \text{ } \%$.

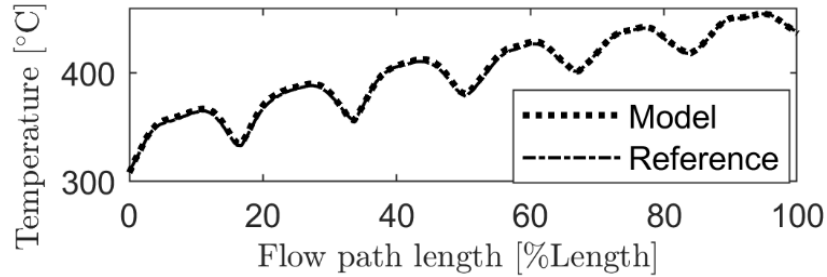


Figure 46. The crown temperature at the inner wall for the steady-state reference model and the model

4.1.2. Dynamic Model

The temperature distribution over the tubes is obtained from the 3D model, which considers the transient change in temperature in the tube's wall and composed of equations (55) and (56):

$$\rho_w C_{p_w} \frac{\partial T_w}{\partial t} = k_w \left[\frac{1}{r} \frac{\partial}{\partial r} \left(r \frac{\partial T_w}{\partial r} \right) + \frac{1}{r^2} \frac{\partial^2 T_w}{\partial \theta^2} + \frac{\partial^2 T_w}{\partial z^2} \right], \quad (55)$$

Where ρ_w is the pipe's density and C_{p_w} is its specific heat capacity. And for the fluid:

$$\rho_f C_{p_f} \left(\frac{\partial T_f}{\partial t} + V_z \frac{\partial T_f}{\partial z} \right) = A_i h_f (T_w - T_{fluid}), \quad (56)$$

Where, V_z is the fluid's velocity and A_i is the finite difference element's area. The boundary conditions are the same as for the steady-state model. The numerical implementation can be completed using a compact Alternating Direction Implicit (ADI) method implemented in MATLAB (Chean et al., 2019; Moin, 2010). This modeling approach was not further pursued during this work. Instead, the steady-state model was used.

4.2. Evaluation of the feedback strategy

In this section, the evaluation of the feedback strategy is conducted on a simulated reference power plant. Initially, one of the main results from this research is discussed, which is that the developed feedback strategy can be used to obtain near-optimal aiming points for an operating setpoint in a simulation environment. First, the equations used in this reference case to define a safe region of operation are introduced to approach this contribution of the dissertation. Then, it is explained how heliostats are grouped based on geometrical considerations. Finally, we present this strategy's use to find near-optimal aiming points configuration at an operation point. Following this, a tuning method is proposed to obtain the parameters to the set of controllers. The disturbance rejection behavior of the plant with the tuned feedback controllers is then analyzed.

For the Solar Two project, the receiver was designed assuming it would undergo 10,000 deep temperature cycles due to the daily operation of draining it and around 30,000 shallow cycles caused by cloud transients. Using these assumptions, the design team chose 316 SS tubes with an outer diameter of 21-mm and wall thickness of 1.25-mm. The receiver consisted of 24 panels and a crossover between east and west. A safe allowable flux density was then calculated and fitted to the salt temperature; moreover, a correction using the Reynolds number allowed for the comparison between the salt's local velocity and the velocity at the design point of operation. After also considering that the salt becomes corrosive at high temperatures, the following two equations were proposed to determine the safe region of operation for the receiver depending both in salt's temperature and velocity; these are given by the following equations, with the temperature is expressed in $^{\circ}F$ (Vant-hull, 2002):

$$AFD < (842.27 - 1.5514 T_{bs} + 4.617 \times 10^{-3} T_{bs}^2 - 3.2073 \times 10^{-6} T_{bs}^3) \left(0.3 + 0.7 \frac{v_s}{v_{dp}} \right), \quad (57)$$

$$AFD < 4.5366 (1103 - T_{bs}) \left(\frac{v_s}{v_{dp}} \right)^{0.8}. \quad (58)$$

Therefore, for every point in the fluid path, the bulk salt temperature of the molten salt T_{bs} , and the allowable flux density AFD can be calculated using the velocity of the salt in the tube v_s , and the velocity for the design point v_{dp} . In this dissertation, these equations define the safe region of operation for the receiver.

Grouping the heliostats

Using the previously described swarm behavior, in section 3.1.2, the number of manipulated variables is reduced. Nonetheless, it is necessary to determine the size of each group. In this work, the division of heliostats into groups in the solar field is made according to geometric considerations. The simulated reference power plant's solar

field is divided into the same number of slices as there are panels in the receiver. In this case, 12 slices, each with eight groups. For a total of 96 groups.

Depending on the heliostats' distance to the central tower, there are two sets of groups for each panel. One set contains heliostats located farther than a radius of 700 m from the central tower, and another set includes the heliostats closer than this threshold. Furthermore, each one of these sets contains four groups of heliostats. As shown in Figure 47, there are two sets of groups of heliostats, and the membership of each heliostat to a group is selected sequentially within the set, as is further shown in Figure 48.

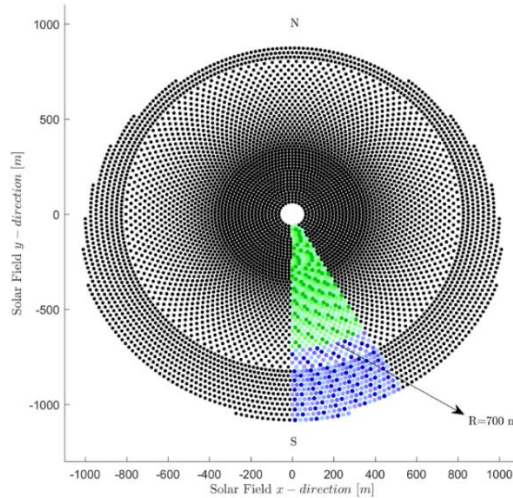


Figure 47. Heliostat distribution and Sets assigned to a panel of the receiver. Green are the four sets of groups of heliostats closer than 700 m to the tower, and blue are the four sets of groups of heliostats farther than 700 m.

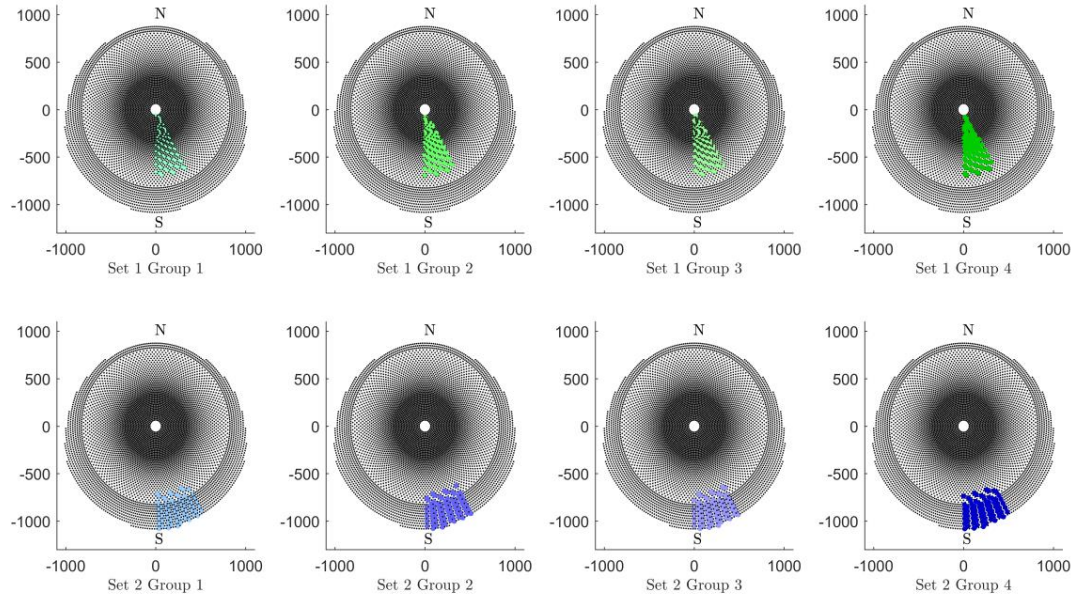


Figure 48. Sets, and Groups assigned to one panel of the receiver.

Figure 49 shows the allowable centroid movement for each group over the panel, given that a panel contains eight groups of aiming points. Four of those groups move from the receiver's equator towards the upper edge of the receiver. Two are located on the right side of a vertical line in the panel center within this group. Two are on the left. The distance (d) from Figure 29 separates vertically the groups' centroids to the right and left of each panel, for example, groups S_1G_1 and S_1G_3 . In this work that distance was fixed to $d = 2m$, which is the center of the area assigned to each group, which forces the centroids to follow a path in the middle of the region assigned to it. The remaining four groups move from the equator towards the receiver's lower edge and follow the same rules as described for the upper part.

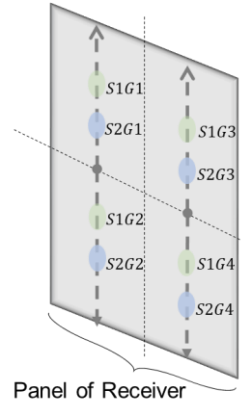


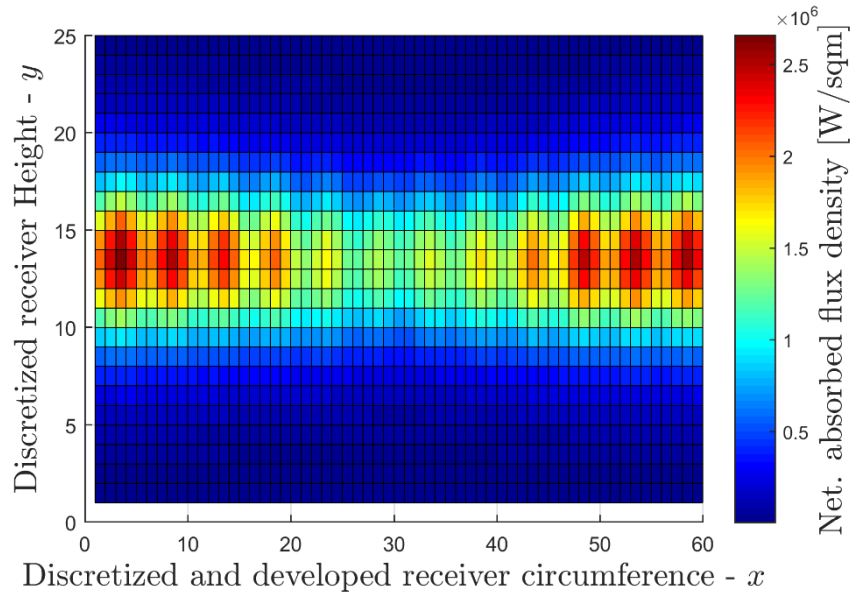
Figure 49. A panel of the receiver and groups assigned to its surface. Groups of heliostats with a slant range higher than 700 m are colored green, blue are those with a slant range under 700 m

During the international internship at the Institute of Solar Research at the DLR, the feedback control strategy was measured against the optimization technique developed by Belhomme (Boris Belhomme et al., 2014) and applied to a virtual reference power plant (Flesch et al., 2017). The open-loop optimization approach of the DLR is based on an ant colony optimization technique. Its implementation is integrated into a steady-state thermal model to determine aiming points that maximize the receiver's thermal output.

The universal algorithm from Belhomme improved with a local search algorithm by Maldonado et al. (Maldonado, Flesch, Reinholz, & Schwarzbözl, 2018) needs to find all the discretized search space, whose size is given by all the number of possible aiming positions to the power of the number of heliostats. This whole dataset is then used to carry out the ant-colony optimization. For the reference power plant with 6482 heliostats, the search space would contain 25^{6482} flux maps if every heliostat could move to 25 different discrete positions. For a given solar hour, atmospheric condition, and mass flow, the optimization takes more than 1.5 hours in a workstation computer with two Intel Xeon E5-2687W processors running at 3.1 GHz and using 30 parallel threads. The same reference power plant is used in this work to present our findings. If

the optimization starts from a randomized position, the thermal power obtained as reported by Maldonado is 455 MW_{th} .

The proposed flux-feedback strategy was modified so that time remained static, i.e., the sun does not move from the design point at solar noon of the autumnal equinox, March 21st. The starting point for the simulation was set so that all aiming points would be concentrated at a point near the receiver's equator. This configuration for the aiming points results in the flux distribution shown in Figure 50a. In contrast, after the controller has stabilized, the flux distribution is shown in Figure 50b.



a)

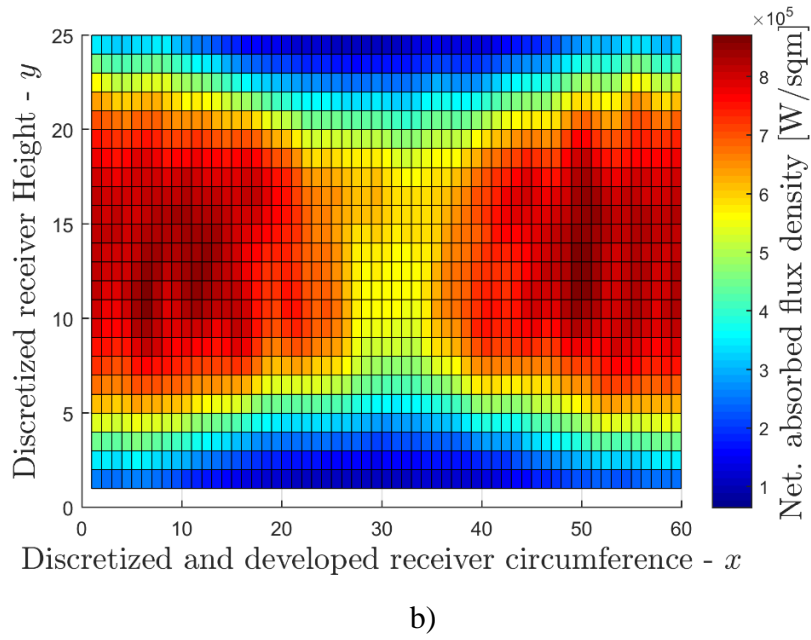


Figure 50. Incident flux on the receiver a) before and b) after convergence of the proposed controller

The control strategy results show that the controller stabilizes fast at a near-optimal solution, as shown in Figure 51. After 60 Iterations, which took 51 *min* with an Intel-Corei7-920, 6 GB RAM desktop computer, the strategy converged to a satisfactory solution for the virtual reference power plant. Even though some points in the panel's surface have higher incident flux than the AFD, those errors are within a 5 % band for all the controllers

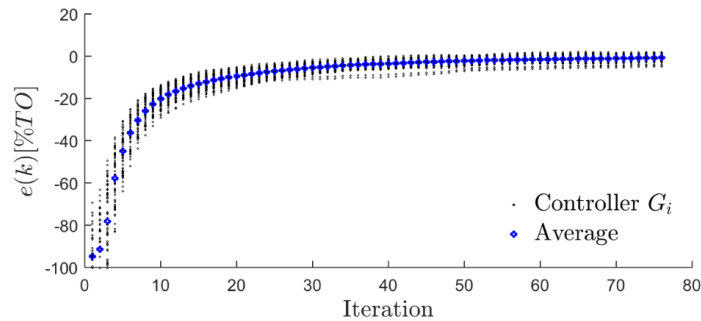


Figure 51. The convergence of the error signals driving the 192 PI-Controllers to a steady-state value.

The computation time for the first 60 iterations is 52 s on average, from which 43 s correspond to the calculations from STRAL, as shown in Figure 52. The controller's output signal and future movements for each heliostat are calculated only in 9 s, making this strategy suitable for real-time implementation during transient conditions. The strategy achieved a thermal power of 441 MW, which is approximately 97% of the optimal value, 455 MW.

The calculation time can be further reduced by improving the MATLAB code. Considering that the controller will be used in a dynamic setting from an already converged solution in a stable point of operation, less than 60 iterations would be required to adapt the aiming point configuration since the algorithm must only react to changes in the flux induced by disturbances.

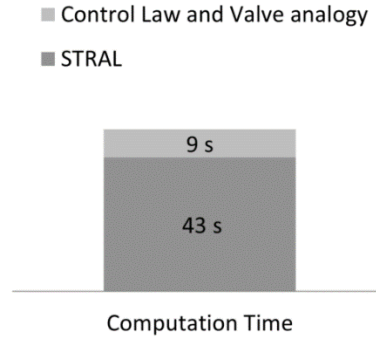


Figure 52. Average computation time for 60 iterations.

Additionally, Figure 53 shows each iteration the standard deviation of the incident flux on the receiver's surface, as calculated by equation (61). $Flux_{ij}(k)$ is the incident flux at grid point (i, j) , $\overline{Flux_{ij}}(k)$ is the mean value for the entire surface's flux density at iteration k . It is clear how the flux becomes more homogeneous as the strategy converges to a solution.

$$\delta_{mean}(k) = \sqrt{\frac{\sum_{i=1}^{25} \sum_{j=1}^{60} Flux_{ij}(k) - \overline{Flux_{ij}}(k)}{25 \times 60}} \quad (59)$$

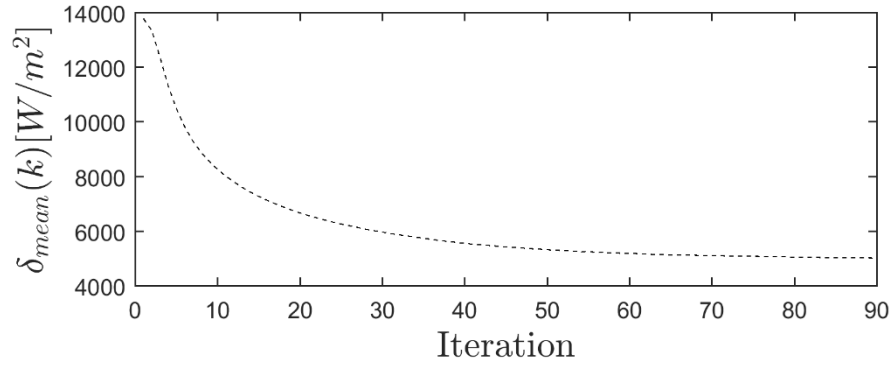
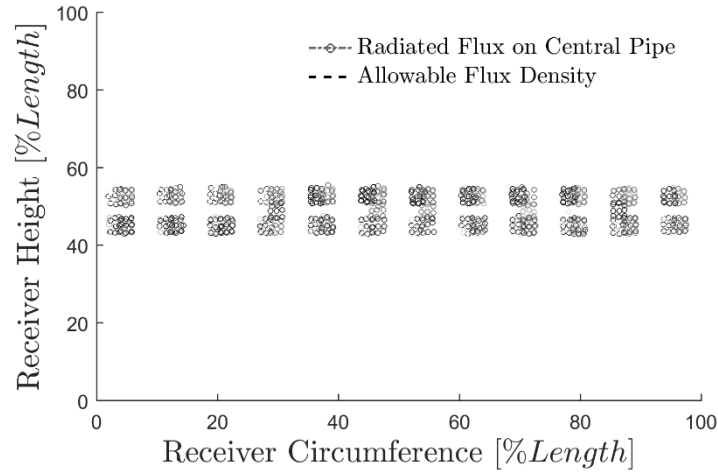


Figure 53. Evolution of the standard deviation as a measure of the homogeneity of the incident flux on the receiver's surface

The initial aiming points and the resulting aiming points when the strategy stabilizes are shown in Figure 54. The receiver is developed radially starting on the south. The aiming points are dispersed at the panels facing south, where the salt enters at the lowest temperature, and the solar field has higher optical efficiency. As the temperature for the molten salt in the tubes closer to the outlet is close to its limiting value, some of the aiming points in the panels facing north are dispersed to cope with the flux limit.



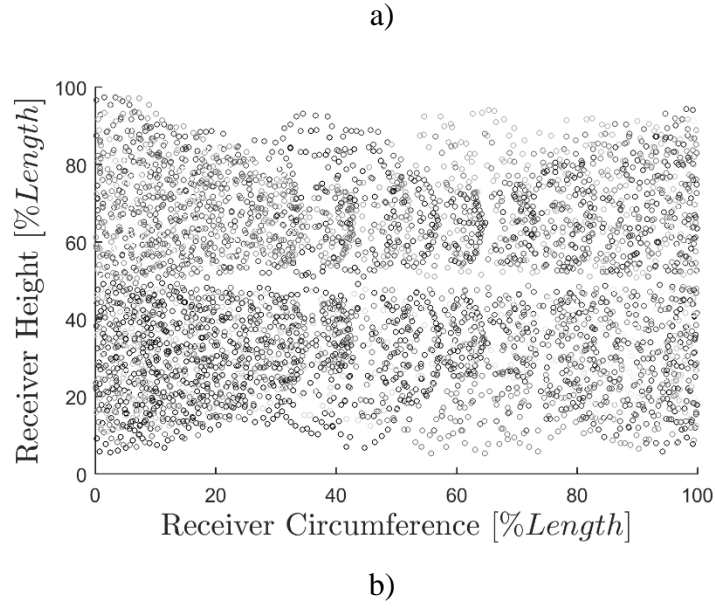


Figure 54. Aiming point distribution on the receiver surface. The receiver circumference begins at the South facing panel and increases anticlockwise. a) Initial conditions for the configuration of the aiming points, b) Aiming points after the controller reached a steady state.

The resulting optical efficiency of the solar field, after the controller has stabilized, is shown in Figure 55. This configuration results in an intercept factor of 0.938.

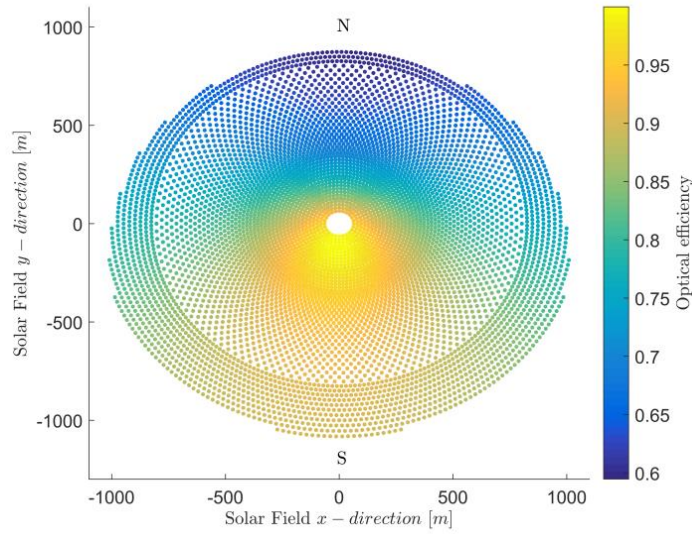
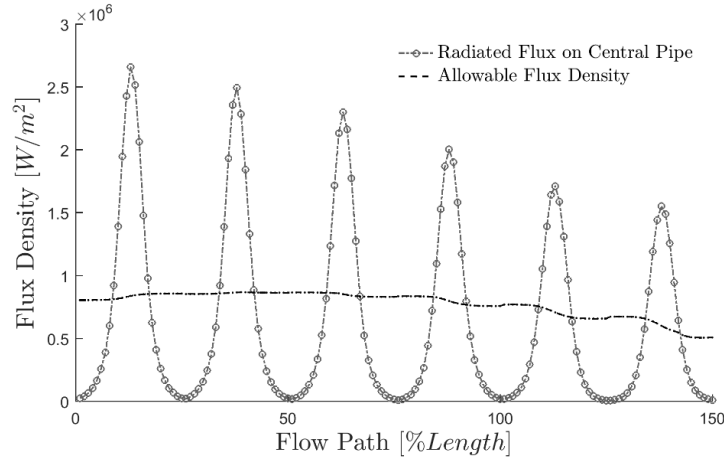
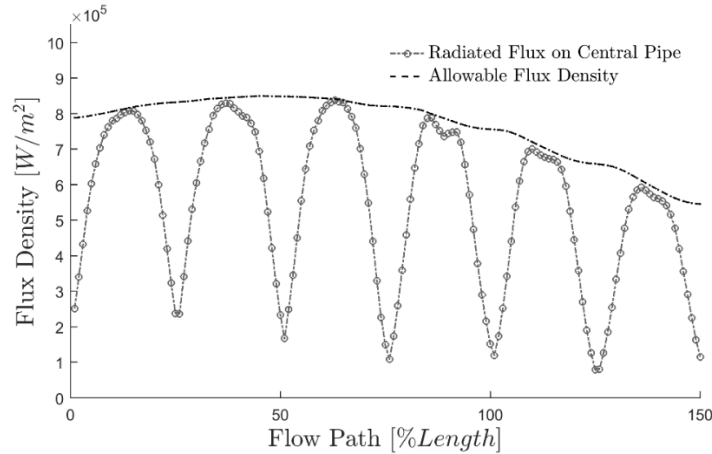


Figure 55. Optical efficiency after convergence, $k = 60$

After 60 iterations, the allowable flux density limit and the simulated irradiated flux on the central pipe for one of the receiver's flow paths is shown in Figure 56 for both the initial configuration of aiming points and the converged solution. It is noteworthy how aiming all heliostats to the receiver's equator is detrimental to the device's integrity. As a result of the above, we can conclude that the proposed controller can find a configuration of aiming points for which the irradiated flux on the receiver's central pipe falls under the allowable flux density.



a)



b)

Figure 56. Allowable flux density limit and irradiated flux on the central pipe for each panel. a) initial conditions for the aiming point configuration, b) after the controller reached steady-state

On the other hand, the flux measurements which could be obtained from a real plant with state-of-the-art methods would include uncertainties. For a preliminary consideration of such errors, the flux resulting from the ray-tracing in STRAL is added to a matrix of uniformly distributed numbers with a maximum amplitude of $100 \frac{Kw}{m^2}$. The results, shown in Figure 57, indicate that the controller finds an aim point distribution despite this measurement noise, which results in a flux density on the receiver below the AFD.

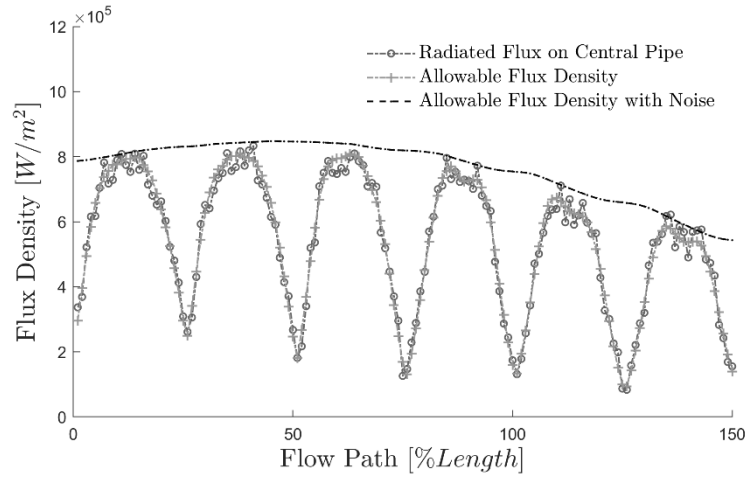


Figure 57. Allowable flux limit and irradiated flux on the central pipe in each panel with uniform noise in the flux measurement

Finally, we have considered a change in the DNI from clear sky to the condition shown in Figure 58. Assuming the DNI conditions persist, the algorithm would then, at each iteration, provide an increment for each heliostat position.

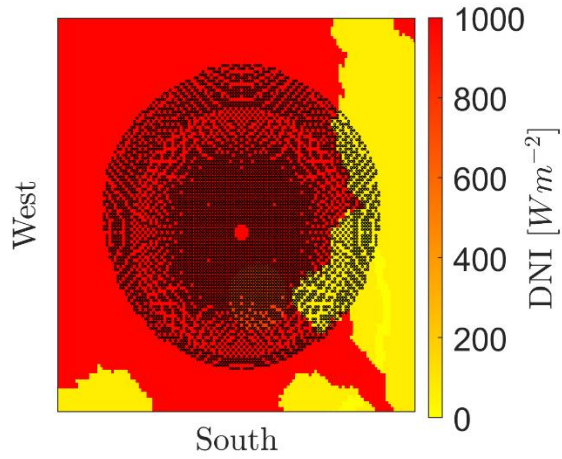


Figure 58. DNI spatial distribution

As shown in Figure 59, after 15 iterations, the algorithm has found a suitable configuration.

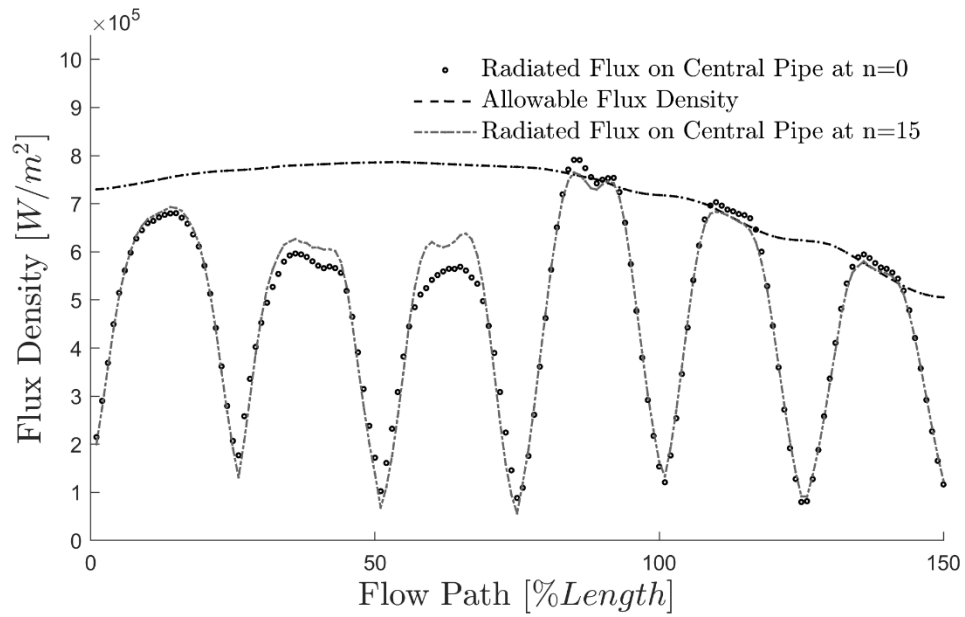


Figure 59. Allowable flux limit and irradiated flux on the central pipe in each panel for iteration n=0 and n=15 after a change in DNI

4.2.1. Tuning the parameters of the feedback controller

First, an investigation into the relationship between the controlled and manipulated variables to determine a tuning strategy was conducted. The dispersion controller was selected to be tuned. In contrast, the centroid controller parameters were fixed, as will be explained in this section.

An open-loop response was obtained for every combination of input-output signals. The initial conditions were determined by the optimal aiming point configuration found in the previous section at noon during the autumnal equinox. A step input change of magnitude 50% CO was inserted as controller output signal and applied to the simulated plant. The sign of the step input was determined by the initial conditions, depending on the controller's value at the initial time; if it is greater than 50 %CO, the sign is negative; on the contrary, it is positive. After letting enough time pass by until the system reached a steady-state, a new step input was applied in the opposite direction to bring back the system to its original state.

The response variables for each group were stored. The procedure was restarted from the initial conditions and repeated for every group. An example of the process reaction curve obtained from one of these experiments is shown in Figure 60.

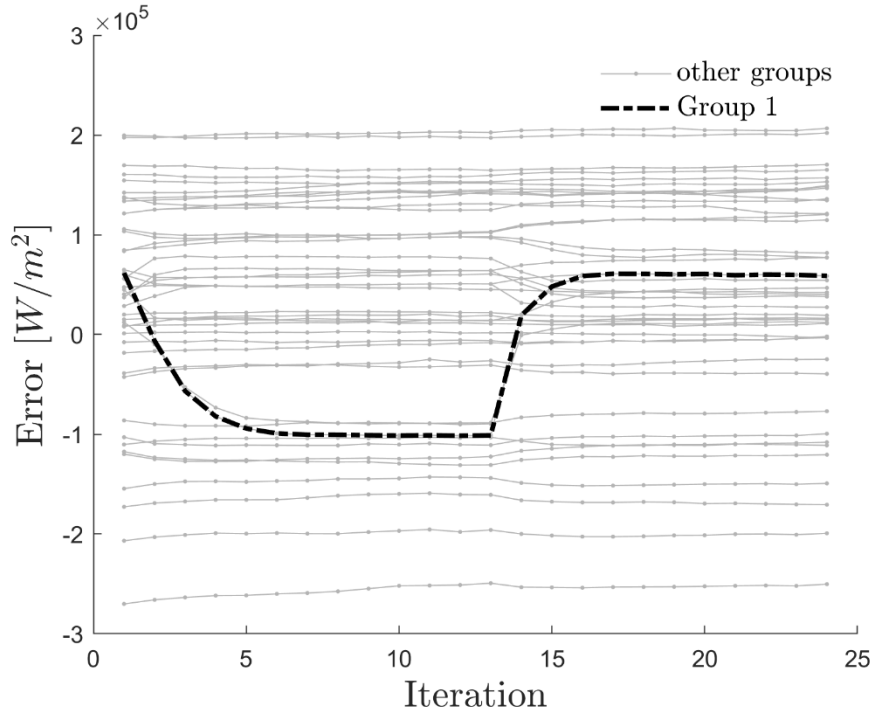


Figure 60. Controlled variables response to a step-change in controller output for group 1

Collecting these data took approximately four weeks, running almost continuously the code (allowing some breaks so the hardware would not overheat) in a laptop with an Intel Core i7 @2.6 GHz, 12 GB-RAM, and a 256 GB-SSD. This long time is because the simulation time needed for the system to reach a new steady-state was about 3 hours even though it was only simulating a 2-minute event, and this was conducted for every group on the solar field. Hence, it is necessary to stress that the tuning procedure could be carried out faster for an actual operating plant, although with much more caution.

After collecting this data, input-output time series were formed and used to estimate a continuous-time transfer function from time-domain data (Ljung, 1987). As can be appreciated in Figure 60, the response can be approximated by a first-order system. By using this model structure as a constraint, the system parameters were identified.

As an example, for group 1, the fitted model has the following structure:

$$\frac{Y_{1,1}(s)}{M_{1,1}(s)} = \frac{3.162 * 10^3}{1.1 s + 1}, \quad (60)$$

with an 88.82 percent fit to estimation data and Mean Squared Error (MSE) of $6.93 * 10^7$. Just like this example, there are 96 identified transfer functions. However, while examining the results, it became evident that heliostats from groups 48 to 96, that is, groups of heliostats farther than 700 m from the tower, had little to no influence in the response variables yielding a near-zero static gain for those transfer functions. As it is shown in Figure 61 with the different behavior for the static gains between groups 1-48 and groups 49-96. Consequently, it was decided to fix the aiming points from groups 49 to 96 and use in the control strategy only those heliostats closer to the tower.

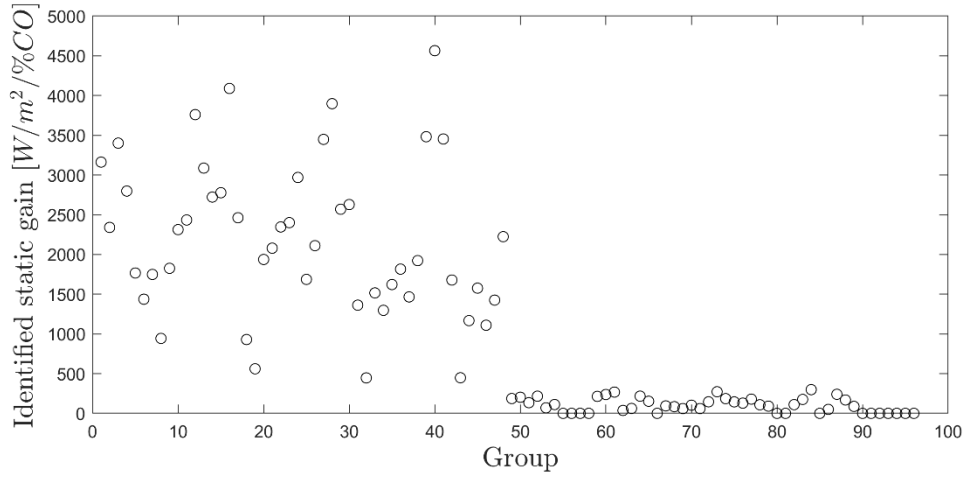


Figure 61. Identified static gains per group (Some outliers have been removed from this plot)

To further investigate the obtained parameters, the results shown in Figure 61 are now organized depending on the groups' geometric location in the solar field. The solar field's slices used to assign the heliostats to the groups have been labeled starting with 1 in the south going anticlockwise, passing the east first, until 12 back at the south, as shown in Figure 62.

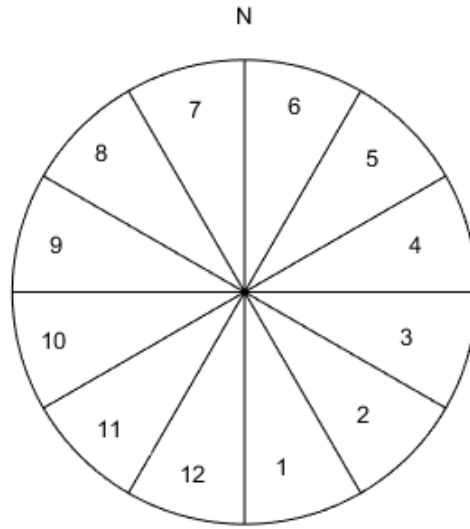


Figure 62. Labels for the geometric location in the solar field of the groups

The static gains for the models following this order are shown in Figure 63. It is also displayed in which quadrant of the receiver's panel each group is assigned.

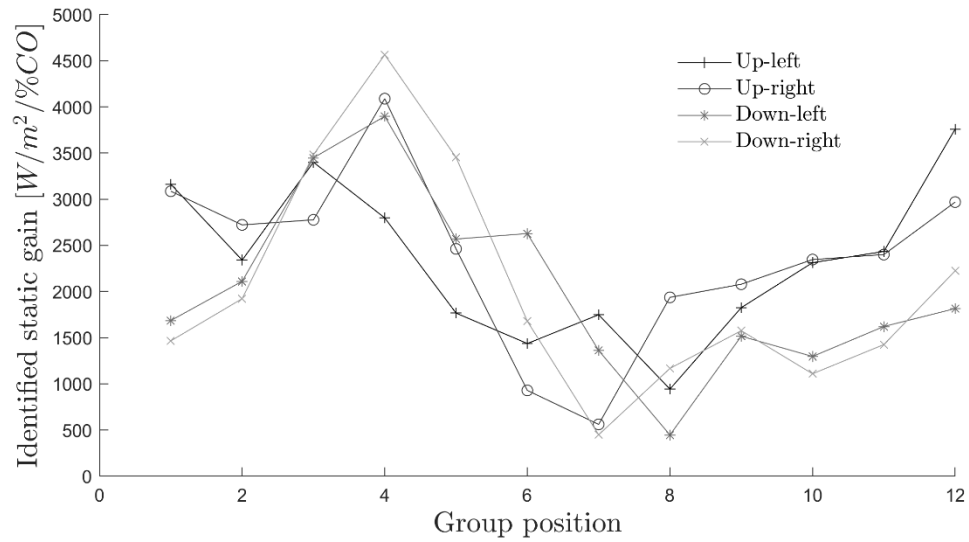


Figure 63. Static gains for the models according to their location on the solar field

Moreover, the time constants found by the estimation method are shown in Figure 64. It was decided to use the median of the time constants as a representative time constant, τ , for all loops.

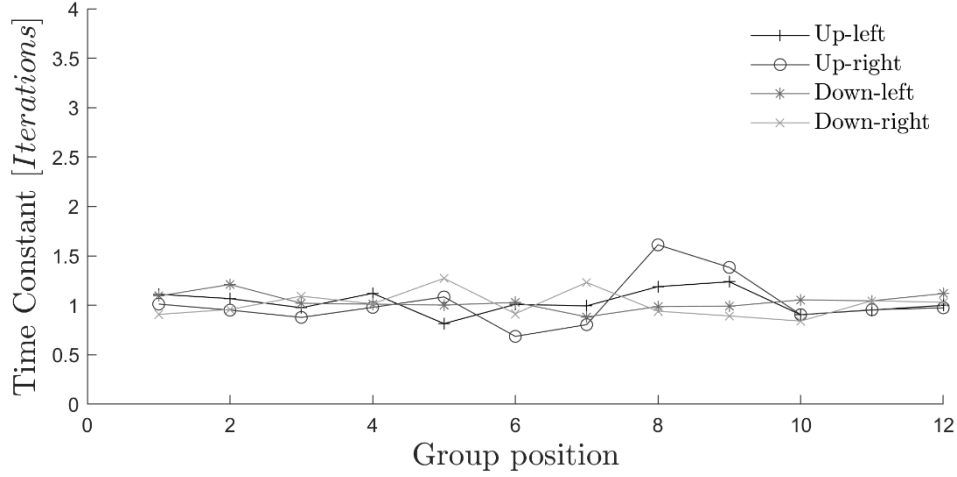


Figure 64. Time constants for the models according to their location on the solar field

The tuning method used follows the controller synthesis equations suggested by Dahlin for a first-order system (C. A. Smith & Corripio, 2006). By using the identified transfer functions, this method suggests a Proportional-Integral (PI) controller structure with a single tuning parameter τ_c . The tuning equation uses the static gain for each group K_i ,

$$K_{ci} = \frac{\tau}{K_i \tau_c}$$

In this work, the system was evaluated under a disturbance for two tuning parameter values. First, for $\tau_c = 10$, which is considered a moderate tuning and then $\tau_c = 100$, a conservative tuning. For this evaluation, a disturbance scenario in the time-lapse between 12:19:00 p.m. and 12:23:30 p.m. on the autumnal equinox was used. We have selected a representative point in the receiver surface to show how the aggressive tuning attempts rapidly to reach the AFD limit, causing an overshoot, while the moderate tuning reaches the setpoint slower, as seen in Figure 65

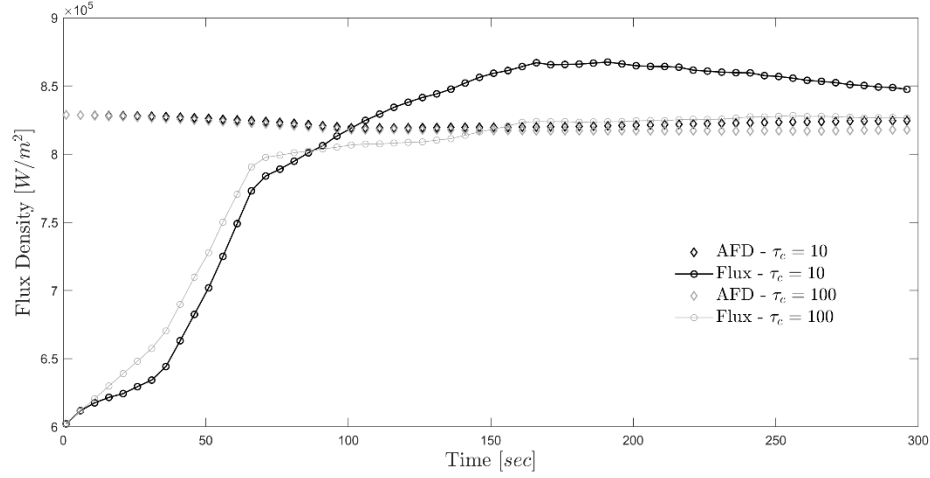


Figure 65. Moderate vs. aggressive tuning result for one point of the receiver between 12:19 and 12:23 p.m. under disturbances

The results indicate that a moderate tuning induces an aggressive response of the system. Furthermore, the behavior of the moderate tuning demands faster movements of the heliostats compared to the conservative tuning. This moderate tuning may cause the strategy to attempt movements for the heliostats beyond the feasible region of operation in terms of the angular speed. Considering that the technique's current implementation does not consider these limits as constraints, conservative tuning is preferred. Hence, it is strongly advised to use a conservative approach for the tuning of the strategy. Based on this conclusion, other works have incorporated the angular speed constraint in implementing the valve analogy (Jesús García et al., 2020).

Using the conservative tuning, i.e. $\tau_c = 100$, the distribution of the proportional gain K_{c_i} for all heliostats in the solar field is shown in Figure 66 and Figure 67.

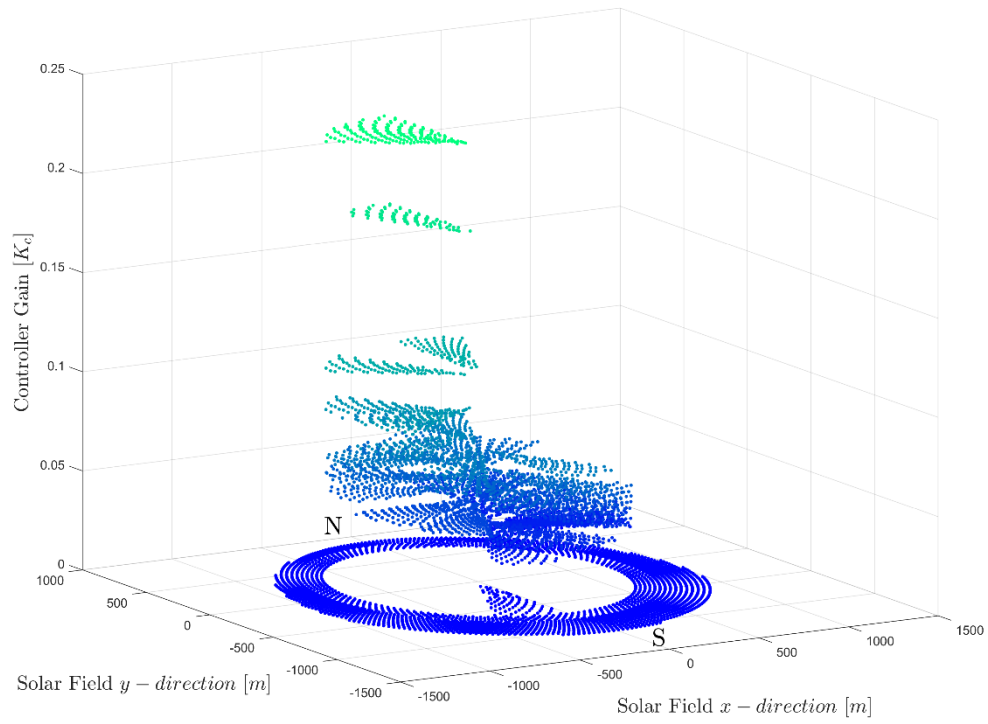


Figure 66. Distribution of the proportional gains for dispersion controllers in the solar field per groups

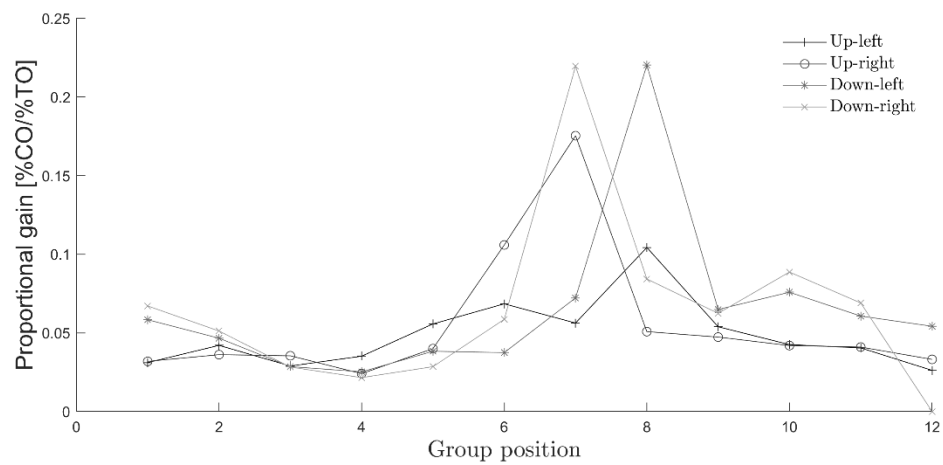


Figure 67. Proportional gains for the controllers according to their location on the solar field

The developed tuning method was tested for the dispersion controller; in the rest of this work, these tuned parameters have been used. Regarding the centroid controllers, a proportional gain of 0.005 was assigned to groups 1 to 48, with zero gain assigned to the rest of the groups' controllers. The integral time value for the centroid controllers was set 3 times higher than the one used for the dispersion controllers. These values would make this controller act significantly slower than the dispersion controllers, which causes a lower effort towards reaching the settling time.

4.2.2. Feedback disturbance rejection

In the following section, the proposed feedback control strategy is tested under an atmospheric disturbance of the solar field by using actual spatially resolved resampled data from the WobaS system to investigate how the proposed strategy reacts. The selected scenario has been chosen from the available data. The duration of this simulation is 4.5 minutes. First, the previous section's strategy was used to find initial conditions and start from a near-optimal aiming point configuration and a clear sky situation. Then, the actual radiation was taken from the WobaS system Data, using the spatially resolved data without time prediction as the actual ground radiation for the solar field.

This scenario, shown in Figure 68, considers the time-lapse between 11:30:00 a.m. and 11:34:30 a.m.

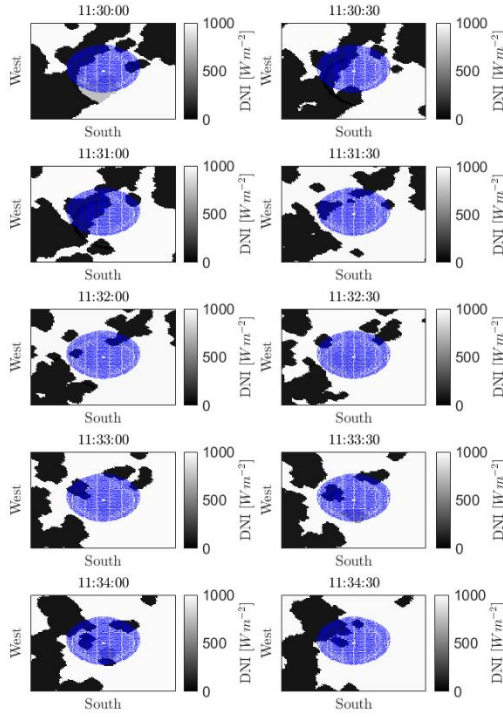


Figure 68. Disturbance Scenario 1

In Figure 69 it is shown the resulting flux of the aiming point configuration, which was found after letting the control strategy converge, as explained in the previous section. This configuration is used as the starting point for the test scenario. The same information is presented in Figure 70, but it is shown in a two-dimensional frame using a linear index to represent each point on the receiver's surface plane. Which was developed to show the time-lapse behavior of the control strategy in a single image.

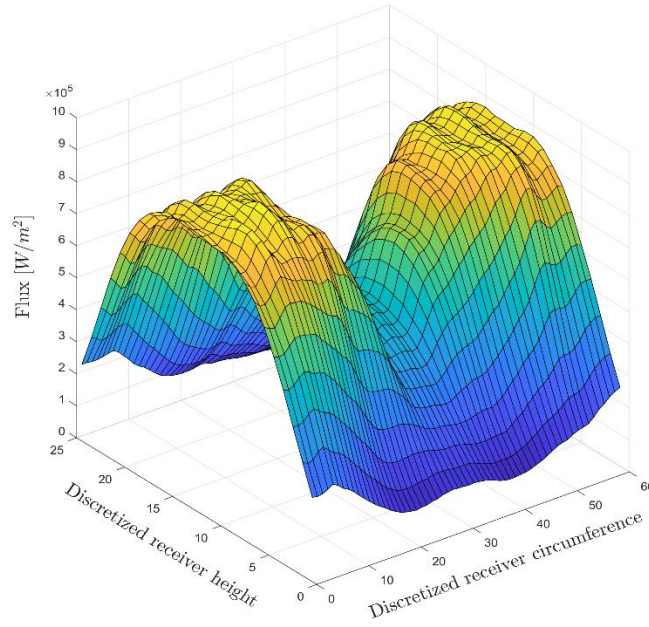


Figure 69. Flux on the receiver at 11:30 a.m. under clear sky conditions for a near-optimal aiming point configuration obtained with the control strategy.

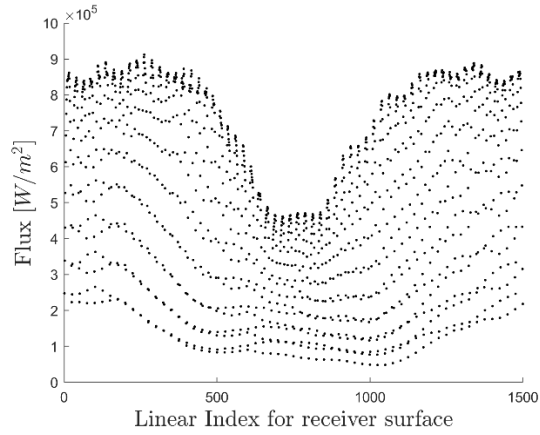


Figure 70. Flux on the receiver at 11:30 a.m. under clear sky conditions, in a near-optimal aim point configuration, using the control strategy, with a linear index to represent the receiver surface.

The following result, Figure 71 and Figure 72, represent the time lapse for the response of the system to this disturbance by overlapping the AFD and Flux for all iterations in a single image.

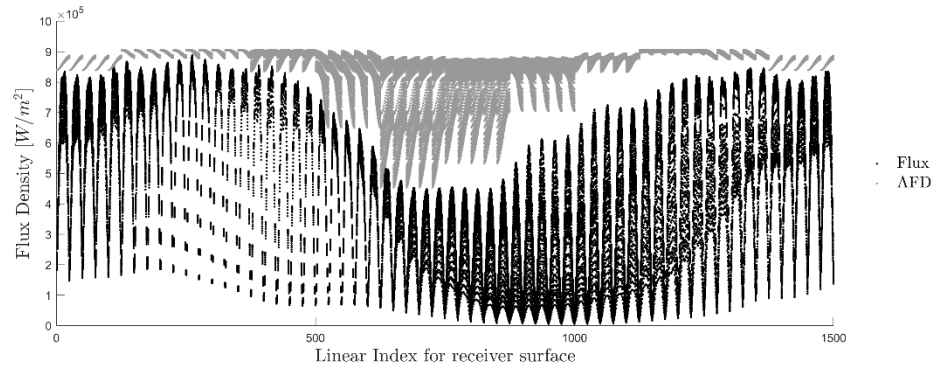


Figure 71. The response of the system with fixed aiming points to the disturbance at 11:30 a.m.

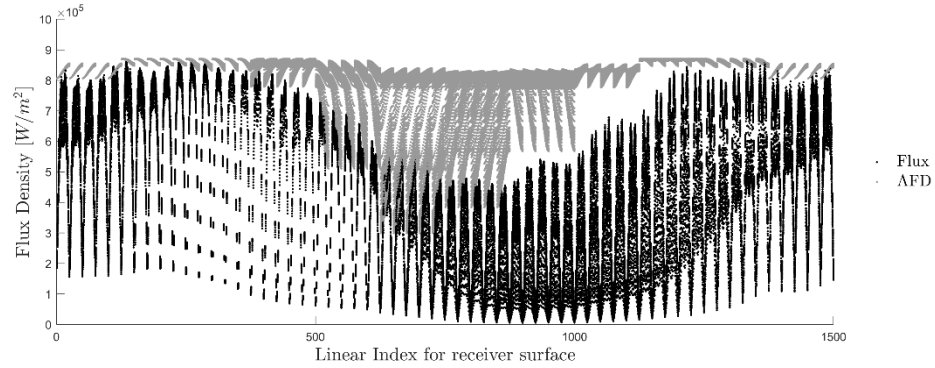


Figure 72. The response of the system with the tuned feedback controller to the disturbance at 11:30 a.m.

It can be appreciated that the controlled system attempts to fill the gap between the AFD and the Flux projected onto the receiver. To further present this, two simple indices have been defined to give a quantitative way to assess the differences between the curves. The first one considers the positive differences between the AFD and Flux at each discrete point on the receiver, while the second one the negative differences. They are scaled differently to account that in most of the operations, there are large areas of the receiver under the AFD. Hence, the cumulative differences at each iteration are divided by 10^8 W/m^2 for the positive index and 10^6 W/m^2 for the negative index.

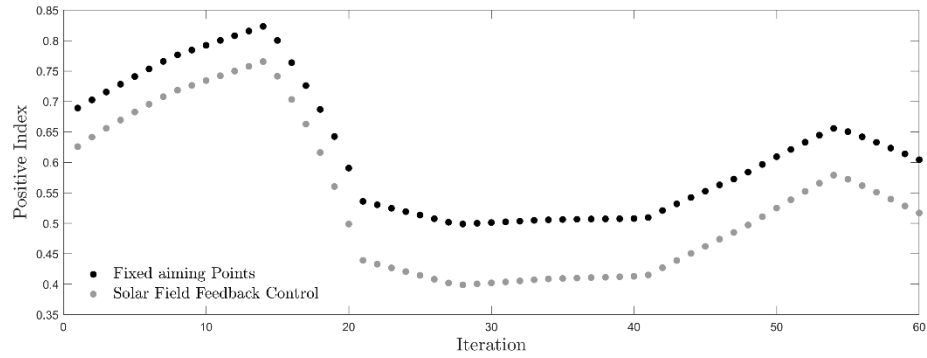


Figure 73. Positive Index for the system's response for fixed aiming points and solar field feedback control under disturbances at 11:30 a.m.

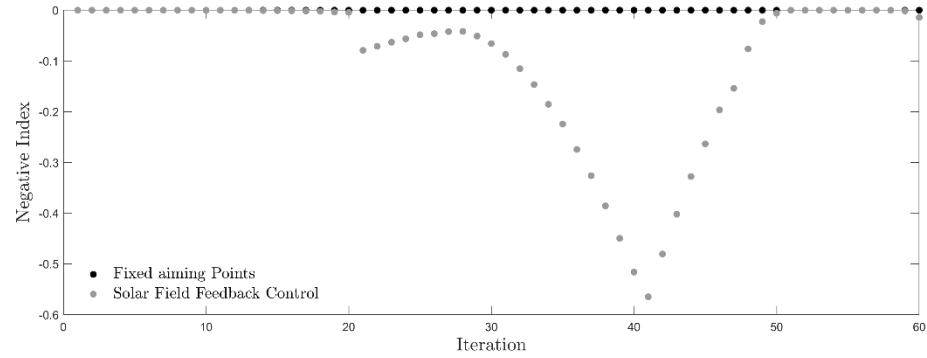


Figure 74. Negative Index for the system's response for fixed aiming points and solar field feedback control under disturbances at 11:30 a.m.

From Figure 73, it is concluded that the solar field control had a better performance than letting the aiming points fixed since the AFD curve and the Flux are nearer according to the positive index, thus, gathering more energy onto the receiver. This comes with a cost. Once the disturbance leaves the solar field, for instance, when the cloud passes, there is a concentration of energy on the receiver, and the controller needs some time to disperse the heliostats. To address this issue, the adaptive control strategy using predicted solar radiation information has been proposed.

4.3. Evaluation of the novel adaptive controller with feedback compensation

One of the main goals set in this work was establishing a pathway to take advantage of the information provided by short-term prediction data of solar radiation in a solar field control strategy for power tower plants. During an internship at the Solar Institute for the DLR, the author gained access to data from a state-of-the-art nowcasting system developed after years of joint European research, the WobaS system, and its operation was explained in previous chapters.

In section 3.1.3, the architecture for the feedback controller was presented. The information from the nowcasting system, as explained in chapter 3, is included by considering an augmented architecture which includes the adaptation engine, which determines the value of k_{FF} . In this section, the value of this gain was fixed at $k_{FF} = 10 \%CO$. In the following subsection, the influence of this parameter was explored in more detail.

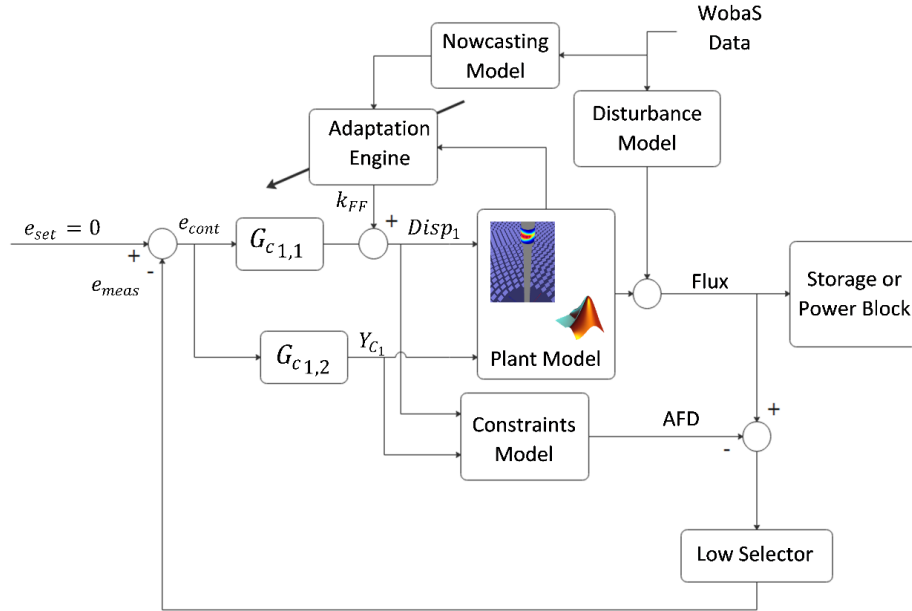


Figure 75. Architecture for the testing of the adaptive control strategy with feedback compensation

In this architecture, the AFD calculation has been included independently as a constraints model, although this work the definition from Vant-Hull was used for the AFD. Advances in the definition of this allowable flux density have been made, for instance, creating databases considering corrosion and thermal stress limits for different material and geometrical properties of the receiver's tubes (Sánchez-González, Rodríguez-Sánchez, & Santana, 2020b).

The Adaptation Engine contains the rules explained in previous sections, and in this work, the nowcasting model refers to the re-sampling of the nowcasting information. The disturbance model symbolizes how a change in solar radiation affects the flux radiated onto the receiver. The controllers $G_{C_{1,1}}$ and $G_{C_{1,2}}$ represent the controllers for the dispersion ($Disp_1$) and centroid Y_{C_1} respectively. Finally, the low selector, which was introduced in previous sections as well, in charge of selecting the point in the sector of the receiver's surface assigned to the group, which more urgently needs to adjust the Flux. The proposed adaptive control strategy with feedforward architecture results to two atmospheric data are presented, one at 11:30 a.m. and one at 12:19 p.m.

For the 11:30 a.m. scenario, it is clear from the positive index plot in Figure 76 that both strategies have similar behavior. When the positive index at each iteration is added, a total of 31.9 is obtained for the adaptive strategy with feedback while 32 for the feedback strategy. Even though the adaptive strategy keeps the flux closer to the AFD, both strategies have roughly the same performance.

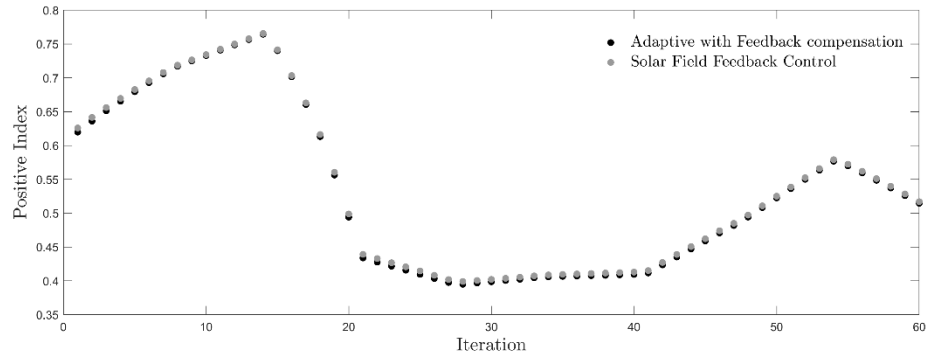


Figure 76. Positive Index results from the adaptive feedforward with feedback compensation strategy and the feedback strategy for a disturbance at 11:30 a.m.

Nonetheless, the negative index reflects the benefits of the proposed strategy, as seen in Figure 77. The controllers could use the nowcasting system's information to disperse before the radiation returns to the solar field once the disturbance leaves the field, decreasing the over-flux period. Adding the index's absolute value for each iteration sums up to 4.7 for the adaptive strategy and 4.9 for the feedback strategy. This corroborates that during this time-lapse, the adaptive strategy kept negative values of the difference between the AFD and the Flux smaller than the feedback strategy.

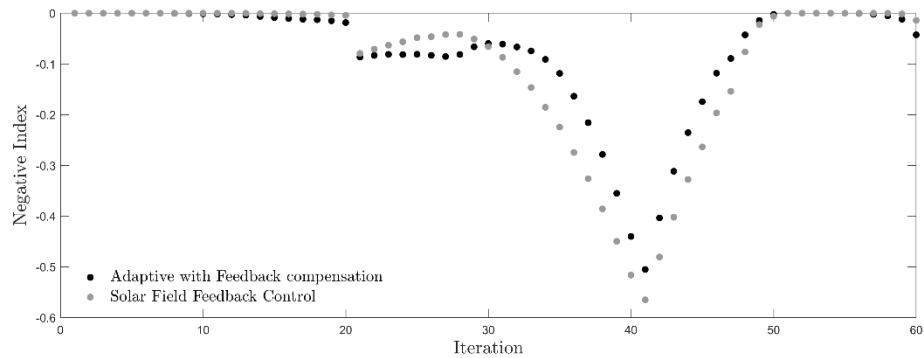


Figure 77. Negative Index results from the adaptive feedforward with feedback compensation strategy and the feedback strategy for a disturbance at 11:30 a.m.

For the 12:19 p.m. scenario, there is also a similar behavior for the positive index, with a total cumulative positive index of 22.3 for the adaptive strategy and 22.2 for the feedback strategy, with a better performance in terms of the negative index for the

adaptive strategy, 76.9 for the adaptive against 80.8 for the feedback strategy. An indicator that during this time-lapse the adaptive strategy kept the negative values of the difference between the AFD and the Flux, smaller than the feedback strategy. In the next section, the strategy is compared to a fixed configuration of aiming points and a mass flow control strategy, which is the industry standard practice.

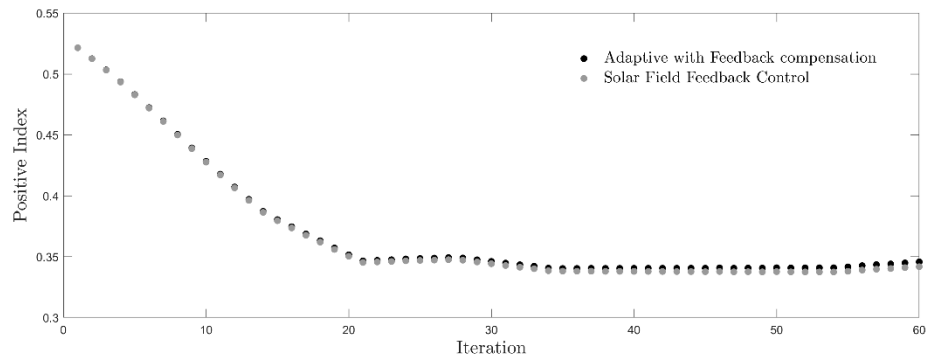


Figure 78. Positive Index results from the adaptive feedforward with feedback compensation strategy and the feedback strategy for a disturbance at 12:19 a.m.

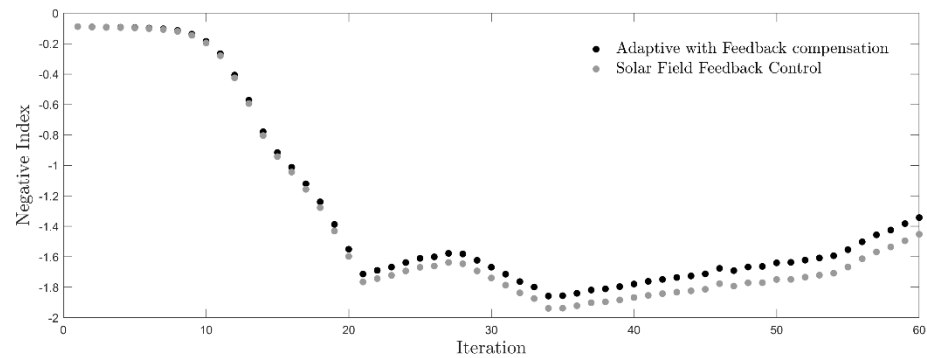


Figure 79. Negative Index results from the adaptive feedforward with feedback compensation strategy and the feedback strategy for a disturbance at 12:19 p.m.

4.3.1. Influence of the adaptive feedforward gain on the controller

The effects of this control parameter on the system behavior were investigated by analyzing two different time-periods with simulations using the following values for the adaptive parameter gain $k_{FF} = \{5, 10, 15, 25\} \%CO$.

In Figure 80, the receiver's intercepted power is shown for 5 minutes, using as disturbance the spatial radiation data from the nowcasting system on May 14th, 2016. The adaptive feedforward gain effect is to disperse the heliostats' aiming points from shaded areas of the solar field where the forecast predicts will be unshaded in the following minute. However, it is appreciated from both Figure 80 and Figure 81 that a smaller gain will preserve more energy focused on the heliostats.

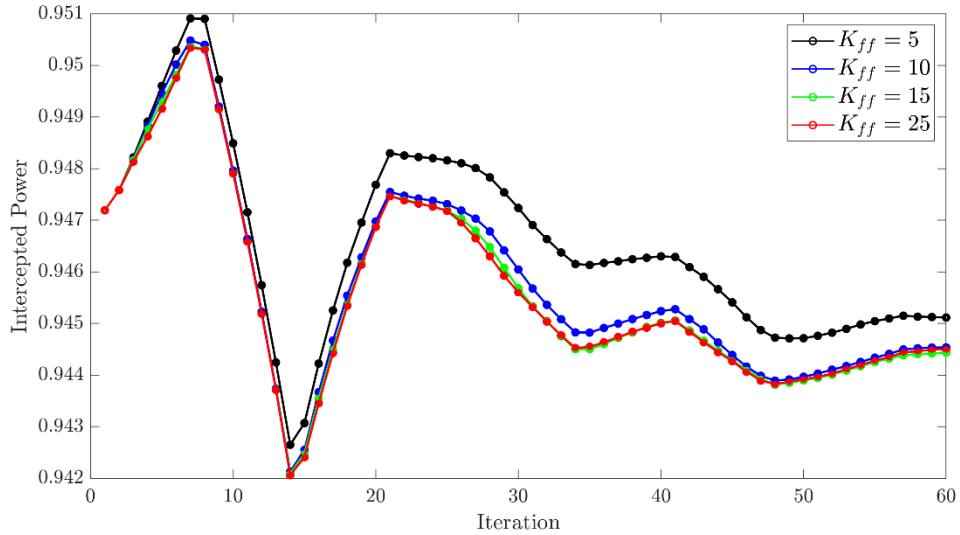


Figure 80. Intercepted power using the adaptive strategy with different feedforward gains at 11:30 a.m.

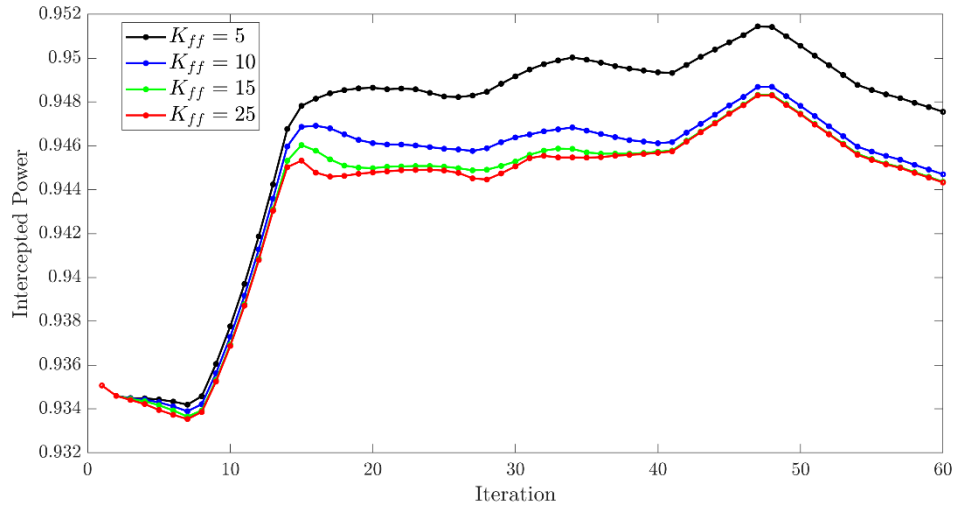


Figure 81. Intercepted power using the adaptive strategy with different feedforward gains at 12:40 m.

The average tracking speed for the heliostats on the solar field in each direction for the time-periods analyzed are shown in Table 3. There is a clear trend towards increasing the tracking speed with a higher adaptive feedforward gain. The controller attempts to disperse the heliostats more aggressively from areas in which the forecast predicts a sudden lack of shadow. The difference between both scenarios responds to the difference in size, path, speed, and transmittance of the cloud passing over the solar field.

Table 3. Average tracking speeds for scenarios starting at 11:30 a.m. and 12:40 a.m. for different values of the adaptive feedforward gain

$k_{FF}, \%CO$	11:30:00 - 11:34:30 a.m.		12:40:00 - 11:44:30 a.m.	
	Azimuth	Elevation	Azimuth	Elevation
	[°/min]	[°/min]	[°/min]	[°/min]
5	2.79	2.48	1.72	2.38
10	2.5	3.76	2.72	3.78
15	3.24	4.11	4.1	4.8
25	3.38	3.88	5.42	5.18

Assuming an upper limit for the system's tracking speed of $9^\circ/\text{min}$ for the elevation and $12^\circ/\text{min}$ in the Azimuth direction. It is concluded that a value of k_{FF} which is a quarter of its possible range results in motions with speeds close to half of the heliostats' maximum speed for the analyzed scenarios. Since the value presented is a mean value, it is strongly recommended as future work to include each heliostat speed limit as a constraint for the valve analogy to ensure that no heliostat is forced into tracking near the maximum boundaries.

4.4. Comparing the proposed strategy in terms of energy gain, thermal stress, and lifetime to an industry-standard practice

The following subsection presents an approach to compare the proposed feedback control strategy with the standard alternative, where the mass flow is modified according to DNI variations (Institut für Solarforschung, 2016). To operate the Solar-Two-receiver, Sandia National Laboratories designed a control algorithm that allows automatic operation in the presence of DNI variation because of cloud passages. The algorithm seeks to maintain outlet molten-salt temperature at 565°C avoiding the receiver pipes' thermal fatigue damage. The initial control algorithm was composed of three independent control signals which regulate the salt flow. Nonetheless, the algorithm was updated with a feature called Cloud Standby. This function served as an alternative to reduce the possibility of receiver damage when clouds disappear, and the heliostats focus full power onto the receiver instantly. The final algorithm used only two independent signals: a feedforward signal composed of eight photometers and a feedback signal from the molten-salt outlet temperature given by thermocouples. Both signals are summed to determine a total flow setpoint on a PI controller that manipulates the flow control valve.

Using the models' temperature distributions and considering an approximation of two-dimensional thermoelasticity, it is possible to calculate the thermally induced stresses

in the tubes. If the temperature distribution is expanded as a Fourier series as shown by the following equation:

$$T(r, \theta) = A_0 + B_0 \ln \frac{r}{a} + \left(\frac{C_0}{r} + C_1 r \right) \cos \theta + \left(\frac{D_0}{r} + D_1 r \right) \sin \theta \quad (61)$$

$$+ \left(\frac{C_0'}{r^2} + C_1' r^2 \right) \cos(2\theta) + \left(\frac{D_0'}{r^2} + D_1' r^2 \right) \sin(2\theta)$$

It is possible to use the least square method to solve for the unknown parameters by using the temperature's inside and outside of the pipe (Kim, Potter, Gardner, Too, & Padilla, 2017).

With the parameters of the Fourier series identified, it is then possible to calculate the thermoelastic stresses in the tubes as explained in chapter 2, just considering that for the calculation of the stress, only the following terms for the temperature distribution are considered $T_a = A_0$, $(T_a - T_b) = B_0$, $F_{10} = C_0$ and $G_{10} = D_0$.

Also, it is necessary to consider the pressure stress, and since the ratio of inner radius to tube thickness is less than 10, thick-wall calculations are used (Neises, Wagner, & Gray, 2014a), which for internal pressure p_i results in:

$$\sigma_{rr} = \frac{p_i a^2}{b^2 - a^2} \left(1 - \frac{b^2}{r^2} \right), \quad (62)$$

$$\sigma_{\phi\phi} = \frac{p_i a^2}{b^2 - a^2} \left(1 + \frac{b^2}{r^2} \right), \quad (63)$$

and:

$$\sigma_{zz} = \frac{p_i a^2}{b^2 - a^2}. \quad (64)$$

By superimposing both pressure and thermal stresses, finding the stress field on the tubes is possible.

For the proposed solar field control operation strategy, it is convenient to recall that several panels form the receiver. The solar field is divided into several groups of heliostats, which are assigned using geometric considerations with corresponding areas of the panels on the receiver. The aiming points for heliostats in some of these groups are aimed to the left of the center of a panel, and some are aimed to the right. These aiming points can move from the equator of the panel towards the edges of the receiver. The solar field controller used consists of a set of simple proportional-integral (PI) controllers, where the objective is to hold the flux density radiated onto the section of the panel assigned to the group as close to a calculated Allowable Flux Density (AFD), which depends on measurable plant parameters.

In this work, we consider that the flux distribution on the receiver is available, which in a real plant can be achieved either by reconstructing the flux using photometers as in Solar Two or with more modern approaches using infrared cameras. The setpoint to the controllers determines how distant the flux and the allowable flux density can be. The setpoint for each PI controller is named Gap and valued zero. In each iteration, the controlled variable for a group corresponds to the smallest value from the difference between the AFD and the flux on that group's panel section, which means that the controller acts based on the information from the surface point in the panel closer to the allowable limit.

Moreover, the manipulated variables are the dispersion of the group of heliostats and the group's centroids' distance from the panel's equator. An increase in the controller output signal will disperse the aim points and move them farther from the equator. On the contrary, a decrease in the controller output will bring them closer to the panel's equator and concentrate them. Furthermore, each PI-controller has been adapted using both the nowcasting radiation information and the change rate of the controlled variable. Figure 82 presents a comparison of the molten-salt outlet temperature between the two strategies. It is observed a significant amount of energy obtained when

the proposed strategy is implemented. Now, the fatigue life's impact must be considered to establish whether the material integrity is affected or not.

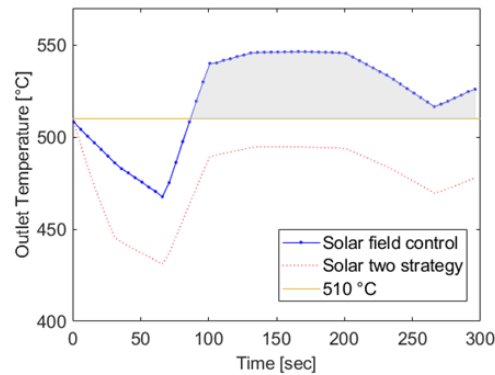


Figure 82. Outlet temperature for both operation strategies. The shaded area represents molten salt, which could be directed to the hot tank.

Since the first report prepared for Sandia Laboratories in 1979 (Berman, Gangadharan, Gupta, & Narayanan, 1979), where an interim standard was proposed to evaluate the reliability required in solar power applications, a significant amount of work has been published in this field. Those investigations aimed to study the effects of considering equal the pipes' behavior in boilers or nuclear facility components and central receivers. The significant cyclical behavior that faces the receiver due to the solar plant's inherent operation or the conservative safety factors could lead to fatigue failure and oversizing the receiver, respectively (Neises, Wagner, & Gray, 2014b). The failure analysis conducted in this section is divided into the stress and the fatigue analysis.

First, the thermal stresses to which solar central receivers are subjected due to the variations of solar radiation make the structural design of the equipment critical. A consequence of the extensive and heterogeneous influence of clouds on surface solar irradiance is that central receivers are subject to spatial and temporal variability on the incoming concentrated direct normal irradiance (DNI). In this part, the analysis is based on a linear-elastic model as introduced in chapter 2, obtaining the thermomechanical stresses in the tubes for the proposed operating and boundary conditions. These stresses

are estimated analytically with the equations presented in (Hetnarski & Eslami, 2009b; Neises et al., 2014b), which describe both the effect of pressure and the mechanical behavior of a non-axisymmetrically heated thick tube. The equations are discussed in detail in (Marugán-Cruz, Flores, Santana, & García-Villalba, 2016; Montoya, Rodríguez-Sánchez, López-Puente, & Santana, 2018). Marugán-Cruz et al. (Marugán-Cruz et al., 2016) examined the Biot number's dependence and the accuracy when the temperature profile is a function of r and θ . Montoya et al. (Montoya et al., 2018) compared the analytical approach with a Finite Element Analysis (FEA). The thermomechanical model used is composed of equations (65)-(67) that describe the stresses lead by the thermal effect and the equations (62)-(64) describing the stresses caused by the internal pressure of the molten salt.

$$\sigma_{T,rr} = \frac{E\alpha B_0}{2(1-\nu)} \left[-\ln \frac{r}{a} + \frac{b^2}{b^2 - a^2} \left(1 - \frac{a^2}{r^2} \right) \ln \frac{b}{a} \right] \quad (65)$$

$$+ \frac{E\alpha r}{2(1-\nu)(b^2 - a^2)} \left(1 - \frac{a^2}{r^2} \right) \left(1 - \frac{b^2}{r^2} \right) (C_0 \cos \phi + D_0 \sin \phi)$$

$$\sigma_{T,\theta\theta} = \frac{E\alpha B_0}{2(1-\nu)} \left[-1 - \ln \frac{r}{a} + \frac{b^2}{b^2 - a^2} \left(1 - \frac{a^2}{r^2} \right) \ln \frac{b}{a} \right] \quad (66)$$

$$+ \frac{E\alpha r}{2(1-\nu)(a^2 + b^2)} \left(3 - \frac{a^2 + b^2}{r^2} - \frac{a^2 b^2}{r^4} \right) (C_0 \cos \phi + D_0 \sin \phi).$$

$$\sigma_{T,zz} = \nu(\sigma_{T,rr} + \sigma_{T,\theta\theta}) - E\alpha(T - T_0). \quad (67)$$

The value T_0 considers the contribution at each point of the cross-section and its relation to the average cross-sectional temperature. To implement this and calculate the axial stress for all elements in a discrete axial slide (cross-section) of the pipe, the average temperature only in that cross-section was used in this work. It was calculated for each discretized axial element by a discretized implementation of the surface integral of the temperature with respect to the cross-section area. Then for each element in the mesh, the stress was obtained using the respective average found for each axial

element. Assuming generalized plane strain at each slice of a 3D tube independently of all other slices is a valid approximation (William Logie, personal communication, May 11th, 2020):

$$T_0 = \frac{1}{A} \int_A T dA \cong \frac{1}{A} \sum T \Delta A. \quad (68)$$

The stress model presented uses the temperature distribution over the pipe, the internal pressure, and the receiver's geometric properties. As a result, the thermomechanical stresses are calculated at each step as the solar plant operates either using the Solar Two or the proposed strategy.

The assumption of a linear-elastic behavior considers that the material's work is stored as potential energy. Therefore, using the Von Mises criterion, presented in equation (69), the pipe's equivalent stresses in the operation modes are calculated. In Figure 83, the equivalent stress in a cross-section of one tube is shown.

$$\sigma_{eq} = \sqrt{\frac{\sum[(\sigma_{rr} - \sigma_{\theta\theta})^2 + (\sigma_{\theta\theta} - \sigma_{zz})^2 + (\sigma_{zz} - \sigma_{rr})^2]}{2}} + 3\tau_{r\theta}^2} \quad (69)$$

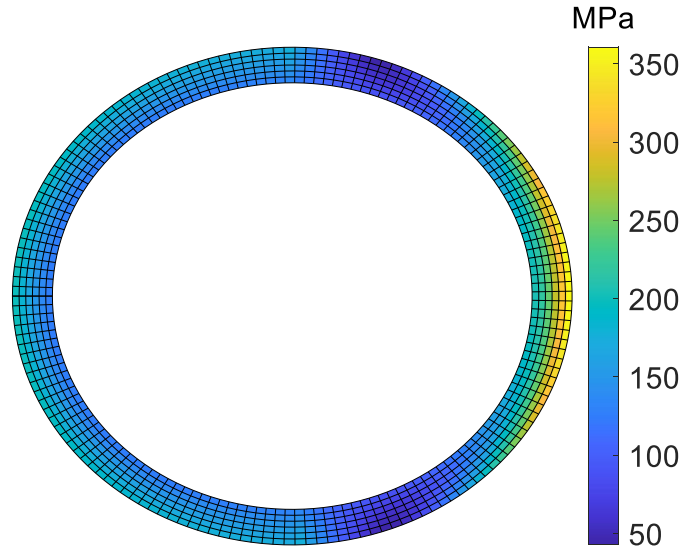


Figure 83. Equivalent stress

Six (6) points are selected in each panel's equator to study how the equivalent stresses change in the flow paths over the time period. These results are presented in Figure 84. The blue lines indicate the equivalent stress behavior using the proposed control strategy. On the other hand, the red ones represent the Solar Two strategy's effect on the receiver. The receiver faces irregular loading behavior when disturbances occur, no matter which operation mode is used. Hence, a fatigue analysis should consider this loading behavior properly.

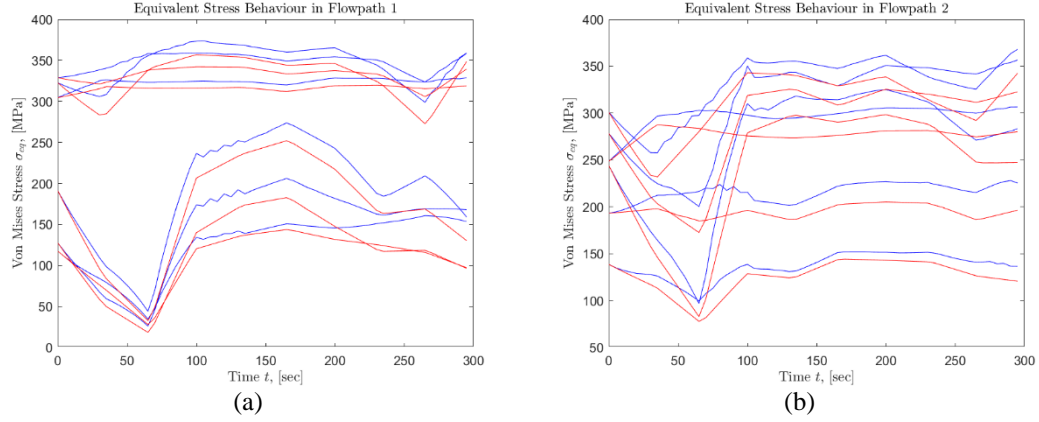


Figure 84. Equivalent stress evolution over the transient period for Inconel 625 in the (a) flow path 1 and (b) flow path 2 of the solar receiver.

However, the loading possibilities for materials during their operating life are vast; specimens are commonly tested for fatigue under sinusoidal loads. The loading profile is divided into two components: the mean stress and the stress amplitude if the cycles are considered symmetric. However, fatigue loadings usually involve stress amplitude that changes irregularly with time, with no symmetric loads. An alternative to investigate nonsymmetric stress loads is the methodology proposed in the ASTM standard No. E1049-85 of 2017, called Rainflow Cycle Counting. The number of load change cycles can be estimated as a cycle amplitude function from an irregular load vs. time history (as presented in Figure 84). A detailed exposition about this methodology can be found either in the ASTM standard or Dowling (Dowling, 1999).

In this dissertation, the rainflow cycle counting was carried out using MathWorks's algorithm in its Signal Processing Toolbox. For each operation, the algorithm yields new sets of equivalent mean and alternating stresses. Consequently, the effect of the mean stresses $[\sigma_m]$ on the limiting value of the stress amplitudes $[\sigma_a]$ must be considered. A simple way to achieve this is through the modified Goodman equation, which finds a set of modified amplitude stresses, $S_{a,eq}$, over the time-period:

$$\frac{\sigma_a}{S_{a,eq}} + \frac{\sigma_m}{S_{ut}(T)} = 1 \quad (70)$$

For this analysis, we considered the phenomenon known as Yield Strength Anomaly (YSA), which affects superalloys like the Inconel 625 by affecting its mechanical properties over a limited temperature range (D. Liu, Zhang, Qin, & Ding, 2017). For the analysis in this section, the ultimate tensile stress was adjusted [$S_{ut}(T) = 801MPa$] according to the experimental data presented by De Oliveira et al. (De Oliveira et al., 2019), who tested the fatigue life of the Inconel 625 at high temperatures.

The next step in the analysis consists of estimating a Stress-Life curve called the S-N curve for the Inconel 625. Defining the life spectrum where the low cycle fatigue (LCF) and high cycle fatigue (HCF) occur. In this work, the selection is based on the experimental analysis presented in (Kashaev, Horstmann, Ventzke, Riekehr, & Huber, 2013; Rojas-Morín & Fernández-Reche, 2011). LCF and HCF zones are defined in the intervals of [101,103] and [103,106] cycles. However, these limits are dependent on the material and its properties. Thus, experimentation should be conducted to reduce uncertainty for future analysis. Using an empirical correlation, the fatigue stress at 10^3 cycles to failure is estimated (Rojas-Morín & Fernández-Reche, 2011):

$$S_{1000} = 0.9 \times S_{ut}, \quad (71)$$

This point is labeled A in the S-N curve presented in Figure 85. A second point B representing the fatigue limit of the Inconel 625 at 10^6 cycles is calculated as follows:

$$S_e = 0.5 \times S_{ut}, \quad (72)$$

The previous equation is used as a first attempt to determine the fatigue limit by assuming that the receiver pipes are smooth. However, this consideration could lead to conservative results because it does not capture the effect of manufacturing processes or environmental conditions on the material. To consider this effect, a surface factor k_a modifies the initially estimated fatigue limit. Hence, studying the fatigue behavior

of a rougher pipe surface than the one assumed smooth. The surface factor is obtained as:

$$k_a = a \times S_{ut}^b \quad (73)$$

Where parameters a and b depend on how the material surface is finished. For this study, the Inconel 625 is considered to be produced by hot rolling and annealed at 90°C for two hours, as in Pereira et al. (Pereira, Lourenço, Nascimento, & Castro, 2018), therefore, a and b take the values of 57.7 and -0.718, respectively (Dowling, 1999). This yields a modified fatigue limit of $S_{e,md} = 190.3 \text{ MPa}$, which was calculated using equation (74) and is labeled as C in the S-N curve.

$$S_{e,md} = k_a \times S_e \quad (74)$$

Figure 85 summarizes the resulting lines A-B and A-C, representing the material's fatigue behavior on a Log-Log scale, under the temperature conditions obtained from the thermal model and the surface conditions. Finally, the modified amplitude stresses calculated are located within the S-N curve to determine if they are in the LCF or HCF zone. As observed in Table 4, for the highest stress conditions reached by the receiver pipes, neither the Solar Two strategy nor the proposed solar field control strategy leads the pipes to fail in the mentioned fatigue zones. The fact that the highest stresses obtained are lower than the modified fatigue limit supports this conclusion. We then conclude that for the analyzed scenarios, the stresses are located beyond the 10^6 cycles to failure.

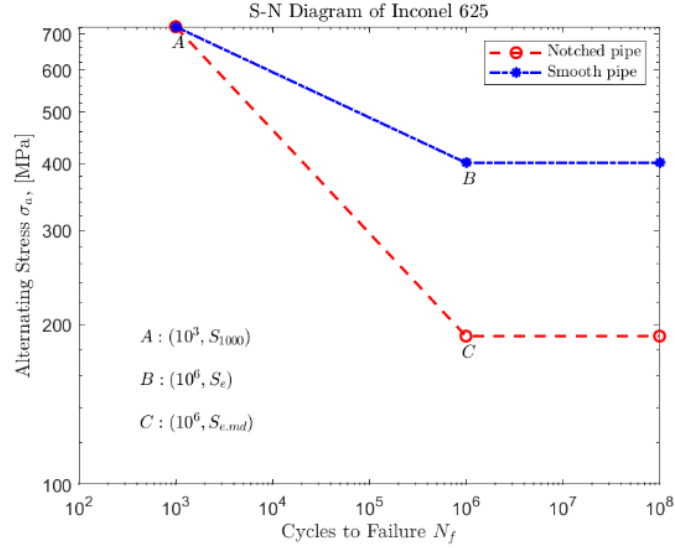


Figure 85. An estimate of S-N fatigue curve for Inconel 625

Dowling (Dowling, 1999) recommends extrapolating the stress-life relationship that rules the HCF zone (A-C) below the fatigue limit to make a life estimation of the material because the hypothesis of a horizontal line on the S-N after 10^6 cycles is not a rigorous approach. The equation that represents the high cycle fatigue behavior has the following structure:

$$\sigma_a = A \times N_f^B \quad (75)$$

Where N_f represents a specific number of cycles to a failure caused by the fatigue strength, σ_a . The terms were fitted using MATLAB, obtaining the parameters: $A = 2.75 \times 10^3$ and $B = -0.19$. With this equation, it is possible to calculate the cycles to failure associated with the operation modes, as shown in Table 4.

Table 4. results of the fatigue analysis for both operation strategies

Stress-Life Condition	Solar Two Strategy		Proposed Control Strategy	
	Flow path 1	Flow path 2	Flow path 1	Flow path 2
Highest	133.3 MPa (6.3×10^6 cycles)	141.2 MPa (4.7×10^6 cycles)	143.1 MPa (4.4×10^6 cycles)	154.7 MPa (2.9×10^6 cycles)
Lowest	0.04 MPa (1.5×10^{25} cycles)	0.01 MPa (2.0×10^{27} cycles)	0.02 MPa (4.4×10^{26} cycles)	0.06 MPa (1.1×10^{24} cycles)

From these results, we conclude that neither scenario, the controlled solar field, nor the cloud-standby mass flow strategy produced thermomechanical stresses, which assuming a linear elastic model, would impact the lifetime of the receiver tubes. Also, the controlled aiming point strategy for that time was able to gain an average enthalpy of 378 MW_{th} , which would have been redirected to the cold tank instead.

Even though 5 minutes is not a significant amount of time to investigate the estimated lifetime, the methodology is proposed and the possibility is open to use a more extended period which could lead to robust datasets of atmospheric disturbances and corresponding thermal stresses. Further research questions arose during this time in the dissertation concerning dynamical thermal stresses and the impact of the clips used to fix the tubes to the receiver and the reactions induced by them. Those clips could be considered stress concentrators in some areas of the pipe, affecting the fatigue life of the receiver pipes. Regarding dynamical stresses, it has been numerically determined that three-dimensional transient thermal stresses in a finite circular cylinder under non-axisymmetric temperature distribution can be higher than the steady-state stresses (Takeuti & Nod, 1980). As can be seen in Figure 86, where the author shows the axial stress (y-axis) along the lateral surface (x-axis) for a cylinder with a heat supply in the circumference of finite width, between time $t = 0.1$ and $t = \infty$.

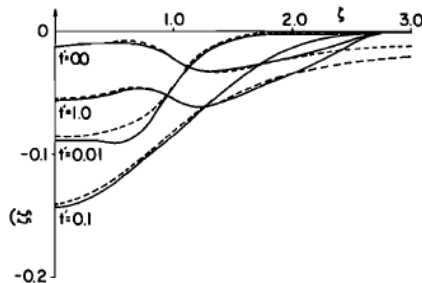


Figure 86. Axial-stress distribution on lateral surface of cylinder, taken from (Takeuti & Nod, 1980)

5. CONCLUSIONS

The contributions of this work to the state of the art of CSP technology begin with the modifications proposed to the valve analogy, which made it applicable in a larger simulated power plant. Moreover, the feedback control architecture proposed, and the tuning procedure developed are transferable to experimental facilities.

The proposed feedback loop found an interesting application which is to be able to provide a near-optimal aiming point configuration relatively quickly in comparison with optimization methods and with low computational effort. It was shown for a reference power plant with 6482 heliostats and thermal power of 450 MW_{th} that the strategy was able to provide aiming points leading to a near-optimal configuration, even starting from a worst-case scenario. It did so with limited computer resources and found the aiming points fast.

A methodology was also developed to analyze the impact of thermal stresses on the lifetime of the receiver using the feedback compensation. Two plant control strategies were examined using the data available. The advantages of the solar field control were an increment in the enthalpy of the fluid during the examined time without impacting the lifetime of the receiver's tubes. The proposed methodology could be improved by more sophisticated AFD modules that consider dynamical thermal stresses and the impact of the clips used to fix the tubes on the receiver and the reactions caused by them. However, the methodology itself is a contribution to the field of CSP since, given a larger dataset of atmospheric disturbances, it can be used to determine the impact of the induced thermal stresses on the receiver.

A method was proposed to tune the feedback controller parameters, and it was tested for the dispersion loop on the simulated reference power plant. The proposed tuning procedure depends only on one parameter. It was shown that an aggressive tuning results in fast movements of the heliostats, which might not be mechanically feasible and can cause oscillations around the desired setpoint.

During tuning, the groups formed by heliostats in distances greater than a fixed radius of 700 m for the reference power plant had a small influence in the controlled variable compared with the other groups, as the relation between the means for the static gains of these two sets of groups differ in almost one order of magnitude. The value for this radius was fixed following recommendations from experts in solar field design from the Solar Institute at the DLR while implementing the control strategy for the reference power plant, to separate groups farther and closer to the central tower, the radius of the projected image of the heliostats onto the receiver. It escapes the scope of this study, but it is recommended as further research to examine this value parametrically. Towards implementing this strategy on an actual plant, the author recommends fixing this radius near half of the distance to the farthest heliostat and then decreasing this radius by half to compare both results and decide an appropriate intermediate value.

A parameter fixed during this study, which is essential to the modifications to the valve analogy, was the distance separating the horizontal position for the desired centroids of the aiming points within each group. This value was set equal to the width of the receiver's panels, as to have two equidistant vertical paths for the horizontal centroid position for the group. This concept has been further explored, and a novel approach following the idea, but exploring different pathways to the ones proposed in this work, has been published by Garcia et al. (Jesús García et al., 2020). It was found on that work that the heat flux variation on the receiver over time depends on the spatial region, with the center exhibiting a first-order response and edges of the receiver showing an underdamped dynamic response.

Another contribution of the work to the CSP field, derives from the adaptive rule proposed to incorporate information, using an index defined in this work, from a nowcasting system into a control strategy for a solar field. Together with the feedback compensation loop and the constraints model, this strategy was tested in a simulated reference power plant subjected to information from a real nowcasting system subjected to actual atmospheric disturbances. In the scenarios presented, the strategy

incorporating the nowcasting information compensated for the negative impact caused by clouds leaving the solar field, avoiding exposure of the receiver to abrupt temperature changes. The intercepted power for different values of the proposed strategy parameter was examined, also the tracking speed of the heliostats demanded by the controller. It was found that the mean heliostat speed for the examined scenarios was inside boundaries, but individual heliostats might escape this limit.

Among future work, it is recommended to consider heliostat's tracking speeds as constraints for the valve analogy to ensure no heliostat is forced into tracking near its maximum boundaries. Furthermore, one possible line of research could compare the robustness of the optimization against the control approach when the heliostats are subject to tracking errors. A final remark, is that it is imperative to promote measuring the direct normal radiation resource in Colombia, to better understand the feasibility of concentrated solar applications.

BIBLIOGRAPHY

- Abutayeh, M., Padilla, R. V., Lake, M., Lim, Y. Y., Garcia, J., Sedighi, M., ... Jeong, K. (2019). Effect of short cloud shading on the performance of parabolic trough solar power plants: motorized vs manual valves. *Renewable Energy*, 142, 330–344. <https://doi.org/10.1016/j.renene.2019.04.094>
- Agrafiotis, C., Storch, H. Von, Roeb, M., Sattler, C., Von Storch, H., Roeb, M., & Sattler, C. (2014). Solar thermal reforming of methane feedstocks for hydrogen and syngas production — A review. *Renewable and Sustainable Energy Reviews*, 29, 656–682. <https://doi.org/10.1016/j.rser.2013.08.050>
- Ashley, T., Carrizosa, E., & Fernández-Cara, E. (2017). Optimisation of aiming strategies in Solar Power Tower plants. *Energy*, 137, 285–291. <https://doi.org/10.1016/j.energy.2017.06.163>
- Ashley, T., Carrizosa, E., & Fernández-Cara, E. (2019). Continuous optimisation techniques for optimal aiming strategies in solar power tower plants. *Solar Energy*, 190(January), 525–530. <https://doi.org/10.1016/j.solener.2019.08.004>
- Astolfi, M., Binotti, M., Mazzola, S., Zanellato, L., & Manzolini, G. (2017). Heliostat aiming point optimization for external tower receiver. *Solar Energy*, 157, 1114–1129. <https://doi.org/10.1016/j.solener.2016.03.042>
- Åström. (2006). *Advanced PID control*. Research Triangle Park, NC: ISA-The Instrumentation, Systems, and Automation Society.
- Ballestrín, J., Burgess, G., & Cumpston, J. (2012). Concentrating Solar Power Technology. In *Concentrating Solar Power Technology*. <https://doi.org/10.1533/9780857096173.3.577>

- Bauer, T., Pfleger, N., Laing, D., Steinmann, W.-D., Eck, M., & Kaesche, S. (2013). *20 - High-Temperature Molten Salts for Solar Power Application* (F. Lantelme & H. B. T.-M. S. C. Groult, eds.). <https://doi.org/https://doi.org/10.1016/B978-0-12-398538-5.00020-2>
- Belhomme, B., Pitz-Paal, R., Schwarzbözl, P., & Ulmer, S. (2009). A new fast ray tracing tool for high-precision simulation of heliostat fields. *Journal of Solar Energy Engineering, Transactions of the ASME*, 131(3), 0310021–0310028. <https://doi.org/10.1115/1.3139139>
- Belhomme, Boris, Pitz-Paal, R., & Schwarzbözl, P. (2014). Optimization of heliostat aim point selection for central receiver systems based on the ant colony optimization metaheuristic. *Journal of Solar Energy Engineering, Transactions of the ASME*, 136(1), 1–7. <https://doi.org/10.1115/1.4024738>
- Benavides, J., Cadena, Á., González, J. J., Hidalgo, C., & Piñeros, A. (2018). *Mercado eléctrico en Colombia: Transición hacia una arquitectura descentralizada*.
- Bergman, T. L., & Lavine, A. S. (2017). *Fundamentals of heat and mass transfer*.
- Berman, I., Gangadharan, A., Gupta, G., & Narayanan, T. (1979). *An interim structural design standard for solar energy applications*. Albuquerque, New Mexico.
- Besarati, S. M., Padilla, R. V., Goswami, D. Y., & Stefanakos, E. (2013). The potential of harnessing solar radiation in Iran: Generating solar maps and viability study of PV power plants. *Renewable Energy*, 53, 193–199. <https://doi.org/10.1016/j.renene.2012.11.012>
- Besarati, S. M., Yogi Goswami, D., & Stefanakos, E. K. (2014). Optimal heliostat aiming strategy for uniform distribution of heat flux on the receiver of a solar

- power tower plant. *Energy Conversion and Management*, 84, 234–243.
<https://doi.org/10.1016/j.enconman.2014.04.030>
- Boretti, A. (2018). Concentrated Solar Power Plants Capacity Factors: A Review. In *Nonlinear Approaches in Engineering Applications* (pp. 41–62).
https://doi.org/10.1007/978-3-319-69480-1_2
- Bosatra, M., Fazi, F., Lionetto, P. F., & Travagnin, L. (2010). Utility Scale PV and CSP Solar Power Plants Performance, Impact on the Territory and Interaction with the Grid Performance , impact on the territory and interaction with the grid. *Power-Gen Europe 2010*.
- Bradshaw, R. W., Dawson, D. B., De la Rosa, W., GILBERT, R., Goods, S. H., HALE, M. J., ... Vant-Hull, L. L. (2002). Final Test and Evaluation Results from the Solar Two Project. In *Contract*. <https://doi.org/10.2172/793226>
- Chang, Z. S., Li, X., Xu, C., Chang, C., & Wang, Z. F. (2015). *The design and numerical study of a 2MWh molten salt thermocline tank*. 69, 779–789.
<https://doi.org/10.1016/j.egypro.2015.03.094>
- Chean, Y., Too, S., García, J., Vasquez, R., Kim, J., & Sanjuan, M. (2019). A transient optical-thermal model with dynamic matrix controller for solar central receivers. *Applied Thermal Engineering*, 154(November 2018), 686–698.
<https://doi.org/10.1016/j.applthermaleng.2019.03.086>
- Chu, Y., & Coimbra, C. F. M. (2017). Short-term probabilistic forecasts for Direct Normal Irradiance. *Renewable Energy*, 101, 526–536.
<https://doi.org/10.1016/j.renene.2016.09.012>
- Churchill, S. W., & Bernstein, M. (1977). A Correlating Equation for Forced Convection From Gases and Liquids to a Circular Cylinder in Crossflow. *Journal of Heat Transfer*, 99(2), 300–306. <https://doi.org/10.1115/1.3450685>

- Coimbra, C. F. M., & Pedro, H. T. C. (2013). Stochastic-Learning Methods. *Solar Energy Forecasting and Resource Assessment*, 383–406.
<https://doi.org/10.1016/B978-0-12-397177-7.00015-2>
- Coley, P. F., & Jonas, P. R. (1999). Back to basics: Clouds and the earth's radiation budget. *Weather*, 54(3), 66–70. <https://doi.org/10.1002/j.1477-8696.1999.tb06428.x>
- Collado, F. J., & Guallar, J. (2019). A two-parameter aiming strategy to reduce and flatten the flux map in solar power tower plants. *Solar Energy*, 188, 185–189.
<https://doi.org/10.1016/j.solener.2019.06.001>
- De Oliveira, M. M., Couto, A. A., Almeida, G. F. C., Reis, D. A. P., De Lima, N. B., & Baldan, R. (2019). Mechanical behavior of inconel 625 at elevated temperatures. *Metals*, 9(3). <https://doi.org/10.3390/met9030301>
- DOE. (2010). *Concentrating solar power commercial application study: Reducing water consumption of concentrating solar power electricity generation*. Retrieved from https://www1.eere.energy.gov/solar/pdfs/csp_water_study.pdf
- DOE, U. S. (2017). *The SunShot 2030 Goals: 3¢ per Kilowatt Hour for PV and 5 ¢ per Killowatt Hour for Dispatchable CSP*. 2–6. <https://doi.org/10.3¢>
- Dowling, N. E. (1999). *Mechanical behavior of materials : engineering methods for deformation, fracture, and fatigue*. Retrieved from http://libnet.ac.il/~libnet/pqd/opac_tau.pl?000421915
- Eltahir, E. A. B., & Humphries, E. J. (1998). The role of clouds in the surface energy balance over the Amazon forest. *International Journal of Climatology*, 18(14), 1575–1591. [https://doi.org/10.1002/\(SICI\)1097-0088\(19981130\)18:14<1575::AID-JOC316>3.0.CO;2-U](https://doi.org/10.1002/(SICI)1097-0088(19981130)18:14<1575::AID-JOC316>3.0.CO;2-U)
- Flesch, R., Frantz, C., Maldonado Quinto, D., & Schwarzbözl, P. (2017). Towards an

- optimal aiming for molten salt power towers. *Solar Energy*, 155, 1273–1281.
<https://doi.org/10.1016/j.solener.2017.07.067>
- Fritz, S. (1957). Solar Energy on Clear and Cloudy Days. *The Scientific Monthly*, 84(2), 55–65.
- García-Martín, F. J., Berenguel, M., Valverde, A., & Camacho, E. F. (1999).
 Heuristic knowledge-based heliostat field control for the optimization of the
 temperature distribution in a volumetric receiver. *Solar Energy*, 66(5), 355–369.
[https://doi.org/https://doi.org/10.1016/S0038-092X\(99\)00024-9](https://doi.org/https://doi.org/10.1016/S0038-092X(99)00024-9)
- García, J. M., Padilla, R. V., & Sanjuan, M. E. (2016). A biomimetic approach for
 modeling cloud shading with dynamic behavior. *Renewable Energy*, 96, 157–
 166. <https://doi.org/10.1016/j.renene.2016.04.070>
- García, J, Too, Y. C. S., Padilla, R. V, Vicencio, R. B., Beath, A., & Sanjuan, M.
 (2017). Heat flux distribution over a solar central receiver using an aiming
 strategy based on a conventional closed control loop. *ASME 2017 11th
 International Conference on Energy Sustainability, ES 2017, Collocated with
 the ASME 2017 Power Conference Joint with ICOPE 2017, the ASME 2017
 15th International Conference on Fuel Cell Science, Engineering and
 Technology, and the ASME 201*, (July). <https://doi.org/10.1115/ES2017-3615>
- García, Jesús, Barraza, R., Soo Too, Y. C., Vásquez Padilla, R., Acosta, D., Estay, D.,
 & Valdivia, P. (2020). Aiming clusters of heliostats over solar receivers for
 distributing heat flux using one variable per group. *Renewable Energy*, 160,
 584–596. <https://doi.org/10.1016/j.renene.2020.06.096>
- García, Jesús, Chean Soo Too, Y., Vasquez Padilla, R., Beath, A., Kim, J.-S., &
 Sanjuan, M. E. (2018). Multivariable Closed Control Loop Methodology for
 Heliostat Aiming Manipulation in Solar Central Receiver Systems. *Journal of
 Solar Energy Engineering*, 140(3), 31010. <https://doi.org/10.1115/1.4039255>

- García, Jesús, Chean, Y., Too, S., Vasquez, R., Beath, A., Kim, J., & Sanjuan, M. E. (2018). Dynamic performance of an aiming control methodology for solar central receivers due to cloud disturbances. *Renewable Energy*, 121, 355–367. <https://doi.org/10.1016/j.renene.2018.01.019>
- García, Jesús, Portnoy, I., Vasquez Padilla, R., & Sanjuan, M. E. (2018). Dynamic Modeling of Solar Radiation Disturbances Based on a Biomimetic Cloud Shading Model. *Journal of Solar Energy Engineering*, 140(2), 21008. <https://doi.org/10.1115/1.4038961>
- Gastón, M., Santigosa, L., Zarzalejo, L. F., Maria Vindel, J., Hanrieder, N., Wilbert, S., ... Wilbert, S. (2017). Optimizing DNI forecast using combinations of nowcasting models from the DNICast project. In *European Conference for Applied Meteorology and Climatology*. Retrieved from <http://elib.dlr.de/115535/>
- Goswami, D. Y. (2015). Principles of Solar Engineering. In *Principles of Solar Engineering*. <https://doi.org/10.1201/b18119>
- Grobler, A. (2015). *AIMING STRATEGIES FOR SMALL CENTRAL RECEIVER SYSTEMS*. Retrieved from <http://hdl.handle.net/10019.1/97051>
- Han, F., & Dai, W. (2013). New higher-order compact finite difference schemes for 1D heat conduction equations. *Applied Mathematical Modelling*, 37(16–17), 7940–7952. <https://doi.org/10.1016/j.apm.2013.03.026>
- Hernandez, J. A., Arredondo, C. A., & Rodriguez, Di. J. (2019). Analysis of the law for the integration of non-conventional renewable energy sources (law 1715 of 2014) and its complementary decrees in Colombia. *Conference Record of the IEEE Photovoltaic Specialists Conference*, 1695–1700. <https://doi.org/10.1109/PVSC40753.2019.8981233>
- Hetnarski, R. B., & Eslami, M. R. (2009a). Thermal stresses - Advanced theory and

- applications. *Solid Mechanics and Its Applications*, 158, 1–591.
https://doi.org/10.1007/978-1-4020-9247-3_1
- Hetnarski, R. B., & Eslami, M. R. (2009b). Thermal Stresses – Advanced Theory and Applications. In *Solid Mechanics and its Applications*.
<https://doi.org/10.1007/978-1-4020-9247-3>
- Hoffschmidt, B., Alexopoulos, S., Rau, C., Sattler, J., Anthrakidis, A., Boura, C., ... Hilger, P. (2012). Concentrating solar power. In *Comprehensive Renewable Energy* (Vol. 3). <https://doi.org/10.1016/B978-0-08-087872-0.00319-X>
- IEA. (2020). *Concentrating Solar Power (CSP)*. Retrieved from <https://www.iea.org/reports/concentrating-solar-power-csp>
- IRENA. (2018a). International Renewable Energy Agency. Renewable Power Generation Costs in 2017. In *International Renewable Energy Agency*. Retrieved from <https://www.irena.org/publications/2018/Jan/Renewable-power-generation-costs-in-2017>
- IRENA. (2018b). Renewable Power Generation Costs in 2017. In I. R. E. A. (IRENA) (Ed.), *International Renewable Energy Agency*. Retrieved from <https://www.irena.org/publications/2018/Jan/Renewable-power-generation-costs-in-2017>
- ISO. (1990). ISO 9060 - Specification and Classification of Instruments for Measuring Hemispherical Solar and Direct Solar Radiation. *Solar Energy Engineering*.
- Karellas, S., & Roumpedakis, T. C. (2019). Solar thermal power plants. In *Solar Hydrogen Production: Processes, Systems and Technologies*.
<https://doi.org/10.1016/B978-0-12-814853-2.00007-2>
- Kashaev, N., Horstmann, M., Ventzke, V., Riekehr, S., & Huber, N. (2013).

- Comparative study of mechanical properties using standard and micro-specimens of base materials Inconel 625, Inconel 718 and Ti-6Al-4 v. *Journal of Materials Research and Technology*, 2(1), 43–47.
<https://doi.org/10.1016/j.jmrt.2013.03.003>
- Kazantzidis, A., Tzoumanikas, P., Blanc, P., Massip, P., Wilbert, S., & Ramirez-Santigosa, L. (2017). Short-term forecasting based on all-sky cameras. In *Renewable Energy Forecasting: From Models to Applications* (pp. 153–178).
<https://doi.org/10.1016/B978-0-08-100504-0.00005-6>
- Kim, J. S., Potter, D., Gardner, W., Too, Y. C. S., & Padilla, R. V. (2017). Ideal heat transfer conditions for tubular solar receivers with different design constraints. *AIP Conference Proceedings*, 1850(June). <https://doi.org/10.1063/1.4984373>
- Kistler, B. L. (1987). *Fatigue analysis of a solar central receiver design using measured weather data*. (April), 1–64. Retrieved from
<http://prod.sandia.gov/techlib/access-control.cgi/1986/868017.pdf>
- Kleissl, J. (2013). *Solar Energy Forecasting and Resource Assessment*.
<https://doi.org/10.1016/C2011-0-07022-9>
- Kolb, G. J. (2011). An evaluation of possible next-generation high temperature molten-salt power towers. *Sandia National Laboratories, SAND2011-9*(December).
- Kraemer, S. (2020). In South Africa and Spain, CSP is Meeting or Exceeding Projected Operation Targets. Retrieved February 27, 2021, from
<https://www.solarpaces.org/in-south-africa-and-spain-csp-is-meeting-or-exceeding-projected-operation-targets/>
- Kuhn, P., Wirtz, M., Killius, N., Wilbert, S., Bosch, J. L., Hanrieder, N., ... Pitz-Paal, R. (2018). Benchmarking three low-cost, low-maintenance cloud height

- measurement systems and ECMWF cloud heights against a ceilometer. *Solar Energy*, 168(March), 140–152. <https://doi.org/10.1016/j.solener.2018.02.050>
- Kuhn, P, Wilbert, S., Prahl, C., Schöler, D., Haase, T., Hirsch, T., ... Pitz-Paal, R. (2017). Shadow camera system for the generation of solar irradiance maps. *Solar Energy*, 157, 157–170. <https://doi.org/10.1016/j.solener.2017.05.074>
- Kuhn, Pascal, Nouri, B., Wilbert, S., Prahl, C., Kozonek, N., Schmidt, T., ... Pitz-Paal, R. (2017). Validation of an all-sky imager-based nowcasting system for industrial PV plants. *Progress in Photovoltaics: Research and Applications*, (October), 1–14. <https://doi.org/10.1002/pip.2968>
- Lele, S. K. (1992). Compact finite difference schemes with spectral-like resolution. *Journal of Computational Physics*, 103(1), 16–42. [https://doi.org/10.1016/0021-9991\(92\)90324-R](https://doi.org/10.1016/0021-9991(92)90324-R)
- Li, Z. (1995). The variable effect of clouds on atmospheric absorption of solar radiation. *Nature*, 376.
- Lilliestam, J. (2018). *Whither CSP? Taking stock of a decade of concentrating solar power expansion and development. Deliverable 4.2, MUSTEC project, ETH Zürich, Zurich.* (764626). Retrieved from [https://mustec.eu/sites/default/files/reports/Lilliestam 2018 Whither CSP_Deliverable4.2 MUSTEC.pdf](https://mustec.eu/sites/default/files/reports/Lilliestam%202018%20Whither%20CSP_Deliverable4.2%20MUSTEC.pdf)
- Lilliestam, J., & Pitz-Paal, R. (2018). Concentrating solar power for less than USD 0.07 per kWh: finally the breakthrough? *Renewable Energy Focus*, 26(00), 17–21. <https://doi.org/10.1016/j.ref.2018.06.002>
- Liu, D., Zhang, X., Qin, X., & Ding, Y. (2017). High-temperature mechanical properties of Inconel-625: role of carbides and delta phase. *Materials Science and Technology (United Kingdom)*, 33(14), 1610–1617.

<https://doi.org/10.1080/02670836.2017.1300365>

- Liu, Y., Wu, W., Jensen, M. P., & Toto, T. (2011). Relationship between cloud radiative forcing, cloud fraction and cloud albedo, and new surface-based approach for determining cloud albedo. *Atmospheric Chemistry and Physics*, 11(14), 7155–7170. <https://doi.org/10.5194/acp-11-7155-2011>
- Ljung, L. (1987). Ljung L System Identification Theory for User. In *PTR Prentice Hall Upper Saddle River NJ*.
- Lovegrove, K., & Pye, J. (2012). 2 – Fundamental principles of concentrating solar power (CSP) systems. In *Concentrating Solar Power Technology* (pp. 16–67). <https://doi.org/10.1533/9780857096173.1.16>
- Lovegrove, Keith, & Stein, W. (Eds.). (2012). Copyright. In *Concentrating Solar Power Technology* (p. iv). <https://doi.org/https://doi.org/10.1016/B978-1-84569-769-3.50022-4>
- Maldonado, D., Flesch, R., Reinholz, A., & Schwarzbözl, P. (2018). Evaluation of aim point optimization methods. *AIP Conference Proceedings*, 2033(November). <https://doi.org/10.1063/1.5067061>
- Margolis, R., Feldman, D., & Boff, D. (2018). *Solar Industry Update*. (May), 1–83. <https://doi.org/NREL/PR-6A20-68425>
- Marlin, T. (1995). *Process Control: Designing Processes and Control Systems for Dynamic Performance*. New York: McGraw-Hill.
- Marugán-Cruz, C., Flores, O., Santana, D., & García-Villalba, M. (2016). Heat transfer and thermal stresses in a circular tube with a non-uniform heat flux. *International Journal of Heat and Mass Transfer*, 96, 256–266. <https://doi.org/10.1016/j.ijheatmasstransfer.2016.01.035>

- Mehos, M., Turchi, C., Vidal, J., Wagner, M., Ma, Z., Ho, C., ... NREL. (2017). Concentrating Solar Power Gen3 Demonstration Roadmap. *Nrel/Tp-5500-67464*, (January), 1–140. <https://doi.org/10.2172/1338899>
- Merchán, R. P., Santos, M. J., García-Ferrero, J., Medina, A., & Hernández, A. C. (2021). Thermo-economic and sensitivity analysis of a central tower hybrid Brayton solar power plant. *Applied Thermal Engineering*, 186(April 2020). <https://doi.org/10.1016/j.applthermaleng.2020.116454>
- Michael , Krüger; Selman, Muslubas ; Thomas , Loeper , Freerk Klasing , Philipp Knödler, C. M., Krüger, M., Muslubas, S., Loeper, T., Klasing, F., Knödler, P., & Mielke, C. (2020). Potentials of Thermal Energy Storage Integrated into Steam Power Plants. *Energies*, 13(9), 1–13. <https://doi.org/10.3390/en13092226>
- Miller, S. D., Heidinger, A. K., & Sengupta, M. (2013). Physically Based Satellite Methods. In *Solar Energy Forecasting and Resource Assessment*. <https://doi.org/10.1016/B978-0-12-397177-7.00003-6>
- Moin, P. (2010). Fundamentals of engineering numerical analysis. In *Fundamentals of Engineering Numerical Analysis* (Vol. 9780521884327). <https://doi.org/10.1017/CBO9780511781438>
- Montoya, A., Rodríguez-Sánchez, M. R., López-Puente, J., & Santana, D. (2018). Numerical model of solar external receiver tubes: Influence of mechanical boundary conditions and temperature variation in thermoelastic stresses. *Solar Energy*, 174, 912–922. <https://doi.org/10.1016/j.solener.2018.09.068>
- Musi, R., Grange, B., Sgouridis, S., Guedez, R., Armstrong, P., Slocum, A., & Calvet, N. (2017). Techno-economic analysis of concentrated solar power plants in terms of levelized cost of electricity. *AIP Conference Proceedings*, 1850. <https://doi.org/10.1063/1.4984552>

- Neises, T. W., Wagner, M. J., & Gray, A. K. (2014a). *ES2014-6603 Structural Design Considerations for Tubular Power Tower*. (April), 1–7.
- Neises, T. W., Wagner, M. J., & Gray, A. K. (2014b). Structural design considerations for tubular power tower receivers operating at 650°C. *ASME 2014 8th International Conference on Energy Sustainability, ES 2014 Collocated with the ASME 2014 12th International Conference on Fuel Cell Science, Engineering and Technology, 1*(April). <https://doi.org/10.1115/ES2014-6603>
- Noureldin, K., Hirsch, T., Kuhn, P., Nouri, B., Yasser, Z., & Pitz-Paal, R. (2018). Modelling an automatic controller for parabolic trough solar fields under realistic weather conditions. *AIP Conference Proceedings, 2033*(November). <https://doi.org/10.1063/1.5067211>
- Nouri, B., Kuhn, P., Wilbert, S., Hanrieder, N., Prah, C., Zarzalejo, L., ... Pitz-Paal, R. (2019). Cloud height and tracking accuracy of three all sky imager systems for individual clouds. *Solar Energy, 177*(August 2018), 213–228. <https://doi.org/10.1016/j.solener.2018.10.079>
- Nouri, B., Noureldin, K., Schlichting, T., Wilbert, S., Hirsch, T., Schroedter-Homscheidt, M., ... Pitz-Paal, R. (2020). Optimization of parabolic trough power plant operations in variable irradiance conditions using all sky imagers. *Solar Energy, 198*, 434–453. <https://doi.org/10.1016/j.solener.2020.01.045>
- Nouri, Bijan, Wilbert, S., Hanrieder, N., Kuhn, P., Schroedter-Homscheidt, M., Pitz-Paal, R., ... Affolter, R. (2018). Intra-hour classification of direct normal irradiance for two sites in Spain and India. In *SolarPaces 2018* (Vol. 1).
- Nouri, Bijan, Wilbert, S., Kuhn, P., Hanrieder, N., Schroedter-Homscheidt, M., Kazantzidis, A., ... Pitz-Paal, R. (2019). Real-time uncertainty specification of all sky imager derived irradiance nowcasts. *Remote Sensing, 11*(9).

<https://doi.org/10.3390/rs11091059>

- Pacheco, J. E., Bradshaw, R. W., Dawson, D. B., la Rosa, W., Gilbert, R., Goods, S. H., ... others. (2002). Final test and evaluation results from the Solar Two project. *Report No. SAND2002-0120, Sandia National Laboratories, Albuquerque, NM.*
- Padilla, R. V., Demirkaya, G., Goswami, D. Y., Stefanakos, E., & Rahman, M. M. (2011). Heat transfer analysis of parabolic trough solar receiver. *Applied Energy*, 88(12), 5097–5110. <https://doi.org/10.1016/j.apenergy.2011.07.012>
- Pereira, F. G. L., Lourenço, J. M., Nascimento, R. M. do, & Castro, N. A. (2018). Fracture Behavior and Fatigue Performance of Inconel 625. *Materials Research*, 21(4). <https://doi.org/10.1590/1980-5373-mr-2017-1089>
- Pfahl, A., Coventry, J., Röger, M., Wolfertstetter, F., Vásquez-Arango, J. F., Gross, F., ... Liedke, P. (2017). Progress in heliostat development. *Solar Energy*, 152, 3–37. <https://doi.org/10.1016/j.solener.2017.03.029>
- REEEI. (2012). *Pre-feasibility study for the establishment of a pre-commercial concentrated solar power plant in namibia*. (September). Retrieved from <http://nei.nust.na/sites/default/files/projects/NA.2012.R.005.2.pdf>
- Relloso, S., & García, E. (2015). Tower Technology Cost Reduction Approach after Gemasolar Experience. *Energy Procedia*, 69, 1660–1666. <https://doi.org/10.1016/j.egypro.2015.03.125>
- Roeb, M., Säck, J. P., Rietbrock, P., Prahl, C., Schreiber, H., Neises, M., ... Konstandopoulos, A. G. (2011). Test operation of a 100kW pilot plant for solar hydrogen production from water on a solar tower. *Solar Energy*, 85(4), 634–644. <https://doi.org/10.1016/j.solener.2010.04.014>
- Röger, M. (2017). *Protocol for Optical and Geometrical Evaluation of Heliostats*.

- Röger, M., Herrmann, P., Ulmer, S., Ebert, M., Prah, C., & Göhring, F. (2014). Techniques to Measure Solar Flux Density Distribution on Large-Scale Receivers. *Journal of Solar Energy Engineering*, 136(3), 031013. <https://doi.org/10.1115/1.4027261>
- Rojas-Morín, A., & Fernández-Reche, J. (2011). Estimate of thermal fatigue lifetime for the INCONEL 625ICF plate while exposed to concentrated solar radiation. *Revista de Metalurgia (Madrid)*, 47(2), 112–125. <https://doi.org/10.3989/revmetalmadrid.1038>
- Sánchez-González, A., Caliot, C., Ferrière, A., & Santana, D. (2017). Determination of heliostat canting errors via deterministic optimization. *Solar Energy*, 150, 136–146. <https://doi.org/10.1016/j.solener.2017.04.039>
- Sánchez-González, A., Rodríguez-Sánchez, M. R., & Santana, D. (2017). Aiming strategy model based on allowable flux densities for molten salt central receivers. *Solar Energy*, 157, 1130–1144. <https://doi.org/10.1016/j.solener.2015.12.055>
- Sánchez-González, A., Rodríguez-Sánchez, M. R., & Santana, D. (2020a). Allowable solar flux densities for molten-salt receivers: Input to the aiming strategy. *Results in Engineering*, 5(November 2019). <https://doi.org/10.1016/j.rineng.2019.100074>
- Sánchez-González, A., Rodríguez-Sánchez, M. R., & Santana, D. (2020b). Allowable solar flux densities for molten-salt receivers: Input to the aiming strategy. *Results in Engineering*, 5(September 2019). <https://doi.org/10.1016/j.rineng.2019.100074>
- Sattler, J., Hoffschmidt, B., Joemann, M., Ajib, S., Anthrakidis, A., Boura, C. T., & Faber, C. (2011). Advanced CSP Teaching Materials Chapter 9 Thermal Energy Storage. *Advanced CSP Teaching Materials*, 38–40.

- Schallenberg, K. (2013). *Initial Performance History - O&M Lessons Learned*. Retrieved from <https://slideplayer.com/slide/4290994/>
- Schlecht, M., & Meyer, R. (2012). 4 – Site selection and feasibility analysis for concentrating solar power (CSP) systems. In *Concentrating Solar Power Technology* (pp. 91–119). <https://doi.org/10.1533/9780857096173.1.91>
- Schwarzbözl, P., Pitz-Paal, R., & Schmitz, M. (2009). Visual HFLCAL - A Software Tool for Layout and Optimisation of Heliostat Fields. *Proceedings*.
- Sengupta, M., Habte, A., Kurtz, S., Dobos, A., Wilbert, S., Lorenz, E., ... Perez, R. (2015). *Best Practices Handbook for the Collection and Use of Solar Resource Data for Solar Energy Applications*. (NREL/TP-5D00-63112), 251 pages. Retrieved from <http://www.nrel.gov/docs/fy15osti/63112.pdf>
- Siebers, D. L., & Kraabel, J. S. (1984). *Estimating convective energy losses from solar central receivers*. <https://doi.org/10.2172/6906848>
- Smith, C. A., & Corripio, A. B. (2006). *Principles and Practice of Automatic Process Control*, John Willey & Sons. Inc.
- Smith, D. C., & Chavez, J. M. (1988). *Final Report on the Phase I Testing of a Molten-Salt Volume I-A Summary Report*. Retrieved from <https://www.osti.gov/servlets/purl/6461363>
- Soo Too, Y. C., García, J., Padilla, R. V., Kim, J. S., & Sanjuan, M. (2019). A transient optical-thermal model with dynamic matrix controller for solar central receivers. *Applied Thermal Engineering*, 686–698. <https://doi.org/10.1016/j.applthermaleng.2019.03.086>
- Stefan Zunft , Matthias Hänel , Michael Krüger , Volker Dreißigacker , Felix Göhring, E. W., Zunft, S., Hänel, M., Krüger, M., Dreißigacker, V., Göhring, F., & Wahl, E. (2011). Jülich Solar Power Tower—Experimental Evaluation of the

- Storage Subsystem and Performance Calculation. *Journal of Solar Energy Engineering*, 133(3), 1–5. <https://doi.org/10.1115/1.4004358>
- Stewart, R. H. (2009). *Introduction to Physical Oceanography*. Retrieved from <https://books.google.de/books?id=3dXTRAAACAAJ>
- Stoffel, T. (2013). Terms and Definitions. In *Solar Energy Forecasting and Resource Assessment*. <https://doi.org/10.1016/B978-0-12-397177-7.00001-2>
- Takeut, Y., & Nod, N. (1980). Three-dimensional transient thermal stresses in a finite circular cylinder under nonaxisymmetric temperature distribution. *Journal of Thermal Stresses*, 3(2), 159–183. <https://doi.org/10.1080/01495738008926961>
- Urquhart, B., Ghonima, M., Nguyen, D. (Andu), Kurtz, B., Chow, C. W., & Kleissl, J. (2013). Sky-Imaging Systems for Short-Term Forecasting. In *Solar Energy Forecasting and Resource Assessment*. <https://doi.org/10.1016/B978-0-12-397177-7.00009-7>
- US Energy Information Agency, E. (2019). International Energy Outlook 2019 with projections to 2050. In *Choice Reviews Online*. <https://doi.org/10.5860/CHOICE.44-3624>
- Vant-hull, L. L. (2002). The role of “allowable flux density” in the design and operation of molten-salt solar central receivers. *Journal of Solar Energy Engineering, Transactions of the ASME*, 124(2), 165–169. <https://doi.org/10.1115/1.1464124>
- Vant-Hull, L. L. L. (2012). Central tower concentrating solar power (CSP) systems. In *Concentrating Solar Power Technology: Principles, Developments and Applications* (pp. 240–283). <https://doi.org/10.1016/B978-1-84569-769-3.50008-X>
- Veda, S., Zhang, Y., Tan, J., Chartan, E., Duckworth, J., Gilroy, N., ... Ericson, S.

- (2018). *Evaluating the Impact of the 2017 Solar Eclipse*. Retrieved from <https://www.nrel.gov/news/press/2018/nrel-researchers-measure-impact-of-eclipse-on-electrical-grid.html>
- Vignola, F. E., McMahan, A. C., & Grover, C. N. (2013). Bankable Solar-Radiation Datasets. In *Solar Energy Forecasting and Resource Assessment*. <https://doi.org/10.1016/B978-0-12-397117-7.00005-X>
- Von Storch, H., Becker-Hardt, S., & Sattler, C. (2018). (Solar) mixed reforming of methane: Potential and limits in utilizing CO₂ as feedstock for syngas production - A thermodynamic analysis. *Energies*, *11*(10), 1–14. <https://doi.org/10.3390/en11102537>
- Wang, G., Kurtz, B., & Kleissl, J. (2016). Cloud base height from sky imager and cloud speed sensor. *Solar Energy*, *131*, 208–221. <https://doi.org/10.1016/j.solener.2016.02.027>
- Winter, C. J., Sizmann, R. L., & Vant-Hull, L. L. (Eds.). (1991). *Solar power plants: fundamentals, technology, systems, economics*. Berlin ; New York: Springer-Verlag.
- XM. (2019). Resultados generales subasta OEF 2022-2023. In *Compañía Expertos en Mercados S.A. E.S.P.* Retrieved from [https://www.xm.com.co/Resultado subasta cargo por confiabilidad/ResultadosSubasta OEF22-23.pdf](https://www.xm.com.co/Resultado%20subasta%20carga%20por%20confiabilidad/ResultadosSubasta%20OEF22-23.pdf)
- XM. (2021). Resultados subasta CLPE 03-2021. In *Compañía Expertos en Mercados S.A. E.S.P.* Retrieved from [https://www.xm.com.co/SubastaCLPE2021/Informe Resultados Nueva Subasta 2021.pdf](https://www.xm.com.co/SubastaCLPE2021/Informe%20Resultados%20Nueva%20Subasta%202021.pdf)
- Zavoico, A. B. (2001). Solar Power Tower - Design Basis Document. *Technical Report SAND2001-2100*, (July), 148. <https://doi.org/10.2172/786629>

APPENDIX A: Publications derived from this research

A.1. Solar Energy



Solar Energy
Volume 215, February 2021, Pages 12-25



Flux-feedback as a fast alternative to control groups of aiming points in molten salt power towers

David Acosta ^a , Jesus Garcia ^b, Marco Sanjuan ^a, Laurin Oberkirsch ^c, Peter Schwarzbözl ^c

^a Department of Mechanical Engineering, Universidad del Norte, Barranquilla, Colombia

^b Department of Mechanical Engineering, Universidad Técnica Federico Santa María, Valparaíso, Chile

^c DLR, German Aerospace Center, Institute of Solar Research, Linder Höhe, 51147 Cologne, Germany

Received 14 June 2020, Revised 12 October 2020, Accepted 13 December 2020, Available online 5 January 2021.

A.2. Renewable Energy



Renewable Energy
Volume 160, November 2020, Pages 584-596



Aiming clusters of heliostats over solar receivers for distributing heat flux using one variable per group

Jesús García ^a , Rodrigo Barraza ^a , Yen Chean Soo Too ^b , Ricardo Vásquez Padilla ^c , David Acosta ^d , Danilo Estay ^a , Patricio Valdivia ^a

Show more

+ Add to Mendeley Share Cite

<https://doi.org/10.1016/j.renene.2020.06.096>

Get rights and content

A.3. Solar Paces 2020

Effect of Solar Field Aiming Strategies on the Fatigue Life in Molten Salt External Central Receivers

Richard Rangel^{1, b)}, David Acosta^{1, a)}, Jesús García², Marco Sanjuan¹, Rodrigo Barraza² and Habib Zambrano¹

¹Universidad del Norte, Mechanical Engineering Department, Km 5 vía Puerto Colombia, Metropolitan area of Barranquilla, Colombia.

²Universidad Técnica Federico Santa María, Mechanical Engineering Department, Vicuña Mackenna 3939, Santiago, Chile.

^{a)}Corresponding author: villamilr@uninorte.edu.co

^{b)}rerangel@uninorte.edu.co

A.4. Revista de Ingeniería de la Universidad de Antioquía

Control scheme selection and optimal tuning in industrial process control using factorial experiment design

David Roberto Acosta Villamil

Universidad del Norte

 <https://orcid.org/0000-0001-7978-516X>

José Fernando Noguera Polanía

Universidad del Norte

 <https://orcid.org/0000-0001-4780-3762>

Arnaldo Verdeza Villalobos

Universidad Simón Bolívar; Universidad del Norte

 <https://orcid.org/0000-0002-5147-2477>

Blanca Luz Foliaco Romero

Universidad del Norte

 <https://orcid.org/0000-0001-6063-4910>

Adriana Fernanda Rincón Montenegro

Universidad del Norte

 <https://orcid.org/0000-0002-1324-9740>

Marco Enrique Sanjuan Mejía

Universidad del Norte

 <http://orcid.org/0000-0001-7435-0781>

DOI: <https://doi.org/10.17533/idea.redin.20201010>



APPENDIX B: Other publications during the doctoral program

B.1. Revista Ingeniare: Aceptado para publicación

Modelo de Red Neuronal ARMAX para un péndulo de Furuta *Neural Network ARMAX model for a Furuta pendulum*

David Acosta Villamil^{1*}
Jose Noguera Polania²
Jovanny Pacheco Bolivar³
Marco Sanjuan Mejia⁴

¹Universidad del Norte. Departamento de Ingeniería Mecánica. Barranquilla, Colombia. E-mail: villamilr@uninorte.edu.co

²Universidad del Norte. Departamento de Ingeniería Mecánica. Barranquilla, Colombia. E-mail: jfnoguera@uninorte.edu.co

³Universidad del Norte. Departamento de Ingeniería Mecánica. Barranquilla, Colombia. E-mail: jpacheco@uninorte.edu.co

⁴Universidad del Norte. Departamento de Ingeniería Mecánica. Barranquilla, Colombia. E-mail: msanjuan@uninorte.edu.co

* Autor de correspondencia: villamilr@uninorte.edu.co